Structural Systems Biology:

multiscale insights into the effect of drug-receptor interactions in neurosignaling pathways

by

Rui Pedro Fernandes Ribeiro

A thesis submitted for the degree of
Doctor of Philosophy

University of Verona
2021

UNIVERSITÀ DEGLI STUDI DI VERONA

DOTTORATO DI RICERCA IN BIOTECNOLOGIE

with funding by

University of Verona

XXXIII CYCLE

Coordinator: **Prof. Dr. Matteo Ballottari**
Advisor: **Prof. Dr. Alejandro Giorgetti**

Ph.D. Candidate: **Rui Pedro Fernandes Ribeiro**

Verona 2021

What is meant to be
will always find its way;
Always!

Acknowledgments

One of the great benefits of a PhD is the possibility of recognizing the frontiers of knowledge and trying to overcome them. When one has a scientific spirit, knowledge has no limits! However, this path can’t be made alone. As they say, here, in Italy: *“Da soli si va più veloce, ma insieme si va più lontano!”*

First and foremost, I would like to express my sincere gratitude to my advisor Prof. Alejandro Giorgetti for the continuous support of my PhD studies and related research, and also for believing in me since the first day. Thank you for your patience, motivation, immense knowledge, friendship, trust, and, especially, for giving me the freedom to think, be creative, and conduct my research on my own way and pace. Thank you for helping me to grow as a researcher, a person and a man.

To the University of Verona and the PhD School in Natural Sciences and Engineering, I am deeply grateful for the opportunity to do my studies on this illustrious institution and for funding them.

To my family, in particular to my parents, I want to thank them for supporting me spiritually every day, and for accepting my path despite the distance. Distance not always means absence, and it’s my belief that every path it’s the right path, and that everything that is happening now happens for my ultimate good.

To my friends, those that I left in Portugal and those that I met in Italy, thank you to brimming me with energy and overflowing me with joy, love and positivity. I thank you all for always encouraging me to follow my heart, intuition, and dreams.

Finally, to Italy, especially to the City of Verona and its people, thank you for welcoming me; thank you for making me feel one of yours. I finally found, here, the place where I belong to; the place to which I can call ***home!***

Abstract

During the process of drug discovery and development the pharmacodynamic models have been serving as the driving force for evaluating drugs at target sites and controlling drug-receptor interactions. Under the umbrella of systems biology and pharmacology, these quantitative models have been rapidly evolving from empirical descriptions to complex mathematical models of biochemical systems. The central idea is the delineation and quantification of drug-receptor interactions, internalization, signaling, and cellular effects enabling the rationalization of drug's modes of actions. Therefore, with the advent of *in silico* approaches in their many renditions, quantitative systems pharmacology attempts to advance our understanding on the relationships between the molecular level of drug-target interactions and higher-level cellular and physiologic mechanisms, pushing the new era of personalized and precision medicine closer.

In this thesis, it was intended to correlate the intracellular effects of the activation of neural-signaling cascades on ligand binding to neuroreceptors applying a combined structure-quantitative systems pharmacology approach. For this purpose, we started by implementing signaling pathways of the Oxytocin and the NMDA receptors to illustrate how merging structural macromolecular data with network biology allows us to explore the subcellular effects upon receptor activation and understand complex biological phenomena. The lack of a common interrelationship between structural biology and systems pharmacology, prompted us to propose a computational framework that integrates structure and quantitative systems pharmacology approaches. Here, it is also proposed a biocomputing framework designed for in-depth studies of post-synaptic neuroreceptors, in particular G-protein coupled receptors, in order to improve current empirically driven drug discovery approaches in a more precise drug design.

Sommario

Durante il processo di ricerca e sviluppo di farmaci, modelli farmacodinamici vengono utilizzati per descrivere l'accesso dei farmaci ai siti di legame dei rispettivi target molecolari, caratterizzando l'interazione farmaco-recettore. Sotto l'ombrello della *system biology* a della farmacologia, questi modelli quantitativi si sono rapidamente evoluti da semplici descrizioni empiriche a dettagliati modelli matematici di sistemi biochimici. L'idea centrale è quella di delineare e quantificare gli effetti cellulari generati dell'interazione farmaco-target, come ad esempio l'internalizzazione del recettore o l'attivazione di cascate di segnalazione, al fine di elucidare i meccanismi d'azione del farmaco a livello molecolare. Con l'avvento del potere descrittivo fornito dagli approcci *in silico*, nelle loro diverse declinazioni, la farmacologia sistemica quantitativa cerca quindi di approfondire la nostra comprensione delle relazioni che si creano tra i meccanismi molecolari attivati localmente dall'interazione farmaco-recettore e gli effetti fisiologici osservabili a livello cellulare e/o sistemico, avvicinandoci sempre più all'era della medicina personalizzata e consapevole.

Il lavoro presentato in questa tesi si focalizza sull'attività di cellule neuronali: l'obbiettivo è quello di correlare effetti molecolari intracellulari, generati dall'attivazione di vie di segnalazione, all'interazione tra recettori espressi in membrana ed i rispettivi ligandi, applicando un approccio ibrido di farmacologia sistemica quantitativa-strutturale. A tal fine, abbiamo cominciato implementando le vie di segnalazione molecolare associate ai recettori dell'Ossitocina ed ai recettori NMDA, per dimostrare come, unendo dati ottenibili dall'analisi strutturale di queste macromolecole a tecniche di biologia sistemica, sia possibile esplorare gli effetti intracellulari generati dell'attivazione dei recettori e comprendere così fenomeni biologici complessi. Avendo constatato a tutt'oggi l'assenza di una comunicazione consistente ed efficace tra

il mondo della biologia strutturale e quello della farmacologia sistemica, in questa tesi viene proposto un framework computazionale multi-scala atto a definire un approccio ibrido ed innovativo, capace di integrare informazioni strutturali dettagliate di singole macromolecole con descrizioni quantitative di ampie reti di interazioni tra molteplici macromolecole. Il framework bio-computazionale descritto nel seguente lavoro è stato progettato e sviluppato al fine di condurre analisi approfondite su recettori post-sinaptici, in particolare GPCR, con lo scopo di migliorare le tecniche di sviluppo di farmaci correntemente basate su approcci empirici fornendo gli strumenti conoscitivi per perseguire studi di sviluppo di farmaci razionale più consapevoli e precisi.

Table of Contents

PART I

Network and Systems Biology in structure-function studies of neuroreceptors

PART II

Pharmacology modeling and simulation workflows: integrating tools to create and investigate pharmacological models

CHAPTER 1

General Introduction

'So, in short, what we develop is a way, which requires a computer, to take the structure of a protein and then to eventually understand how exactly it does, what it does... you could use it, for example, to design drugs or just, like in my case, to satisfy your curiosity.'

Arieh Warshel*,*
Nobel Prize in Chemistry, 2013

The use of computers to apply biological theoretical ideas has shaped up our understanding on the dynamic of biological and biochemical events. In particular, the era of computers and computational methods has changed all aspects of drug research. The reality is that the use of computer has reduced the time, the cost, and the risk of failure of drug research by up 50%, allowing potent HITs to be obtained in a matter of weeks [1,2].

Although computational pharmacology has speeded up the drug discovery and development pipeline (*Fig. 1.1*), according to the *Pharmaceutical Research*

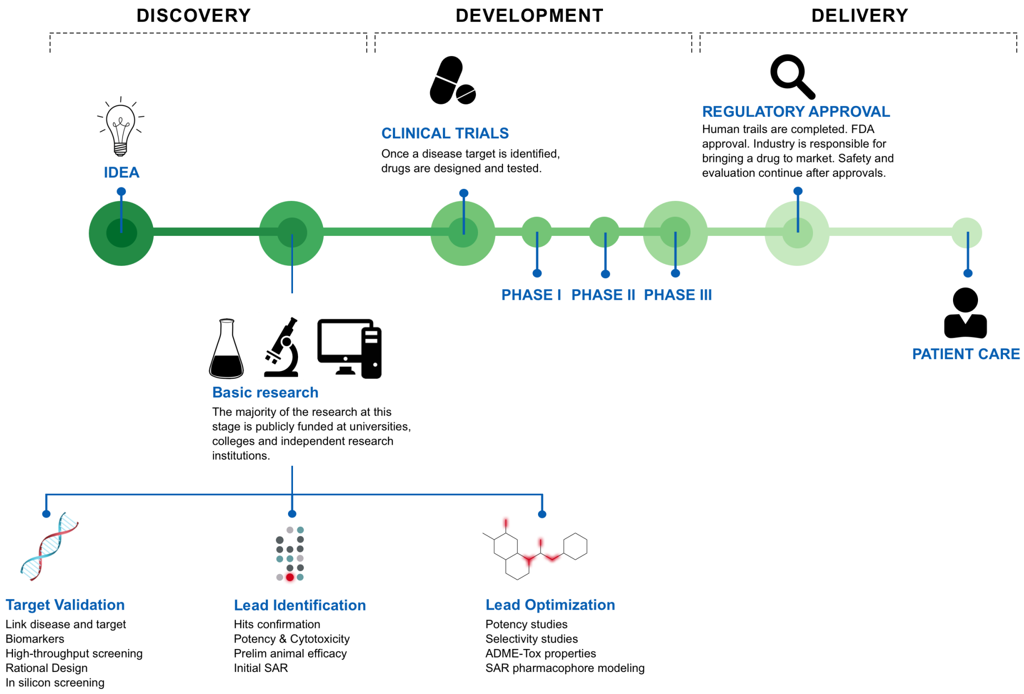

Fig. 1.1 This infographic provides a summary of the sequential steps that are necessary for a drug to progress through the research and development pipelines. Adapted from *researchamerica.com*.

and Manufacturers of America - PhRMA (phrma.org) - the research and development process of a new drug is still taking more than 10 years from the starting project to the final approval from the FDA (US Food and Drug Administration).

Despite all the available technology, the insights provided by the genomic research and the growing resources and founding, the number of new molecular entities, that is, a medication containing an active ingredient that has not been previously approved for marketing in any form, had been decreasing in the early 2000s; probably, due to several facts, such as clinical failures, increasing demands by regulatory authorities, and the disconnection between business and research goals [3–5]. More specifically, many promising drug candidates have been failing in the clinical phases, mainly due the poor understanding of the pathways involved in the mechanism of actions and the little attention paid to biochemical aspects like affinities and specificities of compounds [6,7].

However, in a recent outlook on how the pharmaceutical industry is looking upon their research and development strategies, reports that scientists are now working in fewer diseases areas with focus on a deeper scientific understanding of diseases' biology and mechanisms, and on the evolution of their approach to target validation, hit and lead optimization, pharmacokinetic/pharmacodynamic modeling and drug safety test. The pharma industry is now implementing a new decision-making framework that focuses on the right target, right tissue, right safety, right patient, and right commercial potential [8]. Thus, the process of drug discovery and development no longer focus only on single macromolecules, but on the understanding of the chemical and biological functions of organisms.

Under the umbrella of network and systems biology, protein targets have been now considered in a much broader systemic perspective of their physiologic environment, without losing the macromolecular details [7]. Since cells, tissues, organs, and all the biochemical entities underneath them, such as genes, proteins and metabolites exist in a form of complex nested networks, systems biology rose up as a new interdisciplinary field in which its main concern is to unveil the biochemical pathways and to catalogue all the biological complexes and the relationships between them [9].

Network and systems biology approaches have been already making important contributions to drug discovery and development and, despite being incomplete and error-prone, they are accurate enough to provide useful information [7]. As a matter of fact, such approaches have been assisting in the identification and evaluation of drug targets, for instance in tumor associated diseases [10,11].

Even if network and systems biology approaches changed the way biomedical research thinks about drug action in complex diseases, the truth is that these approaches only focus on the interactions between its elements. This means that the quantitative element that is missing should be, undoubtedly, included into systems biology. In other words, not only network and systems biology should study the physical and functional interactions between the elements that constitute the biological system, but also should measure the concentrations and kinetic parameters that govern these interactions [7]. Therefore, applying such concepts to pharmacology studies, the ***quantitative systems pharmacology*** rises up as a new discipline [9].

Based on mathematical models, quantitative systems pharmacology provides, then, a framework that bridges spatial and temporal dimensions allowing a better understanding on how drugs affect complex biological systems and pathophysiological processes [12]. Such mathematical models rely on the fundamental concept of the receptor occupancy theory initially proposed by A. J. Clark, thereby making the central idea of quantitative systems pharmacology as the quantification of ligand-receptor interaction and subsequent cellular effects. The receptor occupancy theory states that on drug binding a cellular effect mediated by the activation of a signaling cascade may result. And the intensity of the cellular effect depends on drug-receptor parameters like specificity, affinity (strength and time of binding), and availability (drug and receptor concentration) [12].

The cellular response mediated by those signaling pathways are, actually, an intricate series of molecular events, commonly proteins' phosphorylation catalyzed by kinases, and each one of these events can be described by a mathematical equation. Typically, a mathematical model of a biochemical network consists of a set of ***ordinary differential equations*** **(ODEs)**, and since ODEs depend only in one variable, they can be used to describe the change of the states of the system. For instance, if ODEs are integrated as a function of time, such reactions can describe how the concentration of species inside the network changes over time [13]. However, the biochemical reactions underneath a signaling cascade are, normally, governed by kinetic parameters. While drug-receptor binding or protein-protein interactions are characterized by a second-order association constant, k_{on}, and a first-order dissociation constant, k_{off} [12], the reactions of enzyme catalysis are characterized by K_m, V_{max} and K_{cat} [13]. Because under steady-state conditions these processes, from drug-receptor binding to downstream subcellular effects, occur at relatively short time scales equilibrium assumptions allow the explicit numerical calculation of concentration values of drugs, receptors, drug-receptor complexes and of all elements that make part of the signaling cascade [12].

Mathematical models of signal-transduction cascades have been developed for decades for a variety of systems such as the signaling mechanisms of hallucinogens towards the serotonin receptors [14], the sensing reward mechanism of dopaminergic receptors [15], the mechanism of phototransduction mediated by rhodopsin receptors [16–18], or the signaling mediated by the epidermal growth factor receptor [19]. In fact, the number of mathematical models of signaling cascades have been growing so fast that many databases to store them have also been developed. Today, many repository of pathways and mathematical models of biological and biomedical systems can be easily found across the internet, such as the *BioModels* database [20,21].

However, the dynamic modeling of biochemical networks is still hampered by the lack of kinetic parameters needed to feed the network. Ideally, such parameters should be determined experimentally under relevant conditions to the model; however, the truth is that the existing parameters are distributed in literature and relate to different experimental conditions [13,22].

This is where protein structural data plays its role. Since all the kinetic parameters are encoded in the three-dimensional macromolecular structure of proteins, such information can be used to estimate these parameters. In fact, at the same time as the number of mathematical models grow, the number of protein structures that are being solved also rises concurrently [23]. For these reasons, the role of high-resolution three-dimensional protein structures in systems biology/pharmacology has become unquestionable, making many researchers claiming and advocating a new paradigm of ***structure systems pharmacology*** [22,24]. The proof of this is the tremendous quantity of computationally methods, developed in the past years, to derive quantitative structure-kinetics relationships. For instance, molecular dynamics (MD) simulations in their many renditions have been used to estimate drug-receptor binding kinetics [25–27], specially, metadynamics [28]. Another approach is the comparison of molecular interaction fields by similarity indices. Assuming that the molecular interaction fields are the most relevant factors in determining the kinetic parameters values, such parameters can be transferable between related proteins [13]. More recently, thanks to the power of machine and deep learning, many approaches using convolution neural networks have been promising the prediction of binding affinity data from protein-ligand complex structures [29,30].

Taken as a whole, structural-quantitative systems pharmacology provides an unprecedented molecular framework for understanding complex cell processes and molecular networks related to diseases. Bringing to light the dynamic interplay between those complex biological systems and drugs, systems pharmacology has been proposed as an alternative to overcome the critical steps in the drug discovery pipeline [24], promising then to be next-generation of drug-discovery and personalized medicine.

References

1. Jorgensen, W.L. The Many Roles of Computation in Drug Discovery. *Science* **2004**, *303*, 1813–1818, doi:10.1126/science.1096361.

2. Ou-Yang, S.; Lu, J.; Kong, X.; Liang, Z.; Luo, C.; Jiang, H. Computational Drug Discovery. *Acta Pharmacol Sin* **2012**, *33*, 1131–1140, doi:10.1038/aps.2012.109.

3. Lombardino, J.G.; Lowe, J.A. The Role of the Medicinal Chemist in Drug Discovery — Then and Now. *Nat Rev Drug Discov* **2004**, *3*, 853–862, doi:10.1038/nrd1523.

4. Wess, G.; Urmann, M.; Sickenberger, B. Medicinal Chemistry: Challenges and Opportunities. *Angewandte Chemie International Edition* **2001**, *40*, 3341–3350, doi:https://doi.org/10.1002/1521-3773(20010917)40:18<3341::AID-ANIE3341>3.0.CO;2-D.

5. Walters, W.P.; Green, J.; Weiss, J.R.; Murcko, M.A. What Do Medicinal Chemists Actually Make? A 50-Year Retrospective. *J. Med. Chem.* **2011**, *54*, 6405–6416, doi:10.1021/jm200504p.

6. Russell, R.B.; Aloy, P. Targeting and Tinkering with Interaction Networks. *Nat Chem Biol* **2008**, *4*, 666–673, doi:10.1038/nchembio.119.

7. Pujol, A.; Mosca, R.; Farrés, J.; Aloy, P. Unveiling the Role of Network and Systems Biology in Drug Discovery. *Trends in Pharmacological Sciences* **2010**, *31*, 115–123, doi:10.1016/j.tips.2009.11.006.

8. Morgan, P.; Brown, D.G.; Lennard, S.; Anderton, M.J.; Barrett, J.C.; Eriksson, U.; Fidock, M.; Hamrén, B.; Johnson, A.; March, R.E.; et al. Impact of a Five-Dimensional Framework on R&D Productivity at AstraZeneca. *Nature Reviews Drug Discovery* **2018**, *17*, 167–181, doi:10.1038/nrd.2017.244.

9. Androulakis, I.P. Systems Engineering Meets Quantitative Systems Pharmacology: From Low-Level Targets to Engaging the Host Defenses. *WIREs Systems Biology and Medicine* **2015**, *7*, 101–112, doi:10.1002/wsbm.1294.

10. Wang, G.; Yuan, R.; Zhu, X.; Ao, P. Endogenous Molecular-Cellular Network Cancer Theory: A Systems Biology Approach. *Methods Mol Biol* **2018**, *1702*, 215–245, doi:10.1007/978-1-4939-7456-6_11.

11. DeWard, A.; Critchley-Thorne, R.J. Systems Biology Approaches in Cancer Pathology. *Methods Mol Biol* **2018**, *1711*, 261–273, doi:10.1007/978-1-4939-7493-1_13.

12. Krzyzanski, W. Systems Pharmacology Models for Guiding Drug Design. *CPT: Pharmacometrics & Systems Pharmacology* **2013**, *2*, 39, doi:10.1038/psp.2013.15.

13. Stein, M.; Gabdoulline, R.R.; Wade, R.C. Bridging from Molecular Simulation to Biochemical Networks. *Current Opinion in Structural Biology* **2007**, *17*, 166–172, doi:10.1016/j.sbi.2007.03.014.

14. Chang, C.; Poteet, E.; Schetz, J.A.; Gümüş, Z.H.; Weinstein, H. Towards a Quantitative Representation of the Cell Signaling Mechanisms of Hallucinogens: Measurement and Mathematical Modeling of 5-HT1A and 5-HT2A Receptor-Mediated ERK1/2 Activation. *Neuropharmacology* **2009**, *56*, 213–225, doi:10.1016/j.neuropharm.2008.07.049.

15. Nair, A.G.; Gutierrez-Arenas, O.; Eriksson, O.; Vincent, P.; Hellgren Kotaleski, J. Sensing Positive versus Negative Reward Signals through Adenylyl Cyclase-Coupled GPCRs in Direct and Indirect Pathway Striatal Medium Spiny Neurons. *J Neurosci* **2015**, *35*, 14017–14030, doi:10.1523/JNEUROSCI.0730-15.2015.

16. Dell'Orco, D.; Schmidt, H.; Mariani, S.; Fanelli, F. Network-Level Analysis of Light Adaptation in Rod Cells under Normal and Altered Conditions. *Mol. BioSyst.* **2009**, *5*, 1232, doi:10.1039/b908123b.

17. Invergo, B.M.; Montanucci, L.; Koch, K.-W.; Bertranpetit, J.; Dell'Orco, D. Exploring the Rate-Limiting Steps in Visual Phototransduction Recovery by Bottom-up Kinetic Modeling. *Cell Commun Signal* **2013**, *11*, 36, doi:10.1186/1478-811X-11-36.

18. Invergo, B.M.; Dell'Orco, D.; Montanucci, L.; Koch, K.-W.; Bertranpetit, J. A Comprehensive Model of the Phototransduction Cascade in Mouse Rod Cells. *Mol. BioSyst.* **2014**, *10*, 1481–1489, doi:10.1039/C3MB70584F.

19. Kholodenko, B.N.; Demin, O.V.; Moehren, G.; Hoek, J.B. Quantification of Short Term Signaling by the Epidermal Growth Factor Receptor. *J. Biol. Chem.* **1999**, *274*, 30169–30181, doi:10.1074/jbc.274.42.30169.

20. Glont, M.; Nguyen, T.V.N.; Graesslin, M.; Hälke, R.; Ali, R.; Schramm, J.; Wimalaratne, S.M.; Kothamachu, V.B.; Rodriguez, N.; Swat, M.J.; et al. BioModels: Expanding Horizons to Include More Modelling Approaches and Formats. *Nucleic Acids Research* **2018**, *46*, D1248–D1253, doi:10.1093/nar/gkx1023.

21. Malik-Sheriff, R.S.; Glont, M.; Nguyen, T.V.N.; Tiwari, K.; Roberts, M.G.; Xavier, A.; Vu, M.T.; Men, J.; Maire, M.; Kananathan, S.; et al. BioModels—15 Years of Sharing Computational Models in Life Science. *Nucleic Acids Research* **2020**, *48*, D407–D415, doi:10.1093/nar/gkz1055.

22. Xie, L.; Ge, X.; Tan, H.; Xie, L.; Zhang, Y.; Hart, T.; Yang, X.; Bourne, P.E. Towards Structural Systems Pharmacology to Study Complex Diseases and Personalized Medicine. *PLoS Comput Biol* **2014**, *10*, doi:10.1371/journal.pcbi.1003554.

23. Birch, J.; Cheruvara, H.; Gamage, N.; Harrison, P.J.; Lithgo, R.; Quigley, A. Changes in Membrane Protein Structural Biology. *Biology* **2020**, *9*, 401, doi:10.3390/biology9110401.

24. Duran-Frigola, M.; Mosca, R.; Aloy, P. Structural Systems Pharmacology: The Role of 3D Structures in Next-Generation Drug Development. *Chemistry & Biology* **2013**, *20*, 674–684, doi:10.1016/j.chembiol.2013.03.004.

25. De Vivo, M.; Masetti, M.; Bottegoni, G.; Cavalli, A. Role of Molecular Dynamics and Related Methods in Drug Discovery. *J. Med. Chem.* **2016**, *59*, 4035–4061, doi:10.1021/acs.jmedchem.5b01684.

26. Bruce, N.J.; Ganotra, G.K.; Kokh, D.B.; Sadiq, S.K.; Wade, R.C. New Approaches for Computing Ligand–Receptor Binding Kinetics. *Current Opinion in Structural Biology* **2018**, *49*, 1–10, doi:10.1016/j.sbi.2017.10.001.

27. Nunes-Alves, A.; Kokh, D.B.; Wade, R.C. Recent Progress in Molecular Simulation Methods for Drug Binding Kinetics. *Current Opinion in Structural Biology* **2020**, *64*, 126–133, doi:10.1016/j.sbi.2020.06.022.

28. Capelli, R.; Lyu, W.; Bolnykh, V.; Meloni, S.; Olsen, J.M.H.; Rothlisberger, U.; Parrinello, M.; Carloni, P. On the Accuracy of Molecular Simulation-Based Predictions of Koff Values: A Metadynamics Study. *bioRxiv* **2020**, 2020.03.30.015396, doi:10.1101/2020.03.30.015396.

29. Liu, Z.; Su, M.; Han, L.; Liu, J.; Yang, Q.; Li, Y.; Wang, R. Forging the Basis for Developing Protein–Ligand Interaction Scoring Functions. *Acc. Chem. Res.* **2017**, *50*, 302–309, doi:10.1021/acs.accounts.6b00491.

30. Ragoza, M.; Hochuli, J.; Idrobo, E.; Sunseri, J.; Koes, D.R. Protein–Ligand Scoring with Convolutional Neural Networks. *J. Chem. Inf. Model.* **2017**, *57*, 942–957, doi:10.1021/acs.jcim.6b00740.

CHAPTER 2

About this thesis

The research aims of this thesis rely on the pharmacological study of post-synaptic receptors. Hereby, I intend to correlate the intracellular effects of the activation of neurosignaling cascades upon ligand binding to neuroreceptors applying a structure-quantitative systems pharmacology approach.

Having seen that, in the systems biology community, there is a lack of a common language to annotate, exchange, reuse and update biochemical network models, I was prompted to build a common framework to integrate structure and quantitative systems pharmacology approaches. The goal is, thereby, to build a computational platform to predict individual and context-specific drug response phenotypes by correlating molecular interactions with cellular functions.

This thesis is then divided in two main parts. In *Part I – Network and systems biology in structure-function studies of neuroreceptors.* I present two distinct studies where signaling pathways are used to explore the subcellular effects upon receptor activation. The intention is to illustrate how merging structural macromolecular data with network biology allow us to understand complex biological phenomena. Firstly, in *Chapter 3*, I start by presenting the development and implementation of the signaling pathway of the oxytocin receptor in order to provide a rationale on the structure-function relationships of a disease variant of that receptor. Then, in *Chapter 4*, I present a mechanistic model for NMDA and AMPA receptors mediated-synaptic transmission in individual hippocampal synapses, with which the functional impact caused by disease associated variants of NMDA receptors related to severe cognitive impairment is predicted.

In *Part II - Pharmacology modeling and simulation workflows: integrating tools to create and investigate pharmacological models*, the aim is to integrate the state-of-the-art open-source structural bioinformatic tools in a systems pharmacology platform. Specifically, in *Chapter 5*, structural-quantitative systems pharmacology protocols for the prediction of classical pharmacodynamic models towards G-protein coupled receptors (class A) are proposed. In *Chapter 6*, instead, the conceptual idea of assembling a biocomputing platform to settle a new drug discovery pipeline towards those receptors is presented. The aim is building a web-interface platform that implements the protocols proposed on *Chapter 5* interconnected with more computational-demanding structure systems biology web-services.

In the end, the intention is to create a biocomputing platform designed for in-depth studies of post-synaptic neuroreceptors, in particular G-protein coupled receptors (class A), in order to improve current empirically driven drug discovery approaches in a more precise drug design.

Part I

Network and systems biology in structure-function studies of neuroreceptors

CHAPTER 3

Systems biology modeling of the G_q-activated Ca^{2+} signals at the Endoplasmic Reticulum

This chapter describes my contribution to: Structure-function relationships of the disease-linked A218T oxytocin receptor variant; M. Meyer, B. Jurek, M. Alfonso-Prieto, ***R. Ribeiro****, V. Milenkovic, J. Winter, P. Hoffmann, C. H. Wetzel, A. Giorgetti, P. Carloni, I. D. Neumann; submitted.*

3.1 Introduction

The neuropeptide oxytocin (OXT) regulates multiple social and emotional behaviors, such as social bonding, reciprocal trust, aggression, fear and anxiety, both in animals and humans [1,2]. For example, synthetic OXT, intranasally applied, improves social impairments of autistic children [3,4] and has been suggested as a biomarker and target for the treatment of autism spectrum disorder (ASD) [5]. Unfortunately, however, the therapeutic efficacy is highly variable across individuals [6].

OXT exerts its function by binding to its target receptor (OXTR), a member of the Class A G-protein coupled receptors (GPCR) family. Single nucleotide polymorphisms (SNPs) in the gene encoding for OXTR have been associated with a plethora of psychological traits in genome-wide association studies (GWAS). Although most of the described disease-associated SNPs are intronic and/or synonymous mutations [1], non-synonymous SNPs (nsSNPs), which are likely to affect OXTR structure and function, have also been associated with severe psychopathological conditions of ASD. This is the case for the rs4686302 nsSNP, which has been associated with deficits in social communication and cognition, as well as restricted and repetitive behaviors [7,8], along with differences in emotional empathy in a non-clinical Chinese cohort [9]. Another study investigated the association of the rs4686302 nsSNP with premature birth, as well as reduced cesarean section prevalence, and found that this variant results in increased contractility upon OXT stimulation in human myometrium biopsies [10].

The nsSNP rs4686302 is located within the coding region of exon 3 in the human *OXTR* gene, leading to an amino acid exchange of alanine to threonine at position 218 (A218T) of the OXTR protein. Intriguingly, *in silico* sequence-based predictions of the functional significance of this variant did not identify it as damaging [11], in contrast to the observed phenotype. Thus, shedding light on the functional consequences of nsSNP rs4686302 is crucial to assemble a comprehensive model of subcellular effects that may ultimately affect complex behavioral traits associated with ASD.

Here, we propose a systems biology model of the signaling pathway of OXTR in order to give a better understand behind the difference on dynamics of the intracellular Ca^{2+} between the OXTR-WT and OXTR-A218T observed experimentally, and on the impact of the downstream events. However, to the best of our knowledge, there isn't a mathematical system biology model of the OXTR signaling pathway available in the literature that allows the simulation of the IP_3-mediated Ca^{2+} release from internal storages stimulated by the receptor. For this reason, we integrated two existing models: a model of G_q type

G-protein signaling pathway and a model of the dynamics of the IP_3-mediated Ca^2 release from endoplasmic reticulum.

3.2 The OXTR associated signaling pathway

OXTRs are able to couple to different G-proteins. OXTR-mediated activation of $G_{\alpha q}$, $G_{\alpha o}$, and $G_{\alpha i}$ -proteins affect, together with the $G_{\beta\gamma}$ subunit, a diversity of signaling cascades (such as the PLC, PKA, PKC, DAG kinase, MAPK, CaMK, and PI4-Kinase-Rho pathways), as well as membrane ion channels (conducting calcium, potassium and sodium) [1,12]. These pathways will, consequently, converge on the activation of transcription factors like CREB or MEF-2, which, depending on the G-protein coupling, can transduce growth-inhibitory or proliferatory signals [1], *Fig. 3.1*.

The specific coupling of the different G proteins to the receptor, and consequently the triggered physiological effect, is determined by the expression level of the individual G proteins and the local ligand concentration [13]. *Busnelli et al.* have demonstrated that the G_q-mediated pathways are the first

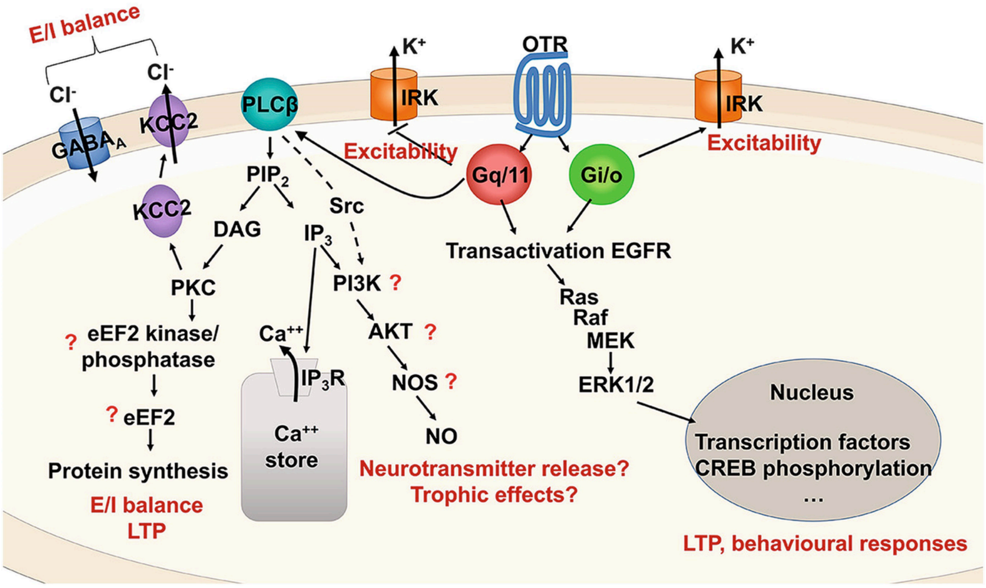

Fig 3.1 Signaling pathway of the OXTR. Figure taken from *Busnelli and Chini 2017* [13].

to be triggered at low OXT concentrations, whereas activation of the $G_{i/o}$-mediated pathways needs at least a 10-fold higher OXT concentration [14]. Indeed, it has been proposed that, at such high OXT concentrations, all the activated G-proteins may act synergistically, causing a rapid desensitization of the OXTR [15].

At low concentrations values of OXT [14] the G_q-mediated pathway is triggered. Both the G_q-α and G_q-βγ subunits activate phospholipase C beta (PLC-β), which consequently generates inositol-1,4,5-trisphosphate (IP_3) and diacylglycerol (DAG) from phosphatidylinositol 4,5-bisphosphate (PIP_2). IP_3, as well as other phospholipid metabolites, are implicated in the release of Ca^{2+} from internal stores, especially from the endoplasmic reticulum (ER). This was experimentally measured by our collaborators using Ca^{2+} imaging techniques for both WT and A218T cells in a Ca^{2+}-free Ringer medium (*Fig. 3.2*). The IP_3-dependent release of Ca^{2+} from the ER is mediated by IP_3 receptors (IP_3Rs) expressed on the organelle membrane. However, this Ca^{2+} release mechanism is also governed by the Ca^{2+} itself, making this dual activation of IP_3Rs central for the oscillatory nature of the intracellular concentration of Ca^{2+} [16]. DAG, together with Ca^{2+}, activates the phosphokinase C (PKC) that, in turn, activates the MAPK pathway [1], in particular phosphorylation of ERK1/2.

At higher OXT concentrations [14], the $G_{i/o}$ proteins coupled to the OXTR are also activated, affecting kinase pathways and membrane ion channels' activity. Some $G_{i/o}$-α subunit isoforms and $G_{i/o}$-βγ subunits directly inhibit adenylyl cyclase, reducing the intracellular levels of cAMP and affecting the activation of PKA. In addition, the $G_{i/o}$-α subunits can also interfere with PKA function indirectly, by altering its nuclear translocation [12]. Although not yet demonstrated in mammalian cells, evidence in *C. elegans* indicated that the G_o-α subunits trigger a decrease in the levels of DAG, acting on the DAG kinase pathway. Since activation of PKC is highly dependent on DAG, G_o-α subunits thus indirectly inhibit PKC [12]. Taking also into account that phosphorylation of IP_3Rs by PKA and PKC plays an important role in modulation of IP_3-induced Ca^{2+} signals [17], the effect on PKA/C by activation of $G_{i/o}$ proteins might not affect the generation and regulation of IP_3-induced Ca^{2+} signals by IP_3Rs, but rather have a modulatory effect [12,18].

The direct activation of PLC-β by $G_{i/o}$ proteins has been shown to be mediated through the βγ subunit. However, the general rapid desensitization of the $G_{i/o}$ signaling implies that the concentration of IP_3 generated by PLC-β activation mediated by $G_{i/o}$-βγ subunit will be too low to generate a robust Ca^{2+}-release from ER [15].

Altogether, activation of $G_{i/o}$ proteins will have a very limited contribution to the IP_3-mediated Ca^{2+} signals at the ER. Moreover, the very low expression of G_o proteins in HEK293 cells [19], used in the experiments presented here, will further minimize their contribution. Therefore, in our experimental setup, the regulation of the IP_3-mediated Ca^{2+} signals at the ER is probably mainly due to the activation of the G_q-mediated pathway.

3.3 Methods

The cascade from OXT-triggered G_q activation to the downstream Ca^{2+} release from the ER through IP_3R was modeled by integrating two previously existing mathematical models: (i) a model of the activation of the eukaryotic MAPK pathway (via PKC/Raf-1) upon serotonin 2A receptor activation [20]; and (ii) a dynamic model of the IP_3R action, with a change in Ca^{2+} and IP_3 concentrations resulting in intracellular Ca^{2+} oscillations [21]. The equations and kinetic constants for each of the reactions of the systems biology model developed here are shown in *Tab. 3.A2*. Namely, we selected from model (i) [20] the reactions upstream from the production of IP_3 by PLC-β. This is the crossroad with model (ii) [21], which dynamically simulates the IP_3 and Ca^{2+}-dependent Ca^{2+} release from the ER into the cytosol. In particular, *Keizer and De Young* proposed a simple model [21] to account for both IP_3 stimulation and Ca^{2+} inhibition by considering the IP_3R as a homotetramer, in which each subunit has one binding site for IP_3 and one for the Ca^{2+}. Each subunit can thus exist in one of four states: S_0 (unbound), S_1 (bound to IP_3), S_2 (bound to Ca^{2+}), and S_3

(bound to IP_3 and Ca^{2+}); however, channel opening requires all four subunits to be in state S_1. Under such assumptions, *Keiser and De Young* [21] defined the flux of Ca^{2+} through the IP_3R as proportional to the open probability for one IP_3R at equilibrium. Considering that the species in each deterministic reaction of our model are expressed in concentration values (*Tab. 3.A3*), we defined the IP_3R open probability as the equilibrium fraction of subunits in state S_1 (see [IP₃R_IP₃] in reaction 22 in *Tab. 3.A2*).

Our model was developed under the *PySB* framework [22] and integrated using the *SciPy* ODE numerical integrator [23]. The results were analyzed using *NumPy* [24], *SciPy* [23] and *scikit-learn* [25] libraries. All the simulations and analysis codes were written and run in a *Jupyter* notebook [26] (available at *https://github.com/rribeiro-sci/OXTR.git*).

3.4 Results

The systems biology model described above was used to rationalize the experimentally measured Ca^{2+} concentrations with 100 nM OXT and in the absence of extracellular Ca^{2+} (*Fig. 3.2 E,* blue bars). Simulation's parameters and initial concentrations of the model are provided in *Tab. 3.A1* and *Tab. 3.A3*. Since the molecular modeling results had suggested that the A218T variant affects receptor activation (not shown here), we modified the forward kinetic constant of reaction 3 in *Tab. 3.A2*. This parameter describes G_q-protein binding to the receptor, which implicitly depends on receptor activation. We introduced a scaling factor, so that this kinetic constant remains unmodified for WT OXTR (*kf_coupling_wt* = 1), whereas it is adjusted for the A218T mutant (*kf_coupling_mut* = variable) to attempt to simulate the experimentally observed higher Ca^{2+} signal in A218T compared with WT cells incubated in Ca^{2+}-free Ringer (*Fig. 3.2 E*).

Simply scaling, by trial and error, the *kf_coupling_mut* by a factor of 1.45, our *in silico* model is able to reproduce the shape of the experimental Ca^{2+}

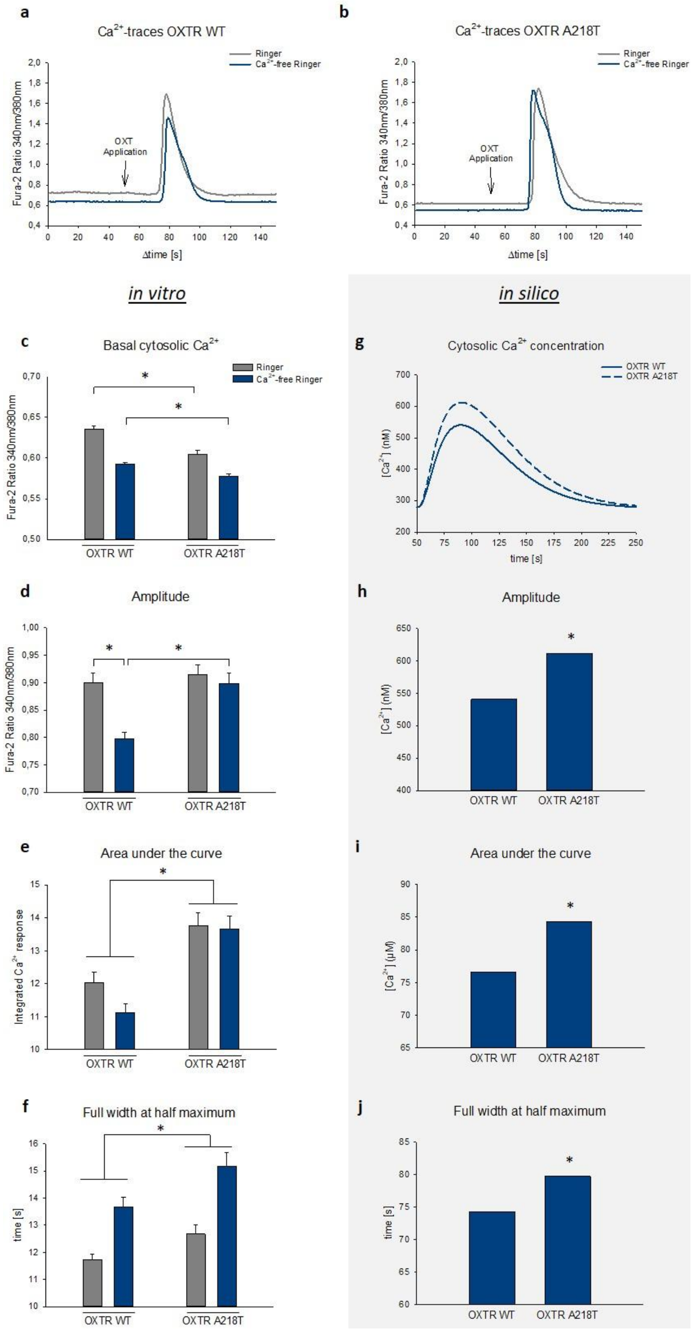

Fig. 3.2 Intracellular Ca2+ dynamics in the OXTR WT and A218T variant *in vitro* and *in silico*. **A)** and **B)**, representative Ca^{2+}-traces of OXTR WT or A218T cells upon stimulation with 100 nM OXT in Ca^{2+}-containing (grey line) or Ca^{2+}-free (blue line) Ringer's solution. **C)**, Basal cytosolic Ca^{2+} levels of OXTR WT and A218T cells. **D)** mean amplitude of OXT-induced Ca^{2+}-signals in Ca^{2+}-free and Ca^{2+}-containing Ringer's solution in WT and mutant cells. **E)** mean area under the curve calculated as integral over time above baseline in OXTR A218T compared to OXTR WT cells under both conditions. **F)** two-way ANOVA revealed a main effect between the cell lines regarding the full width at half maximum. **G)** graphical representation of the simulation curves of Ca^{2+} concentration upon stimulation with OXT in Ca^{2+}-free Ringer's solution. **H)** Maximal amplitude of OXT-induced Ca^{2+} simulation curves' peaks of OXTR WT and A218T. $*$ ratio = 1.13. **I)** area under simulation's curves of OXTR WT and A218T. $*$ ratio = 1.10. J, FWHM of the OXT-induced Ca^{2+} simulation's curves of OXTR WT and OXTR A218T. $*$ ratio = 1.07. **C)**, **D)**, **E)** and **F)**, Bars show mean + SEM in presence (grey bars) or absence (blue bars) of extracellular Ca^{2+}.

concentration curves (*Fig. 3.2 E*) and the ratio between the WT and A218T OXTR amplitudes (*Fig. 3.2 D*). The calculated WT/A218T ratios for the AUC and full width at half maximum (*Fig. 3.2 H* and *3.2 J*) are also in agreement with the experimental results (*Fig. 3.2 G* and *3.2 I*).

3.5 Discussion

Autism is a multifactorial neurodevelopmental disorder. Although various SNPs in the OXTR, including the A218T variant, have been associated with ASD symptoms, a comprehensive understanding of the molecular consequences are not yet fully understood, but essential to promote the development of an effective treatment. Understanding the chain of intracellular events caused by disease-linked mutations may provide a “master-regulator” in the ASD pathway that could be exploited for clinical treatment options.

Here, using a computational systems biology modeling approach, we help to unravel key subcellular consequences of expression of the pathological OXTR variant A218T. We show that the change in receptor activation caused by the mutation might be the key factor for the observed changes in intracellular Ca^{2+} concentrations. The observed differences in Ca^{2+} dynamics might play an important role in maintaining downstream signal specificity, *e.g.*, in the MAPK cascade (not shown here), which will likely result in changes in gene expression.

Although our model is able to qualitatively predict a relative change in the concentration of Ca^{2+} comparable with the experimental data, one should keep in mind that it was developed based on two previous independent models. Some of the kinetic constants in those models were tuned in order to mimic specific experimental data for other GPCRs. Hence, future improvements of our model should involve fitting of kinetic constants to experimental data obtained for the OXTR signaling pathway. Moreover, since the activation of the MAPK/ERK pathway depends also on the extracellular Ca^{2+} and on the activation of the epidermal growth factor receptor (EGFR), further extensions of our model should incorporate these secondary pathways. Therefore, future improvements of the cascade description need to include this possibility.

3.6 Appendix

Tab. 3.A1 Simulation Parameters.

Parameter	Value	Description
ttotal	250 s	total simulation time
nsteps	10000	number integration steps
time_in, time_out	50 s, 51 s	time of the simulation in which OXT can bind to OXTR
kf_coupling_wt, kf_coupling_mut	1, variable	Scaling factor that multiplies the forward kinetic constant of reaction 3 in *Tab. 3.A2*. See text for more details.

Tab. 3.A2 Equations and kinetic constants for each of the reactions of the proposed mathematical model of the OXTR signaling pathway.

	Reaction	Parameters		Ref.
		Kinetic forward constant	Kinetic reverse constant	
1	$R + L \rightleftharpoons RL$	$1.00\ \mu M^{-1}s^{-1}$	$2.50\ s^{-1}$	[20]
2	$R + G_{\alpha\beta/\gamma} \rightleftharpoons R\_G_{\alpha\beta/\gamma}$	$1.00\ \mu M^{-1}s^{-1}$	$1.67\ s^{-1}$	[20]
3	$RL + G_{\alpha\beta/\gamma} \rightleftharpoons RL\_G_{\alpha\beta/\gamma}$	$1.00\ \mu M^{-1}s^{-1}$	$0.0046\ s^{-1}$	[20]
4	$G_{\alpha} + G_{\beta/\gamma} \rightleftharpoons G_{\alpha\beta/\gamma}$	$6.00\ \mu M^{-1}s^{-1}$	$0.0001\ s^{-1}$	[20]
5	$RL\_G_{\alpha\beta/\gamma} \longrightarrow RL + G_{\alpha\text{-GTP}} + G_{\beta/\gamma}$	$0.04\ s^{-1}$	-	[20]
6	$RGS4 + G_{\alpha\text{-GTP}} \rightleftharpoons RGS4\_G_{\alpha\text{-GTP}}$	$20.83\ \mu M^{-1}s^{-1}$	$33.32\ s^{-1}$	[20]
7	$RGS4\_G_{\alpha\text{-GTP}} \longrightarrow RGS4 + G_{\alpha}$	$8.33\ s^{-1}$	-	[20]
8	$G_{\alpha\text{-GTP}} \longrightarrow G_{\alpha}$	$0.01\ s^{-1}$	-	[20]
9	$PLC\beta + G_{\alpha\text{-GTP}} \rightleftharpoons PLC\beta\_G_{\alpha\text{-GTP}}$	$2.52\ \mu M^{-1}s^{-1}$	$1.00\ s^{-1}$	[20]
10	$PLC\beta\_G_{\alpha\text{-GTP}} + Ca_i^{2+} \rightleftharpoons PLC\beta\_G_{\alpha\text{-GTP}}\_Ca$	$30.00\ \mu M^{-1}s^{-1}$	$1.00\ s^{-1}$	[20]
11	$PLC\beta\_G_{\alpha}\text{-GTP}\_Ca \longrightarrow PLC\beta\_Ca + G_{\alpha}$	$0.013\ s^{-1}$	-	[20]
12	$PLC\beta + Ca_i^{2+} \rightleftharpoons PLC\beta\_Ca$	$3.00\ \mu M^{-1}s^{-1}$	$1.00\ s^{-1}$	[20]
13	$PLC\beta\_Ca + Ga_{\text{-GTP}} \rightleftharpoons PLC\beta\_G_{\alpha}\text{-GTP}\_Ca$	$25.20\ \mu M^{-1}s^{-1}$	$1.00\ s^{-1}$	[20]
14	$PLC\beta\_G_{\alpha\text{-GTP}}\_Ca + PIP_2 \longrightarrow PLC\beta\_G_{\alpha}\text{-GTP}\_Ca + IP_3 + DAG$	$\frac{48.0[PIP_2]}{5.00 + [PIP_2]}$	-	[20]
15	$PLC\beta\_Ca + PIP_2 \longrightarrow PLC\beta\_Ca + IP_3 + DAG$	$\frac{10.0[PIP_2]}{40.13 + [PIP_2]}$	-	[20]
16	$IP_3 \longrightarrow null$	$\frac{0.14([IP_3] - [IP_3]_{initial})}{[IP_3]}$	-	[20]
17	$DAG \longrightarrow null$	0.15	-	[20]
18	$IP_3R + IP_3 \rightleftharpoons IP_3R\_IP_3$	$50.00\ \mu M^{-1}s^{-1}$	$6.50\ s^{-1}$	[21]
19	$IP_3R + Ca_i^{2+} \rightleftharpoons IP_3R\_Ca$	$20.00\ \mu M^{-1}s^{-1}$	$0.0806\ s^{-1}$	[21]
20	$IP_3R\_IP_3 + Ca_i^{2+} \rightleftharpoons IP_3R\_IP_3\_Ca$	$1.00\ \mu M^{-1}s^{-1}$	$0.50\ s^{-1}$	[21]
21	$IP_3R\_Ca + IP_3 \rightleftharpoons IP_3R\_IP_3\_Ca$	$20.00\ \mu M^{-1}s^{-1}$	$14.50\ s^{-1}$	[21]
22	$Ca_{ER}^{2+} \longrightarrow Ca_i^{2+}$	$\frac{0.185\left(800\left(\frac{[IP_3R\_IP_3]}{[IP_3R]_{initial}}\right)^4 + 0.15\right)\left([Ca_{ER}^{2+}] - [Ca_i^{2+}]\right) - 0.5\frac{[Ca_i^{2+}]^2}{[Ca_i^{2+}]^2 + 0.09^2}}{[Ca_{ER}^{2+}]}$	-	[21]

Tab. 3.A3 Initial concentrations of each of the species in the mathematical model.

Parameter	**Value (μM)**	**Reference**
R_{init}	1.4107	[20]
L_{init}	0.1	OXT concentration used in the experiments presented in this work
G_{init}	0.0027739	[20]
$G\alpha\text{-}GTP_{init}$	6.4172E-4	[20]
$G\beta\gamma_{init}$	0.0037173	[20]
$R\_G\alpha\beta\gamma_{init}$	0.27*Rinit	[20]
$G\alpha\beta\gamma_{init}$	0.61869	[20]
$RGS4_{init}$	0.019994	[20]
$RGS4\_G\alpha\text{-}GTP_{init}$	6.4168E-6	[20]
$Ca_i^{2+}{}_{init}$	0.1*	[21]
$Ca_{ER}^{2+}{}_{init}$	1	-
$PLC\beta_{init}$	0.090022	[20]
$PLC\beta\_G\alpha\_GTP_{init}$	1.4492E-4	[20]
$PLC\beta\_Ca_{init}$	0.0093825	[20]
$PLC\beta\_Ca\_G\_GTP_{init}$	1.5038E-4	[20]
PIP_{2init}	2.6578	[20]
IP_{3init}	0.21952	[20]
DAG_{init}	0.055555	[20]
IP_3R_{init}	0.119	[16]

*Value chosen according to the resting value of cytosolic calcium concentration present in typical experiments for a variety of cells (50-100 nM) [21] that ensures the correct parameters for the reaction 22 of *Tab. 3.A2*.

References

1. Jurek, B.; Neumann, I.D. The Oxytocin Receptor: From Intracellular Signaling to Behavior. Physiol. Rev. 2018, 98, 1805–1908, doi:10.1152/physrev.00031.2017.

2. Grinevich, V.; Neumann, I.D. Brain Oxytocin: How Puzzle Stones from Animal Studies Translate into Psychiatry. Mol Psychiatry 2020, doi:10.1038/s41380-020-0802-9.

3. Parker, K.J.; Garner, J.P.; Libove, R.A.; Hyde, S.A.; Hornbeak, K.B.; Carson, D.S.; Liao, C.-P.; Phillips, J.M.; Hallmayer, J.F.; Hardan, A.Y. Plasma Oxytocin Concentrations and OXTR Polymorphisms Predict Social Impairments in Children with and without Autism Spectrum Disorder. Proceedings of the National Academy of Sciences 2014, 111, 12258–12263, doi:10.1073/pnas.1402236111.

4. Parker, K.J.; Oztan, O.; Libove, R.A.; Sumiyoshi, R.D.; Jackson, L.P.; Karhson, D.S.; Summers, J.E.; Hinman, K.E.; Motonaga, K.S.; Phillips, J.M.; et al. Intranasal Oxytocin Treatment for Social Deficits and Biomarkers of Response in Children with Autism. Proc Natl Acad Sci USA 2017, 114, 8119–8124, doi:10.1073/pnas.1705521114.

5. Guastella, A.J.; Hickie, I.B. Oxytocin Treatment, Circuitry, and Autism: A Critical Review of the Literature Placing Oxytocin Into the Autism Context. Biological Psychiatry 2016, 79, 234–242, doi:10.1016/j.biopsych.2015.06.028.

6. Bakermans-Kranenburg, M.J.; van IJzendoorn, M.H. A Sociability Gene? Meta-Analysis of Oxytocin Receptor Genotype Effects in Humans: Psychiatric Genetics 2014, 24, 45–51, doi:10.1097/YPG.0b013e3283643684.

7. Francis, S.M.; Kim, S.-J.; Kistner-Griffin, E.; Guter, S.; Cook, E.H.; Jacob, S. ASD and Genetic Associations with Receptors for Oxytocin and Vasopressin—AVPR1A, AVPR1B, and OXTR. Front. Neurosci. 2016, 10, doi:10.3389/fnins.2016.00516.

8. Kalyoncu, T.; Özbaran, B.; Köse, S.; Onay, H. Variation in the Oxytocin Receptor Gene Is Associated With Social Cognition and ADHD. J Atten Disord 2019, 23, 702–711, doi:10.1177/1087054717706757.

9. Wu, N.; Li, Z.; Su, Y. The Association between Oxytocin Receptor Gene Polymorphism (OXTR) and Trait Empathy. Journal of Affective Disorders 2012, 138, 468–472, doi:10.1016/j.jad.2012.01.009.

10. Füeg, F.; Santos, S.; Haslinger, C.; Stoiber, B.; Schäffer, L.; Grünblatt, E.; Zimmermann, R.; Simões-Wüst, A.P. Influence of Oxytocin Receptor Single Nucleotide Sequence Variants on Contractility of Human Myometrium: An in Vitro Functional Study. BMC Med Genet 2019, 20, 178, doi:10.1186/s12881-019-0894-8.

11. Kim, J.; Stirling, K.J.; Cooper, M.E.; Ascoli, M.; Momany, A.M.; McDonald, E.L.; Ryckman, K.K.; Rhea, L.; Schaa, K.L.; Cosentino, V.; et al. Sequence Variants in Oxytocin Pathway Genes and Preterm Birth: A Candidate Gene Association Study. BMC Med Genet 2013, 14, 77, doi:10.1186/1471-2350-14-77.

12. Jiang, M.; Bajpayee, N.S. Molecular Mechanisms of Go Signaling. NSG 2009, 17, 23–41, doi:10.1159/000186688.

13. Busnelli, M.; Chini, B. Molecular Basis of Oxytocin Receptor Signalling in the Brain: What We Know and What We Need to Know. In Behavioral Pharmacology of Neuropeptides: Oxytocin; Hurlemann, R., Grinevich, V., Eds.; Current Topics in Behavioral Neurosciences; Springer International Publishing: Cham, 2017; Vol. 35, pp. 3–29 ISBN 978-3-319-63738-9.

14. Busnelli, M.; Saulière, A.; Manning, M.; Bouvier, M.; Galés, C.; Chini, B. Functional Selective Oxytocin-Derived Agonists Discriminate between Individual G Protein Family Subtypes. J. Biol. Chem. 2012, 287, 3617–3629, doi:10.1074/jbc.M111.277178.

15. Van-Ham, I.I.; Oron, Y. Go G-proteins mediate rapid heterologous desensitization of G-protein coupled receptors in Xenopus oocytes. Journal of Cellular Physiology 2005, 204, 455–462, doi:10.1002/jcp.20341.

16. Taylor, C.W.; Konieczny, V. IP3 Receptors: Take Four IP3 to Open. Sci. Signal. 2016, 9, pe1–pe1, doi:10.1126/scisignal.aaf6029.

17. Vermassen, E.; Fissore, R.A.; Nadif Kasri, N.; Vanderheyden, V.; Callewaert, G.; Missiaen, L.; Parys, J.B.; Smedt, H.D. Regulation of the Phosphorylation of the Inositol 1,4,5-Trisphosphate Receptor by Protein Kinase C. Biochemical and Biophysical Research Communications 2004, 319, 888–893, doi:10.1016/j.bbrc.2004.05.071.

18. Xie, R.; Li, L.; Goshima, Y.; Strittmatter, S.M. An Activated Mutant of the a Subunit of Go Increases Neurite Outgrowth via Protein Kinase C. Developmental Brain Research 1995, 87, 77–86, doi:10.1016/0165-3806(95)00061-H.

19. Atwood, B.K.; Lopez, J.; Wager-Miller, J.; Mackie, K.; Straiker, A. Expression of G Protein-Coupled Receptors and Related Proteins in HEK293, AtT20, BV2, and N18 Cell Lines as Revealed by Microarray Analysis. BMC Genomics 2011, 12, 14, doi:10.1186/1471-2164-12-14.

20. Chang, C.; Poteet, E.; Schetz, J.A.; Gümüş, Z.H.; Weinstein, H. Towards a Quantitative Representation of the Cell Signaling Mechanisms of Hallucinogens: Measurement and Mathematical Modeling of 5-HT1A and 5-HT2A Receptor-Mediated ERK1/2 Activation. Neuropharmacology 2009, 56, 213–225, doi:10.1016/j.neuropharm.2008.07.049.

21. Keizer, J.; De Young, G.W. Two Roles of Ca2+ in Agonist Stimulated Ca2+ Oscillations. Biophys J 1992, 61, 649–660.

22. Lopez, C.F.; Muhlich, J.L.; Bachman, J.A.; Sorger, P.K. Programming Biological Models in Python Using PySB. Mol Syst Biol 2013, 9, 646, doi:10.1038/msb.2013.1.

23. Virtanen, P.; Gommers, R.; Oliphant, T.E.; Haberland, M.; Reddy, T.; Cournapeau, D.; Burovski, E.; Peterson, P.; Weckesser, W.; Bright, J.; et al. SciPy 1.0: Fundamental Algorithms for Scientific Computing in Python. Nat Methods 2020, 17, 261–272, doi:10.1038/s41592-019-0686-2.

24. Harris, C.R.; Millman, K.J.; van der Walt, S.J.; Gommers, R.; Virtanen, P.; Cournapeau, D.; Wieser, E.; Taylor, J.; Berg, S.; Smith, N.J.; et al. Array Programming with NumPy. Nature 2020, 585, 357–362, doi:10.1038/s41586-020-2649-2.

25. Pedregosa, F.; Varoquaux, G.; Gramfort, A.; Michel, V.; Thirion, B.; Grisel, O.; Blondel, M.; Prettenhofer, P.; Weiss, R.; Dubourg, V.; et al. Scikit-Learn: Machine Learning in Python. J. Mach. Learn. Res. 2011, 12, 2825–2830.

26. Kluyver, T.; Ragan-Kelley, B.; Pérez, F.; Granger, B.; Bussonnier, M.; Frederic, J.; Kelley, K.; Hamrick, J.; Grout, J.; Corlay, S.; et al. Jupyter Notebooks - a Publishing Format for Reproducible Computational Workflows. In Proceedings of the Positioning and Power in Academic Publishing: Players, Agents and Agendas; Loizides, F., Scmidt, B., Eds.; IOS Press, 2016; pp. 87–90.

CHAPTER 4

A mechanistic model of NMDA and AMPA receptors-mediated synaptic transmission in individual hippocampal CA3-CA1 synapses

The work described in this chapter is taken from: P. Micheli[*]*,* ***R. Ribeiro***[*†]*, A Giorgetti*[†]*; A Mechanistic Model of NMDA and AMPA Receptors-Mediated Synaptic Transmission in Individual Hippocampal CA3-CA1 Synapses: A Computational Multiscale Approach. Int. J. Mol. Sci. 2021, 22, 1536. https://doi.org/ 10.3390/ijms22041536.*

4.1 Introduction

Ionotropic glutamatergic receptors are a class of membrane receptors divided in three main subtypes classified according to their activation to the selective agonists: NMDA, AMPA, and Kainato. They play a key role in the process of synaptic transmission, which takes place in excitatory glutamatergic synapses,

---

[*] First author

[†] Correspondent author

and dysregulations in their normal activities have been widely linked to numerous neurological disorders and synaptopathies [1–5]. Particularly, NMDA and AMPA receptors have been identified as crucial in the molecular mechanism underlying the process of synaptic plasticity, a process that leads to the modulation in the strength of the neuronal response to stimulation, linked to learning and memory [6–8].

Complex cognitive functions such as learning and multiple forms of memory are carried out by the hippocampal formation, which can dynamically sample, encode, store and retrieve information coming from the sensory experience [9–11]. The constant encoding and integration of new information is possible thanks to the ability of a neural circuit to continuously reshape its topology and modulate the strength of its connections. In the hippocampal circuits, synaptic plasticity events that individual cells may undergo during synaptic transmissions occur in the form of Long Term Potentiation (LTP) and Long Term Depression (LTD). The trisynaptic circuit, particularly, has been extensively studied because of its apparently simple connectivity and the experimental accessibility of its structures. Inside this pathway, CA3 Shaffer collateral axons innervate CA1 pyramidal cells forming excitatory glutamatergic synapses (*Fig. 4.1*). The high density of NMDA receptors expressed on the surface of the dendritic CA1 spines confers to this synapse the ability to easily undergo NMDA receptor-mediated LTP and LTD, which has been substantially evidenced to be essential for some forms of explicit learning in mammals [12,13].

In Schaffer collateral-CA1 synapses, AMPA and NMDA receptors populate the membrane of CA1 spine, actively participating in synaptic transmission. AMPA receptors are GluR1-GluR4 containing homo/hetero-tetrameric receptors which mediate fast excitatory neurotransmission in glutamatergic synapses. Early phase of synaptic plasticity events which occur in Schaffer collateral-CA1 synapses are associated with alterations in the number of AMPA receptors expressed on the spine membrane through activation of exocytosis or endocytosis mechanisms, as well as changes in AMPA receptors conductance through

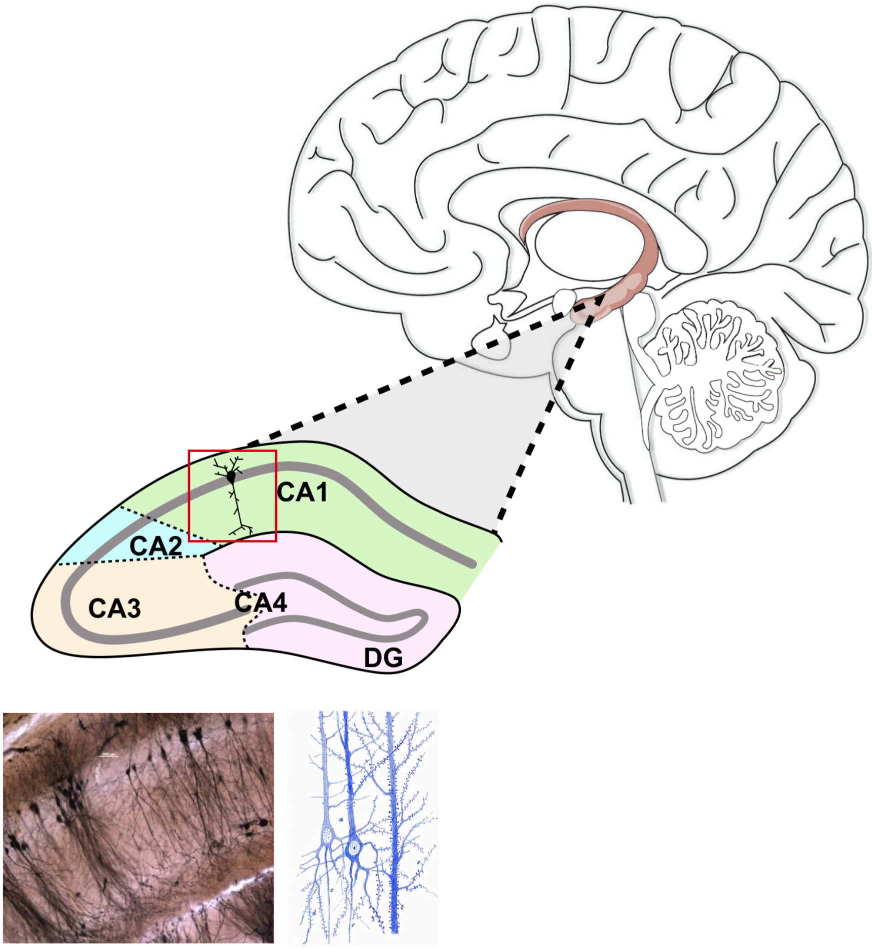

Fig. 4.1 Schematic image of Brain with a magnified illustration of hippocampal CA3-CA1 synapses (Adapted from *Stangor and Walinga, 2014 [14]*, and *Sheppard et al. 2019 [15]*). Bottom left, the image of Golgi-Cox stained hippocampal CA1 neurons from mouse (taken from *Sheppard et al. 2019 [15]*). Bottom right, drawing used by Cajal to show the existence of dendritic spines on pyramidal cells with the methylene blue method (taken from *DeFilipe, 2015 [16]*).

phosphorylation modifications [17,18]. Together, these molecular mechanisms lead to fine modulations in the strength of the synaptic transmission.

The reactions underlying such modulation are controlled by the transient variations in the Ca^{2+} concentration that occur in the post-synaptic spine, especially, due to the activation of NMDA receptors (*Fig. 4.2*). NMDA receptors are hetero-tetrameric glutamatergic ionotropic receptors permeable to Na^{2+}, K^{+}, Ca^{2+} and Mg^{2+} ions [19,20]. The permeability to Mg^{2+} ions gives to NMDA receptors a pronounced voltage-dependent behavior. At resting membrane potentials external Mg^{2+} ions enter into the receptor's pore, but unlike the other permeating ions, they bind tightly to the pore blocking it and impairing further ion permeation [21,22]. One of the most accepted physiological mechanisms needed to efficiently unblock NMDA receptors, thus generating an inward Ca^{2+} flux, is a temporal coincidence between the release of presynaptic neurotransmitter and a depolarization of the postsynaptic spine (of sufficient amplitude and duration) elicited by post-synaptic activity. This synchronicity is taken into account in the *Spike Timing Dependent Plasticity (STDP)* paradigm that also includes the postsynaptic dendritic activity expressed in the form of *back-propagating action potentials* (bAPs) [23,24]. The transient postsynaptic Ca^{2+} inward current generated by the activation and unblocking of NMDA receptors critically acts on the kinetic equilibrium of different

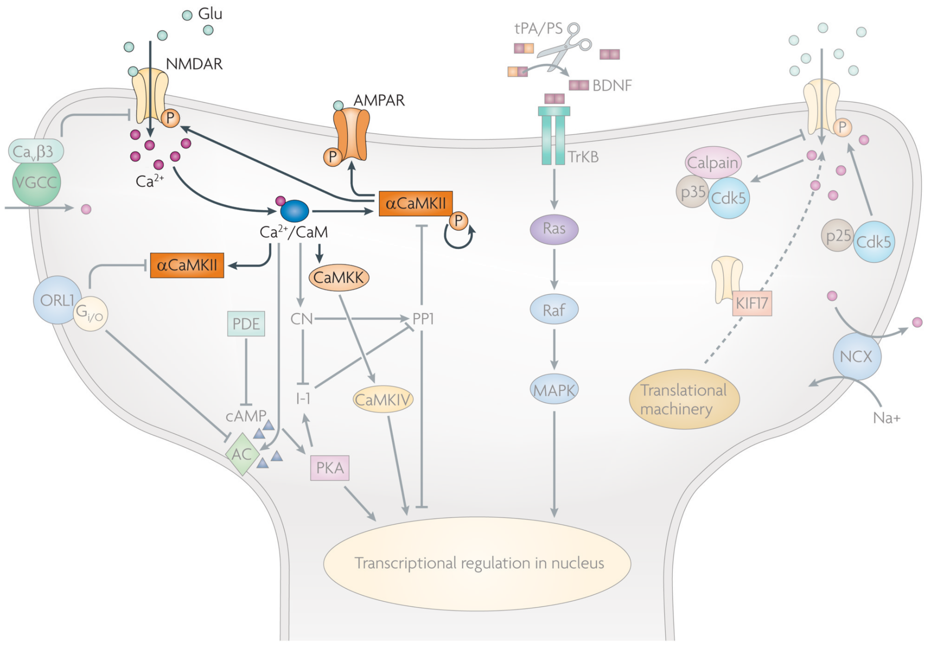

Fig. 4.2 NMDAR-dependent signaling and downstream kinases and phosphatases implicated in learning and memory enhancement. The part of the image that is not faded represents the signaling pathway implemented in our framework. Figure taken and adapted from *Lee and Silva, 2019* [25].

calcium-binding proteins involved in LTP/LTD-inducing pathways, such as Ca^{2+}/Calmodulin-dependent Kinase II (CaMKII) [25–27], (*Fig. 4.2*).

Dysfunctions on LTP/LTD-mediated synaptic plasticity have been associated with many neurological disorders like epilepsy and Alzheimer, Hughtington, and Parkinson's diseases [4,25–30].

A comprehensive and detailed understanding of the molecular mechanisms underlying synaptic transmission and neuroplasticity is then crucial for the physio-pathological characterization of many cognitive functions. However, even if LTP/LTD-mediated synaptic plasticity has been extensively studied, providing a substantial description of a full integration of the interaction networks underlying the whole synaptic transmission, deeply characterized at the molecular level, is currently a major challenge. This could be the starting point for the identification of new therapeutic strategies, aimed at re-tuning the global behavior of the intricate network of molecular interactions underlying synaptic plasticity, and thus, restoring its functional integrity.

Here, we present, and render available to the scientific community, a mathematical model of the CA3 Schaffer collateral-CA1 transmission. Although others integrated and detailed models of glutamatergic synapses have been proposed recently [31,32], a clinical-oriented application of such models, able to take into account also the molecular characterization of particular disease-associated variants often lacks. The rationale of our work was to provide a synaptic model which can be easily reproduced, run, and integrated into larger analytical pipelines, proposing a novel viewpoint on the possible applications of comprehensive and detailed system biology models.

Our model allows us to simulate several features of the CA3-CA1 synaptic transmission process. These include (1) glutamate release inside the synaptic cleft as a result of a presynaptic stimulation, (2) bAP in the postsynaptic dendritic spine, (3) kinetic description of the gating mechanism of both NMDA and AMPA receptors, (4) estimation of the excitatory post-synaptic currents (EPSCs) and excitatory post-synaptic potentials (EPSPs), including the explicit calculation of the NMDA-mediated inward Ca^{2+} current, and (5) kinetic descriptions of the Ca^{2+}-dependent molecular reactions which take place inside the post-synaptic spine, and lead to the activation of CaMKII. Here we report some of the qualitative features observed in the receptors-specific contributions to synaptic transmission, as well as in the timing of pre/post-synaptic stimulation.

4.2 Results and Discussions

This section is divided in two main subsections. In the first part, we present the implementation of the mechanistic model, providing an overview on the structure of the pipeline through the description of the individual modules, implemented to describe different fragments of the system. The second part contains the simulation of the model under different parameter configurations. This allows us to infer some qualitative features of the system, with a particular focus on the timing between pre and post-synaptic stimuli, and finally to assess shifts in the global system behavior given by the introduction of rare variants in the NMDA receptors associated with diseases.

4.2.1 An integrative, *Python*-based, pipeline for simulating glutamatergic synaptic transmission

We developed an integrative mathematical pipeline for easily running numerical simulations of synaptic transmission in individual CA3 Schaffer collateral-CA1 synapses, driven by both pre and post-synaptic stimulation. The pipeline is composed of 4 different main modules, each of them aimed to model a different part of the whole transmission process. Starting from the definition of a stimulation pattern, new modules were progressively implemented and added on top of each other, defining a linear pipeline for simulating the synaptic transmission following the scheme represented in *Fig. 4.3*.

4.2.1.1 Stimulation Pattern Design (SPD)

This module implements a series of functions which easily allow to define a stimulation pattern that will drive the synaptic transmission. Such stimulation

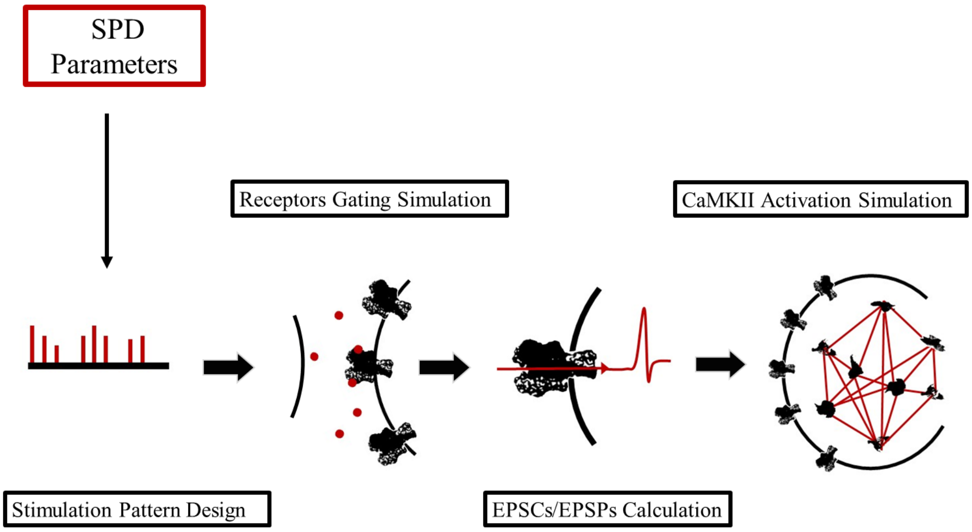

Fig. 4.3 Conceptual scheme of the pipeline to simulate our synaptic transmission

patterns can be composed by both pre and post-synaptic stimuli, organized as trains of bursts. Here, highly customizable patterns can be designed by setting the number of stimuli composing each burst, the intra-burst and inter-burst frequencies for both pre and post-synaptic stimuli (*Fig. 4.4*).

Pre-synaptic stimuli are idealized and modeled as instantaneous rise and fall of the free glutamate concentration in the synaptic cleft, assuming a square pulse-like shape. In this article, we will refer to a pre-synaptic stimulus as "glutamate pulse". The quantity of released glutamate (*i.e.,* the pulse amplitude, expressed in µM) and the glutamate exposure time inside the cleft (*i.e.,* the pulse width, expressed in ms) of each pre-synaptic stimulus can be independently parameterized. Post-synaptic stimuli are modeled as dendritic back-propagating action potentials, consisting in transient depolarization potentials of the post-synaptic spine membrane. The shape of such stimuli has been defined using a two-component exponential function (see *methods*, section 4*.3.1.1* for further details), as proposed by *Shouval et al.* [33]. The stimulation pattern defined in this module will constitute the input of the following modules.

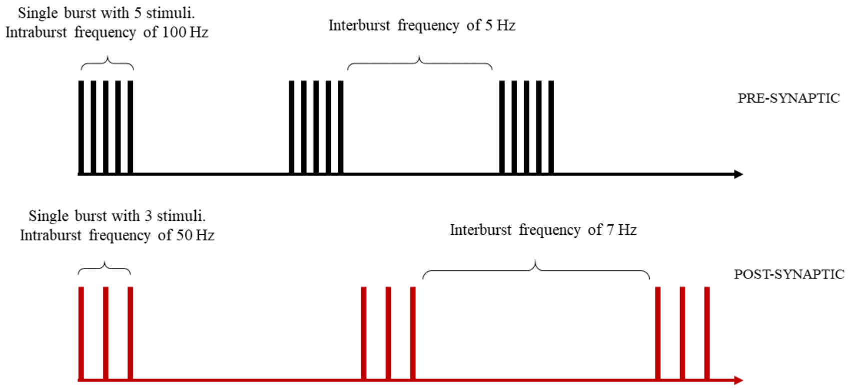

Fig. 4.4 Example scheme of a stimulation pattern. Pre and post-synaptic stimuli are organized as trains or bursts. Each burst is composed by a sequence of stimuli, delivered at an intra-burst frequency. Inter-burst frequency defines the interval between each burst. Number of stimuli per burst, intra-burst and inter-burst frequencies can be defined during the stimulation pattern design, for both pre and post-synaptic patterns.

4.2.1.2 Receptors Gating Simulation (RGS)

Pre-synaptic stimuli defined during the design of the stimulation pattern are used as input to a second module, which is aimed to simulate the interactions between the neurotransmitter and the AMPA and NMDA receptors. This module contains the compartmental kinetic description of both the receptor-neurotransmitter binding reactions and the gating mechanisms which lead to the opening of the channels. Particularly, the latter consists in state-transition models (including closed, pre-open, open, and desensitized states) which statistically represent the stochastic distribution of the current traces recorded by electrophysiological experiments. We selected and integrated one kinetic model for both, AMPA and NMDA receptors, proposed by *Koike* and collaborators and *Amico-Ruvio and Popescu* [34,35], respectively. Then, we translated both models into systems of first-order differential equations, implemented in a single larger kinetic model using the *PySB python* package (see *methods* for further details). Finally, a numerical integration is performed allowing the simulation of the receptor's behavior with a high temporal resolution (integration step of 1 μs). We tested the reliability of these *ex-novo* implementations by comparing the behaviors predicted by our model, for both AMPA and NMDA receptors, with the behaviors reported in the works by *Koike* and collaborators and by *Amico-Ruvio and Popescu* [34,35] (*Tab. 4.A1*). We observed a strong consistency between the kinetic features of both AMPA and NMDA receptors predicted by our PySB-based model and the respective original models, pointing out to a high reliability of our implementation.

4.2.1.3 EPSCs/EPSPs Calculation (CPC)

The third module of our framework consists of a system of equations used to explicitly calculate the EPSCs and the respective EPSPs generated during the simulation of the synaptic transmission. The EPSCs are estimated by calculating, over the simulation, the ion fluxes that permeate each open channel (predicted with the RGS module, described in section 4*.2.1.2*). This estimation is made according to the channel-specific conductance, the channel-specific reversal potential, and the depolarization level of the post-synaptic membrane.

The EPSPs are then derived from the EPSCs (see *methods* section 4*.3.1.3* for further details). All the depolarization potentials, which includes the EPSPs and, eventually, the bAPs arising from the post-synaptic stimulation, are summed together to assess the global changes in the membrane depolarization value. In this module the equation for the explicit estimation of the NMDA-mediated Ca^{2+} current, is used to assess the post-synaptic changes in the Ca^{2+} concentration according to a simple model proposed by *Shouval et al.* [33] (see *methods,* section 4*.3.1.3* for further details).

4.2.1.4 CaMKII Activation Simulation (CAS)

The last module of our pipeline aims to simulate a kinetic description of the post-synaptic molecular interactions that controls the CaMKII autophosphorylation events. For this purpose, as previously described for the RGS module (section 4*.2.1.2*), we selected from literature a detailed kinetic model based on its reproducibility, and we transcribed all its reactions into a second PySB model as a system of first-order differential equations. We chose to implement a model for the CaMKII activation proposed by *Pepke et al.* [36], and we integrated it into the simulation pipeline. This kinetic model includes a large number of reactions, mainly characterizing the interactions between free Ca^{2+} ions, calcium-binding messenger CaM and the CaMKII enzyme. Particularly, the Ca^{2}-CaM mediated autophosphorylation of CaMKII enzyme, which leads to its own activation, directly plays a pivotal role in inducing the early phase of synaptic plasticity [22–24]. Although the changes in the synaptic strength are currently not explicitly assessed in our model, the variations in the activated CaMKII accumulation allows one to assess the relative efficiency of the simulated synaptic transmission.

4.2.2 Kinetic behavior analysis of AMPA and NMDA receptors under different pre-synaptic stimulation conditions

We explored how AMPA and NMDA receptors kinetically behave under different stimulations patterns exploiting the RGS module (section 4*.2.1.2*). For this purpose, we simulated the model using different pre-synaptic stimulation patterns, consisting of either a single glutamate pulse or bursts of multiple glutamate pulses, delivered at different frequencies (ranging from 10 to 100 Hz). The amplitude of the glutamate pulses was set into a physiological range of 1-2 mM [37,38], while the time width was varied in a range between 1 ms and 1.5 s.

We firstly focused on the kinetic behavior of AMPA receptors under a single glutamate pulse of 1 mM, simulated with 1, 5 and 10 ms width. The desensitization kinetics of AMPA receptors predicted by the gating model shows a much slower time course (τ = ~25 ms, fitted with single exponential function) compared to the deactivation kinetics (τ = ~0.55 ms, fitted with single exponential function) after the end of a single glutamate pulse (*Fig. 4.5 A)*. Moreover, both the exposure time of the glutamate (defined by the pulse width) and the stimulation frequency seems to strongly affect the amount of desensitized receptors reached after a single pre-synaptic event [34], (*Fig. 4.5 B)*. The faster deactivation compared to the desensitization predicted by the model, points to the property of AMPA receptors to preferentially undergo a temporal accumulation of desensitized states instead of the open states.

We then analyzed how the variation of the glutamate pulses duration affects the summation of desensitized states under a single pre-synaptic burst stimulation. The latter was simulated by a single burst composed by 5 glutamate pulses of 1 mM amplitude and 1, 5 and 10 ms width, with an intra-burst frequency of 100 Hz. We observed a significant increase in the temporal summation of desensitized AMPA receptors as the glutamate exposure values rise (*Fig. 4.5 C*, *D*, and *E,* respectively).

Next, we analyzed the predicted kinetic behavior of NMDA receptors. By simulating a single glutamate pulse of 1 mM amplitude and 1 ms, 500 ms, and 1.5 s width, we observed a significatively slower deactivation and desensitization kinetics compared to AMPA receptors (*Fig. 4.6*). Fitting the curves with a single exponential function we found time constants of 163, 195 and 210 ms for the deactivation kinetics after 1 ms, 500 ms and 1.5 s of glutamate exposure, respectively, and a time constant of 1.95 s for the desensitization kinetics (*Fig. 4.6 A, B)*. From these results, we got a ratio between the desensitization and the deactivation time constant ($\tau_{\mathrm{desens}}/\tau_{\mathrm{deact}}$) of ~12 for NMDA receptors and ~45 for AMPA receptors. The lower value found for NMDA receptors leads to a more efficient temporal summation of its open states. In fact, when we simulated our model with a single pre-synaptic burst of 5 glutamate pulses of 1 mM amplitude and 1, 5, 10 ms width, with intra-burst frequencies of 10, 50 and 100 Hz, we observed, effectively, summation of the open NMDAs (*Fig. 4.6 C, D, E)*

To have a better insight on the difference between the kinetic behavior of AMPA and NMDA receptors, we simulated our model with a single pre-synaptic burst of 5 glutamate pulses of 1 mM amplitude and 1, 5 and 10 ms width, varying the intra-burst frequency between 10 and 100 Hz. For each intra-burst frequency, we calculated the ratio between the total number of desensitized

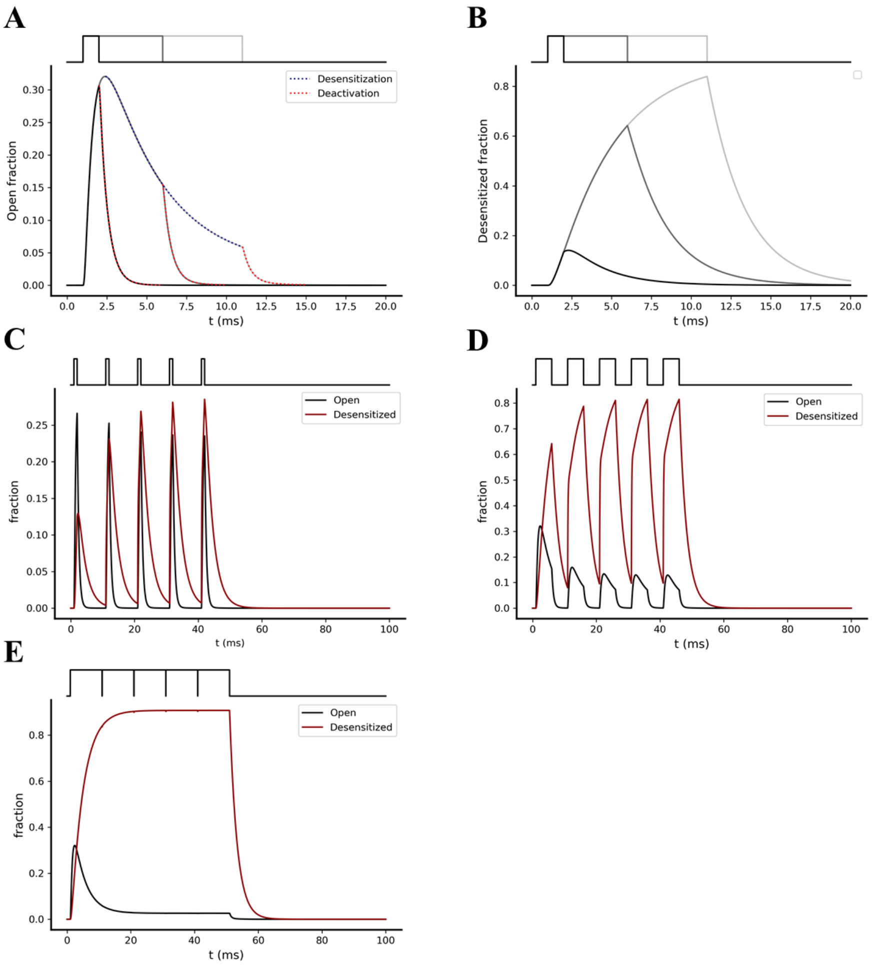

Fig. 4.5 Opening and desensitization kinetics of the AMPA receptors. **(A)** Open fraction kinetics following a stimulation with a single glutamate pulse of 1mM amplitude and width of 1 ms (black), 5ms (dark grey) and 10 ms (light grey). Blue dotted trace shows the desensitization kinetics, while red dotted traces show the deactivation kinetics following glutamate removal from the synaptic cleft. **(B)** Desensitized fraction kinetics following a stimulation with a single glutamate pulse of 1mM amplitude and width of 1 ms (black), 5ms (dark grey) and 10 ms (light grey). **(C, D, E)** Kinetics of open and desensitized fractions following pre-synaptic stimulations with a burst composed of 5 glutamate pulses, with glutamate pulse amplitude of 1 mM, an intra-burst frequency of 100 Hz, and a pulses width of 1 ms **(C)**, 5 ms **(D)** and 10 ms **(E)**.

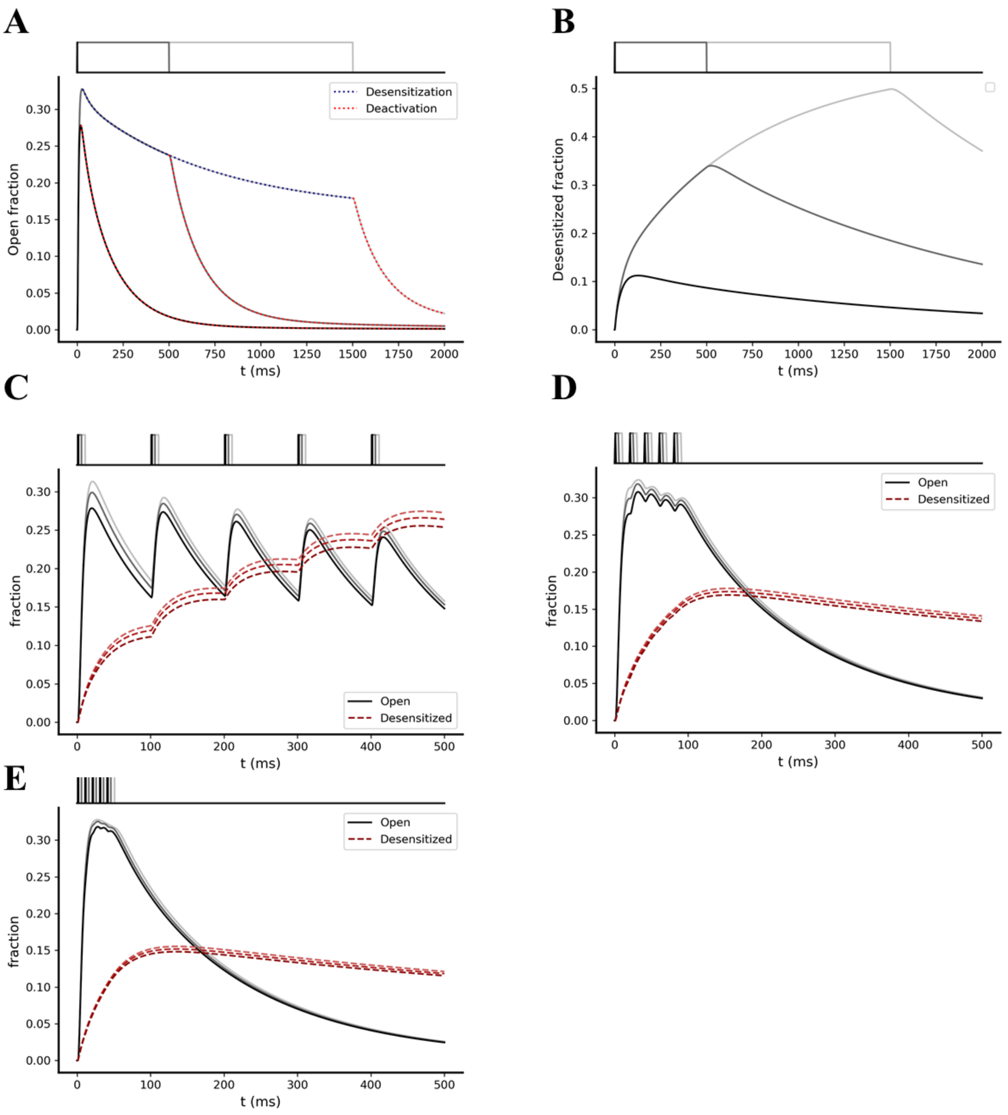

Fig. 4.6 Opening and desensitization kinetics of the NMDA receptors. **(A)** Open fraction kinetics following a stimulation with a single glutamate pulse of 1mM amplitude and width of 1 ms (black), 500 ms (dark grey) and 1.5 s (light grey). Blue dotted trace shows the desensitization kinetics, while red dotted traces show the deactivation kinetics following glutamate removal from the virtual synaptic cleft. **(B)** Desensitized fraction kinetics following a stimulation with a single glutamate pulse of 1mM amplitude and width of 1 ms (light grey), 5ms (dark grey) and 10 ms (black). **(C, D, E)** Kinetics of open and desensitized fractions following pre-synaptic stimulations with a burst composed of 5 glutamate pulses, with glutamate pulse amplitude of 1 mM, pulse width of 1 ms (black), 5 ms (dark grey), 10 ms (light grey) and an intra-burst frequency of 10 Hz **(C)**, 50 Hz **(D)** and 100 Hz **(E)**.

and open receptors. According to our model, these simulations pointed out that the desensitized/open ratio of AMPA receptors depends more on the stimulation frequencies and on the glutamate pulses durations compared to the desensitized/open ratio of the NMDA receptors (*Fig. 4.7*).

4.2.3 Temporal relationship between pre and post-synaptic stimuli strongly impacts synaptic transmission efficiency

During the stimulation of the synapse, the equations implemented in the CPC module (section 4*.2.1.3*) allow us to explicitly assess the individual contribution of both AMPA and NMDA receptors to the global electrical transmission.

Pre-synaptic-induced excitatory potentials and post-synaptic dendritic back-propagation events programed during the stimulation pattern design are integrated together to continuously estimate the variations in the NMDA permeability, as well as in the Ca^{2+} flux driving force (see *methods* section 4*.3.1.3* for further details). We explored through several simulations how the temporal relationship between pre and post-synaptic stimuli can shape the efficiency of the electro-chemical transmission.

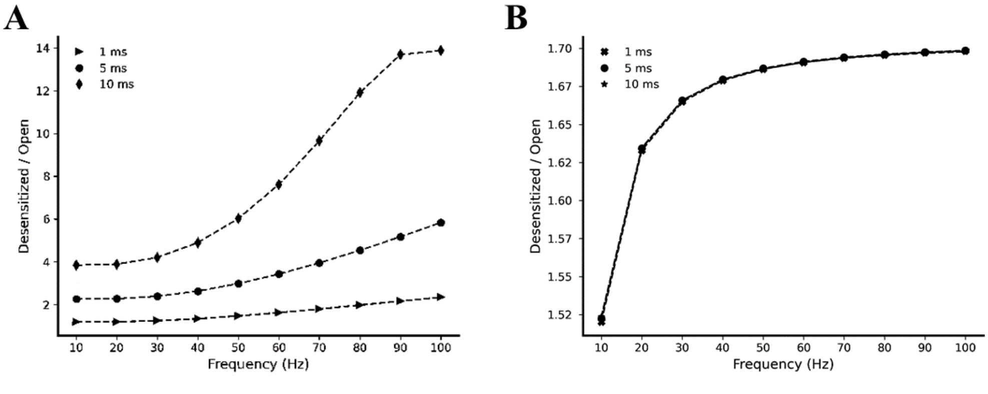

Fig. 4.7 Desensitized/Open ratio expressed as a function of stimulation frequency. Simulations were performed using a single pre-synaptic burst composed by 5 glutamate pulses of 1 mM amplitude and 1, 5, 10 ms width. For each simulation the ratio between the desensitized and the open fraction has been calculated for **(A)** AMPA and **(B)** NMDA receptors.

4.2.3.1 AMPA-mediated EPSPs are not sufficient to efficiently relieve the Mg^{2+} block from NMDA receptors

The pronounced voltage-dependent affinity of NMDA receptors for the extracellular Mg^{2+} ions causes the actual permeation of the channel to be strongly modulated by the depolarization level of the membrane [19]. We have previously observed that the kinetic equations implemented in the RGS module predict no effective temporal summations of open AMPA receptors because of their fast desensitization and deactivation kinetics, as also observed in other studies [34,39]. Analyzing the output of the RGS module using the equations implemented in the CPC module (sections *4.2.1.2* and *4.2.1.3*) we then observed that, coherently, also the AMPA-mediated responses tend not to summate (*Fig. 4.A1*).

This observation prompted us to investigate if the amplitude of an AMPA-mediated EPSP evoked by a single pre-synaptic event was high enough to relieve the Mg^{2+} block from NMDA receptors. Since the EPSPs amplitudes of AMPA and NMDA receptors are influenced by their levels of expression on the post-synaptic spine surface, we performed multiple simulations of a single glutamate pulse of 1 mM amplitude, 1, 5 and 10 ms width, varying the level of available AMPA receptors in a range between 20 and 200 [40]. Simulation results reported that the maximum AMPA-mediated EPSPs peaks elicited by single-pulse pre-synaptic stimulations reach -40 mV with 200 units of AMPA receptors (*Fig. 4.8 A)*. According to the Mg^{2+} unblocking probability function that we have incorporated into the model (see *methods* section *4.3.1.3* for further details), such depolarization level can effectively release the Mg^{2+} ion from NMDA receptors only if the extracellular Mg^{2+} concentration is very low compared to the physiological concentration (*Fig. 4.8 B*), which is near to 1 mM [19].

These results emphasize the fact that only pre-synaptic events may be not enough to ensure an effective Ca^{2+} permeation. As supported by the STDP paradigm, temporal coordination between pre and post-synaptic events must

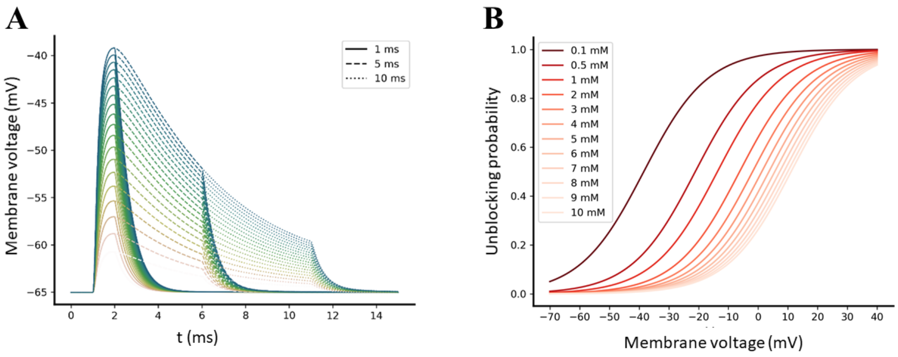

Fig. 4.8 **(A)** Simulated AMPA-mediated EPSPs evoked by different numbers of available AMPA receptors, ranging from 20 (lower trace) to 200 (upper trace). Solid, dashed and dotted traces refer to single pulse stimulation performed with a glutamate pulse width of, respectively, 1, 5 and 10 ms. **(B)** Sigmoidal unblocking probability function for Mg^{2+} block, expressed as function of membrane voltage. Each trace corresponds to a different value of extracellular Mg^{2+} concentration.

occur in order to allow a significant Ca^{2+} influx which can effectively trigger plasticity [41].

4.2.3.2 Synchronization between pre and post-synaptic stimulation significantly increases the NMDA receptor contribution to synaptic transmission.

We further investigated how the synchrony between pre and post-synaptic activity can affect the efficiency of synaptic transmission, particularly by increasing the amplitude of the NMDA receptors-mediated EPSCs and EPSPs.

For this purpose, we compared the individual responses of AMPA and NMDA receptors obtained from two different stimulation patterns, one including only pre-synaptic stimulation and one including coupled pre and post-synaptic stimulations. In both stimulation patterns the pre-synaptic stimulation consisted in a single theta burst composed of 5 glutamate pulses of 1mM amplitude and 1, 5 and 10 ms width, with an intra-burst frequency of 100 Hz [42]; post-synaptic stimulation was designed as a single dendritic back-propagation event, which occurs in the post-synaptic spine 1 ms after the first pre-synaptic stimuli was delivered. Simulations were performed in the presence of 20 AMPA and 15 NMDA receptors [40,43], with extracellular Mg^{2+} concentration set to 1 mM. As expected, significant increases in the total NMDA receptor-mediated current peak (~2.5 fold) as well as in the Ca^{2+} that permeated the channel (~4.5 fold) were observed during the coupled pre and post-synaptic stimulation compared to the pre-synaptic stimulation alone, showing the impact of bAP-mediated synaptic facilitation on the NMDA receptors conductance (*Fig. 4.9*).

Since we had observed that the presence of a bAP during stimulation significantly increases the NMDA receptor mediated EPSC, we analyzed how variations in temporal coordination level between pre and postsynaptic stimuli impacts the amplitude of the elicited Ca^{2+} influx. For this purpose, we performed multiple simulations varying the time interval between pre and post-synaptic stimuli ($\Delta t = t_{post}-t_{pre}$). For each simulation we then evaluated the effect of the bAP-induced synaptic facilitation by calculating the maximum Ca^{2+} concentration reached in the post-synaptic spine. Simulating a single pre-synaptic glutamate pulse of 1 mM amplitude and 1 ms width, together with a single post-synaptic bAP, we found that post-synaptic Ca^{2+} rises from a value of ~200 nM (the post-synaptic Ca^{2+} concentration elicited by a single pre-synaptic event alone) to a maximum of ~1.4 μM (*Fig. 4.10*). This value is obtained when the pre-synaptic event precedes the post-synaptic event (positive Δt) of ~20 ms, in agreement with the Hebbian STDP paradigm for synaptic plasticity (see *Feldman 2012* [20] for a review).

4.2.4 Kinetic and pharmacological analysis of NMDA variants: Multiscale integration

Deactivation time course defines the time required by the receptor-mediated current to decay after the removal of the agonist from the synaptic cleft. This kinetic feature, together with EC_{50} value of the agonist, constitute a prominent quantitative feature used to perform functional analysis of ion channels [44]. Many published studies on rare NMDA receptor variants tried to assess

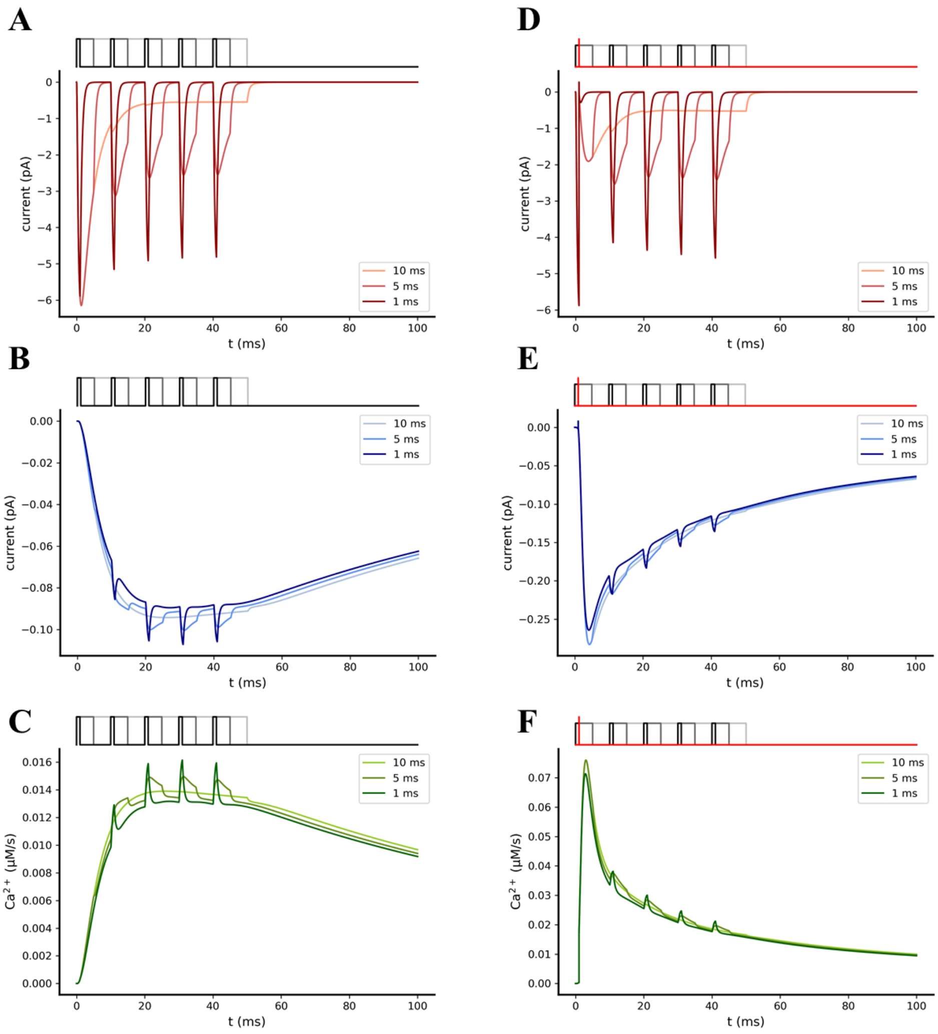

Fig. 4.9 Simulation of synaptic transmission elicited by a single pre-synaptic burst of 5 glutamate pulses, in absence **(A, B, C)** or in presence **(D, E, F)** of a single post-synaptic back-propagating action potential (bAP). **(A, D)** Time course of the individual AMPA-mediated EPSC. **(B, E)** Time course of the individual NMDA-mediated EPSC. **(C, F)** Time curse of the Ca^{2+} molar flowrate that permeate NMDA receptors during the simulations. Pre-synaptic bursts were composed of 5 glutamate pulses of 1 mM amplitude and 1 ms (black pulses), 5 ms (dark grey pulses) and 10 ms (light grey pulses) width; in each plot the responses elicited by 1 to 10 ms widths are represented by different colors, respectively, from the darkest to the brightest. Post-synaptic activity (red trace) was programmed as a single dendritic back-propagation event which occurs 1 ms after the first pulse of the pre-synaptic burst began. Both simulations were performed in the presence of 20 AMPA, 15 NMDA and 1 mM of extracellular Mg^{2+}.

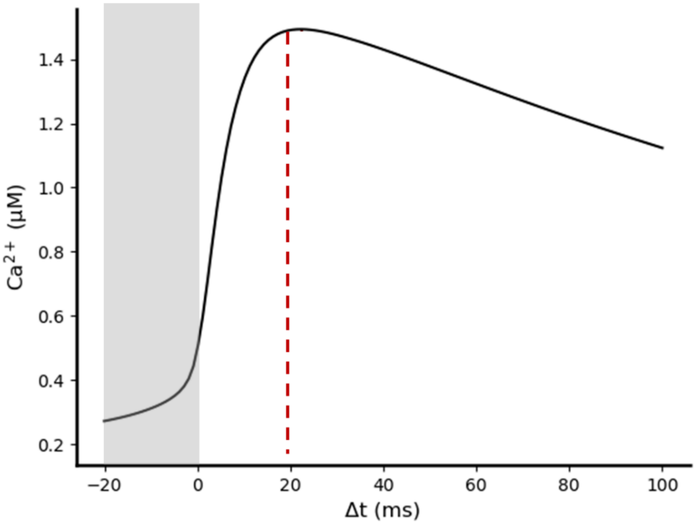

Fig. 4.10 Relationship between pre/post-synaptic stimulation timing and Ca^{2+} concentration peaks reached in the post-synaptic spine. Simulations were performed in the presence of 20 AMPA, 15 NMDA and 1 mM of extracellular Mg^{2+}. Maximum post-synaptic Ca^{2+} concentration was reached with $\Delta t \approx 20$ ms. Gray rectangle highlights negative Δt values in which post-synaptic stimuli precede pre-synaptic stimuli.

the severity of a certain mutation considering its impact on both glutamate potency and deactivation time constant [25,45–47].

On that account, we used our model to predict how mutations on the binding site affects the k_{off} rate of the glutamate binding reaction and, consequently, the glutamate affinity to the receptor. For this study we have selected variants with a negative impact on the glutamate affinity (K_d) and for which data of EC_{50}, calculated through peak current measurements, and data of activation kinetics have been reported in different experimental and computational studies [25,45,46,48]. In particular, we focused on two rare variants: Glu413Gly and Cys461Phe that fall inside the Glun2B binding pocket (*Fig. 4.11*). These variants have been shown to decrease the glutamate potency, which may result from a decrease in the glutamate affinity [46,48,49].

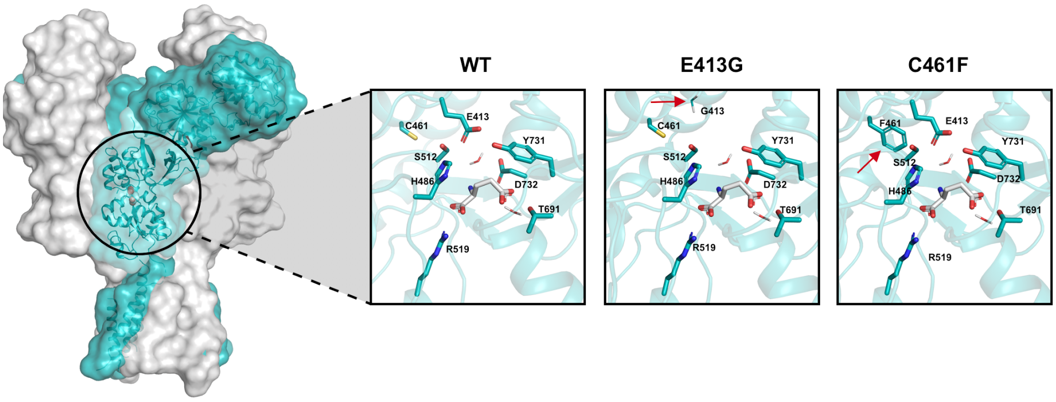

Fig. 4.11 Structure of human GluN1/GluN2A NMDA receptor (PDB accession code: 4TLM). GluN2B subunit is colored in light blue. The insights show the glutamate binding domain of the wild-type (WT) receptor and the two structural variants Glu413Gly and Cys461Phe. Each window focuses on the docked glutamate (white molecule) and the crucial residues that directly participate to the interaction. Red arrows point to the residue substitution of each of the two structural variants.

Therefore, we tuned the NMDA kinetic model to reproduce the same concentration-response behaviors experimentally observed for both the Glu413Gly and Cys461Phe variants.

Exploiting our kinetic model, we were able to computationally assess the NMDA-glutamate concentration-response relationship by using the following approach: firstly, we sampled concentration values in a range between 0.01 and 1000 mM; next, for each value we run the RGS module, simulating a single glutamate pulse, with amplitude corresponding to the current glutamate concentration value and width of 1.5 s, as reported by experiments [45], setting the number of AMPA receptors to 0 (since we were interested in isolate the NMDA response). Finally, calculating from each simulation the peak of evoked current, EC_{50} value was obtained by fitting the concentration-response data with logistic function.

To predict the shifts in the NMDA receptor-glutamate affinity associated to the rare variants Glu413Gly and Cys461Phe, knowing their experimental EC_{50} values (75-79 μM for Glu413Gly [45,46] and 169 μM for Cys461Phe [45]), we progressively increase, during a sequence of multiple simulations, the ratio between the rate constants k_{off} and k_{on} (*i.e.,* the K_d) of the equations describing the interaction between NMDA receptor and glutamate. For each simulation we computed the EC_{50} value, and in the end of all simulations we selected the K_d that rendered the EC_{50} values closest to experimental ones.

As a result, we found that the NMDA receptor kinetic behavior generated by predicted K_d values shows a current deactivation time constant very close to the experimental ones (*Tab. 4.1*).

The kinetic model of the NMDA receptor was tuned by only increasing the k_{off} rate constant of the glutamate binding reactions. Therefore, we reasoned that the coherence between our results and the experimental data points to the fact that the analyzed variants are likely to affect the affinity of the receptor (thus causing an EC_{50} shifting) by negatively altering the glutamate residence time inside the binding pocket of the receptor.

Tab. 4.1 Predicted K_d and deactivation time constant for NMDA WT and variants. Deactivation decay was fitted with a two-components exponential function, and the weighted Tau was then calculated (see methods section 4.3.2.2).

	Predicted K_d (μM)	**Weighted Tau (ms)**	
		Predicted	**Exp.**
Wt	2.5	328	314-570 [45,46,50]
Glu413Gly	190.5	29	20-34 [45,46]
Cys461Phe	446.5	27	28 [46]

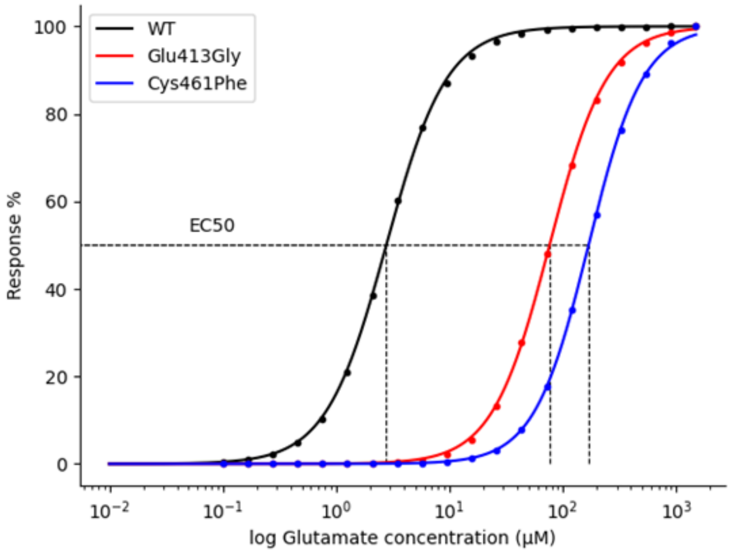

Fig. 4.12 Dose-response curves of the effect of glutamate on wild-type (WT) and variants-NMDA receptors. Simulation data was fitted with logistic regression. EC_{50} values of 2.7, 76 and 169 μM for WT, Glu413Gly and Cys461Phe-NMDA receptors, respectively.

For NMDA wild-type receptor we found a K_d value of 2.5 μM and a deactivation constant of 328 ms, whereas for the Glu413Gly and Cys461Phe variants we found K_d values of 190.5 and 446.5 μM and deactivation constants of 29 and 27 ms, respectively (*Fig. 4.12* and *Tab. 4.1)*. As these results imply, the Glu413Gly and Cys461Phe variants increase the K_d of glutamate of ~75 and ~180-fold (*Tab. 4.1*).

The next step in our multiscale analysis of NMDA Glu413Gly and Cys461Phe receptor variants consisted in further investigating if the calculated affinity alterations can impact the synaptic plasticity mechanism. To address this question, we simulated the effects of the structural variants on the amplitude of the raise in the post-synaptic Ca^{2+} concentration and on the amount of activated CaMKII, an enzyme which directly plays a pivotal role in triggering synaptic plasticity events in CA3-CA1 synapses. This latter estimation was

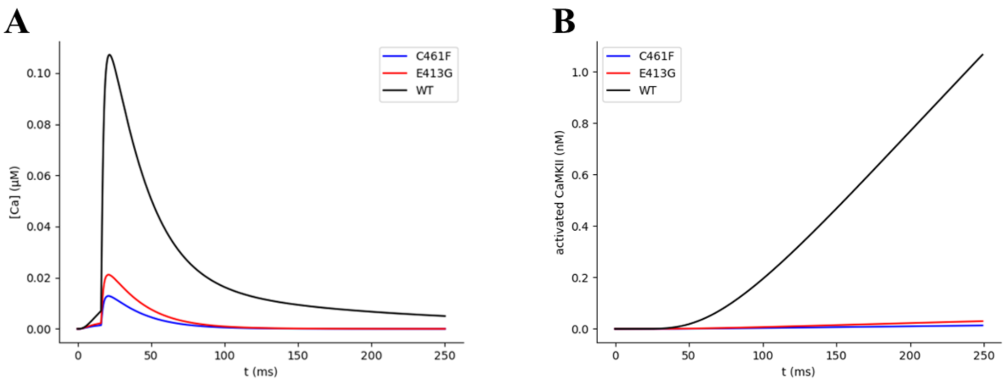

Fig. 4.13 Variation of **(A)** Ca2+ concentration and **(B)** activated CaMKII over time for the WT and variants NMDA receptors. All simulations were performed under one pair of single pre and postsynaptic pulses, with a presynaptic pulse of 1 ms of glutamate exposure, a delay between the pre and the postsynaptic stimuli of 20 ms, and 1 mM of Mg^{2+}.

done by exploiting the CAS module (section 4.*2.1.4*). This module contains a mathematical description of the Ca^{2+}-dependent CaM-CaMKII transduction pathway, which, starting from Ca^{2+} transients, leads to activation of CaMKII kinase (see *methods* section *4.3.1.4* for further details). We stimulated our virtual synapse with a pair of single pre and post-synaptic stimuli (glutamate pulse of 1 mM amplitude and 1ms width, time interval between pre and post-synaptic stimuli of 20 ms). As expected, we found that the predicted decrease in the NMDA glutamate affinity significatively attenuates the amplitude of the elicited post-synaptic Ca^{2+} variation of ~5 and ~8.5 fold for the Glu413Gly and Cys461Phe variants, respectively (*Fig. 4.13 A*). Moreover, the kinetic model for the Ca^{2+}-mediated activation of the CaMKII enzyme predicted much lower amounts of activated CaMKII for Glu413Gly (~13 fold) and Cys461Phe (~23 fold) variants compared to the wild type (*Fig. 4.13 B*). Considering the key role that CaMKII enzyme plays in the molecular mechanism underlying synaptic plasticity process, the predicted drastic decrease in the activation efficiency of such enzyme points out the severity of these rare structural variants. In fact, since CaMKII-driven neuroplasticity seems to be negatively affected in a significant way, severe neuropathological phenotypes, including learning and memory impairment, are likely to arise.

In the last part of our *in silico* experiment we were interested in reporting a more general representation of the relationship between NMDA-glutamate affinity and CaMKII enzyme activation efficiency. Here, our rationale was to search for an NMDA-glutamate affinity threshold that can be used for discriminating between high and low-severity variants, knowing their respective K_d. We proceeded, for this purpose, to simulate the whole synaptic model with the same basic stimulation pattern previously adopted for the analysis of Glu413Gly and Cys461Phe variants but varying the K_d affinity value in a range between 1 and 1000 μM. For each simulation (*i.e.*, for each K_d value) we selected the maximum amount of activated CaMKII observed. Data were firstly normalized to the maximum response observed across all the simulation and then fitted with the four-parameters logistic function (see *methods* section 4*.3.2.3* for further details) (*Fig. 4.14*). Finally, the threshold has been calculated by finding the bending point of the fitted curve, which corresponded to a K_d value of ~19 μM (*Fig. 4.14*).

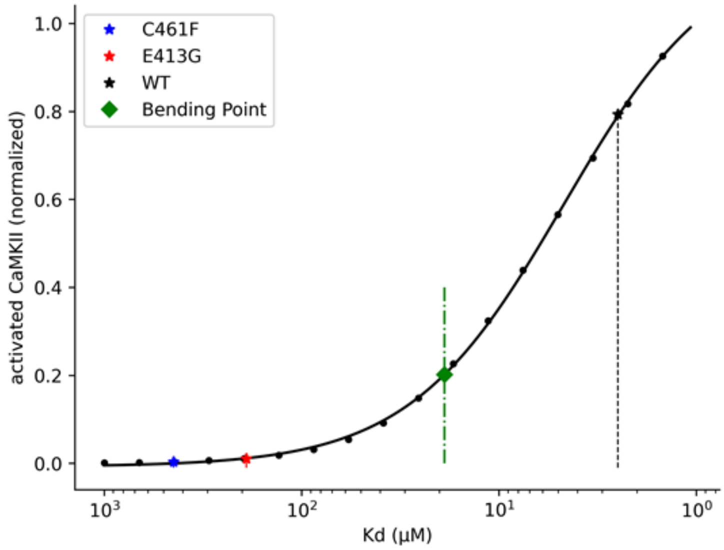

Fig. 4.14 Variation of activated CaMKII as function of the NMDA-glutamate K_d values. All simulations were performed under one pair of single pre and postsynaptic pulses, with a presynaptic pulse of 1 ms of glutamate exposure, a delay between the pre and the postsynaptic stimuli of 20 ms, and 1 mM of Mg^{2+}.

The identification of this type of thresholds can be very useful for a rapid assessment of the downstream effects of variants and can be easily integrated in larger analytical pipelines. We are currently working on a further implementation of this synaptic model which also integrates a detailed kinetic description of the reactions controlling the phosphorylation of AMPA receptors by the CaMKII enzyme, an event which is known to directly control synaptic strength modulations (LTP and LTD) by altering the conductance and trafficking of these receptors. With this further extension, we aim to explicitly quantify synaptic plasticity events that can occur during the stimulations.

4.3. Methods

In this section we provide a full and detailed description of all the individual modules that compose the proposed mathematical model, each of which implements a different fragment of the whole synaptic transmission process.

This modular rationale at the base of the framework implementation guarantees an easy customization of the simulation pipeline, as well as the further extensibility of the system.

The current build of the framework includes:

- Stimulation Pattern Design (SPD) module, where both pre and post-synaptic stimuli can be programmed independently. This module allows to define the inputs of the virtual synapse.
- Receptors Gating Simulation (RGS) module. This module performs a compartmentalized kinetic simulation of the virtual synaptic cleft, where neurotransmitter released from pre-synaptic stimuli interacts with ionotropic membrane receptors expressed on the post-synaptic spine.
- EPSCs/EPSPs Calculation (CPC) module. This module analyzes the data coming from the RGS module and, calculating synaptic currents and their respective potentials, integrates pre and post-synaptic stimuli. It constitutes a “bridge” between the extracellular and the intracellular compartments.

- CaM/CaMKII Activation Simulation (CAS) module. This module performs a compartmentalized kinetic simulation of a set of molecular reactions which takes place in the virtual post-synaptic spine, which includes the interactions between Ca^{2+}, Calmodulin (CaM) and Ca^{2+}/CaM-dependent Kinase II (CaMKII).

The kinetic equations used to describe the reactions contained in both RGS and CCS modules are implemented, exploiting the *PySB python* package [51], as systems of first-order differential equations. Numerical integration is performed using the *SciPy* ODE integrator [52]. All of the data analysis and fittings were performed using *SciPy* and *Numpy* packages [52,53]. Finally, all the plots were generated using the *Matplotlib* library [54].

All the code is stored in a publicly available *github* repository (*https://github.com/rribeiro-sci/CA3-CA1_SynapticModel*), where a *jupyter* notebook file for running simulations and performing basic analysis can be also found.

4.3.1 Mathematical model implementation

4.3.1.1 SPD module

In this module the stimulation pattern of the virtual synapse can be designed. Bidirectionality is a crucial feature of neuronal communication. The functional and topological properties of the brain neural network can be significantly shaped by the temporal relationship between forward and backward signals, as the STDP paradigm for the synaptic plasticity claims [20,21,55]. Therefore, integration of pre and post-synaptic stimuli constitute a logic core of our implementation. For this purpose, patterns of pre and post-synaptic stimuli can be programmed and simulated independently, in order to analyze how the system behaves under different levels of synchronization between pre and postsynaptic activities. Each pattern is modeled as a train of bursts. Numbers of stimuli per burst, intra-burst and inter-bursts frequencies can be specified to design custom stimulation patterns (*Fig. 4.4*).

In our model, pre-synaptic stimuli have been idealized as glutamate pulses, representing the instantaneous rise and fall in the free neurotransmitter concentration available inside the cleft compartment following pre-synaptic action potentials. Amplitude (*i.e.*, the amount of available free glutamate) and width (*i.e.*, the exposure time of the free glutamate) of the pre-synaptic glutamate pulses can be defined during the stimulation design.

On the other side, post-synaptic stimuli have been modeled as transient depolarizations of the post-synaptic spine generated by dendritic back-propagating action potentials (bAP). Each bAP is shaped using a two-component exponential function, taken from the work by *Shouval* and coworkers [33]:

$$(eq.\ 4.1) \qquad bAP(t) = V_{max} * \left(\left(I_{fast} * exp\left(\frac{-t}{\tau_{fast}}\right) \right) + \left(I_{slow} * exp\left(\frac{-t}{\tau_{fast}}\right) \right) \right)$$

where V_{max} is the maximum depolarization value for bAP value set to +67 mV [56], I_{fast} and I_{slow} are the relative magnitudes of the fast and slow components of the bAP that sum to one, and τ_{fast} and τ_{slow} are the relative time constants that describe the exponential decays of the two components.

4.3.1.2 RGS module

This module contains a system of kinetic equations describing the interactions between glutamate and AMPA/NMDA receptors, which take place inside the cleft compartment. The aim of this module is to accurately simulate both the receptors-neurotransmitter binding reactions and the gating mechanism that leads to opening or desensitization of the receptors.

Individual models describing the kinetic behavior of both AMPA and NMDA receptors have been selected from literature based on their reproducibility, and subsequently implemented as systems of first-order differential equations inside the PySB framework. To reproduce the kinetic behavior of AMPA receptors we chose a model proposed by *Koike et al.* [34] for homomeric GluR2 (flip) receptors. The model assumes two glutamate binding steps, one pre-open transient state, three desensitized states, and one open state of the receptor (*Fig. 4.A2 B*). For the kinetic description of the gating mechanism of NMDA receptors we used the model for GluN1/GluN2B NMDA receptor proposed by *Amico-Ruvio and Pospescu* [35]. This kinetic scheme includes two sequential glutamate binding steps, three pre-open transient states, two desensitization states and one open state of the receptor (*Fig. 4.A2 A).* Since we assume a saturating concentration of glycine inside the clef compartment, the binding steps with this molecule are not included in the kinetic model. Thus, all the resting NMDA receptors are considered glycine bound.

4.3.1.3 CPC module

In this module we implemented a set of equations that aims to assess the EPSCs and the respective EPSPs generated by the open fractions of both AMPA and NMDA receptors. EPSPs are then integrated with the back-propagating action potentials programmed during the stimulation design. Finally, the sum of all the depolarizing contributions is used to assess the variations of the postsynaptic membrane potential.

Many synaptic models that have been proposed in the past estimated the EPSCs and/or the EPSPs simply by using two-components exponential functions fitted on electrophysiological recordings [33,56–58]. On the contrary, in our model the open probabilities of the receptors vary according to a system of deterministic rate equations, that represent mass-action kinetics of receptors-neurotransmitter interactions [51]. For this reason, the rising and decay phases of both receptors-mediated EPSCs and EPSPs responses are shaped by the complex receptors-specific interaction kinetics with the neurotransmitter. This confers more flexibility to our model, allowing us, for example, to explore the responses generated by mutant forms of the receptors by tuning the rate constants of some of the kinetic equations.

We defined the EPSCs of AMPA and NMDA receptors as follows:

$$(eq.\ 4.2) \qquad EPSC_{AMPA}(t) = O_{AMPA}(t) * G_{AMPA} * \left(V_m(t-\Delta t) - V_{E_{AMPA}}\right)$$

$$(eq.\ 4.3)\qquad EPSC_{NMDA}(t) = O_{NMDA}(t) * G_{NMDA} * \left(V_m(t-\Delta t) - V_{E_{NMDA}}\right) * B\left(V_m(t-\Delta t)\right)$$

where $O_{AMPA}(t)$ and $O_{NMDA}(t)$ are the number of open NMDA and AMPA receptors at each time step; G_{NMDA} and G_{AMPA} are the single channel conductance set to 40 pS and 15 pS, respectively [59–61]; $V_m(t - \Delta t)$ is the membrane potential at time $(t - \Delta t)$; V_E is the channel-specific equilibrium reversal potential and defines the value of the membrane potential for which the electrochemical equilibrium is reached, and thus, the net flux through the channel is 0 (we assume that $V_{E_{AMPA}} = V_{E_{NMDA}} = 0$ [62]; $B(V_m)$ describes the voltage dependence of the NMDA current given by the Mg^{2+} blocks defined by [33]:

$$(eq.\ 4.4)\qquad B(V_m) = \frac{1}{1 - exp(-K_M V_m) * \left(\frac{[Mg^{2+}]}{3.27}\right)}$$

Once the EPSCs have been calculated, the relative EPSPs are determined simply by applying the law of Ohm:

$$(eq.\ 4.5)\qquad EPSP_{AMPA}\,(t) = EPSC_{AMPA}(t) * R_s$$

$$(eq.\ 4.6)\qquad EPSP_{NMDA}\,(t) = EPSC_{NMDA}(t) * R_s$$

where R_s is the spine's resistance set to 500 MΩ [63].

Finally, the total membrane potential, defined as the sum of the partial depolarization contributions, is calculated according to the equation:

$$(eq.\ 4.7)\qquad V_m(t) = V_r + EPSP_{AMPA}(t) + EPSP_{NMDA}(t) + bAP(t)$$

where V_r is the resting membrane potential of the spine (-65 mV).

In CA3 Schaffer collateral-CA1 synapses, the key mediator of the postsynaptic response is the elicited intracellular Ca^{2+} variation. Since NMDA receptors are the major source of Ca^{2+} during spine stimulation [64], we explicitly calculate the NMDA receptor-mediated Ca^{2+} molar flow rate as follows:

$$(eq.\ 4.8) \qquad I_{Ca^{2+}}(t) = O_{NMDA}(t) * G_{Ca^{2+}} * \left(V_M(t-\Delta t) - V_{E_{Ca^{2+}}}\right) * B\left(V_m(t-\Delta t)\right)$$

where $G_{Ca^{2+}}$ expresses the permeability of the NMDA receptor to Ca^{2+} ions, set to 2 $nM \cdot ms^{-1} \cdot mV^{-1}$ [56] and $V_{E_{Ca^{2+}}}$ is the reversal equilibrium potential for Ca^{2+} set to +130 mV [56].

Finally, the calcium dynamics in the postsynaptic cell is integrated by a simple first-order differential equation [33,56]:

$$(eq.\ 4.9) \qquad \frac{d[Ca^{2+}(t)]}{dt} = I_{Ca^{2+}}(t) - \frac{[Ca^{2+}(t)]}{\tau_{Ca^{2+}}}$$

where τ_{Ca2+} is the passive decay time constant of postsynaptic Ca^{2+} concentration, set to 20 ms [33].

A full list of all the parameters used in the equations described above is provided in *Tab. 4.A2*.

4.3.1.4 CAS module

The last module of the pipeline contains a compartmentalized kinetic description of a reaction network which takes place inside the post-synaptic spine.

Here, our rationale was to assess the variability in the amount of activated CaMKII enzyme upon different stimulation conditions. Since CaMKII plays a crucial role in the positive regulation of the early phase of LTP in CA3 Schaffer collateral-CA1 synapses [22–24], this estimation allows us to qualitatively infer the strength and the efficiency of the synaptic transmission. As previously described for the RGS module, we selected from literature a kinetic model based on its reproducibility, we translated it inside the PySB framework, and we, finally, appended the new block to the pipeline. For this purpose, we selected from BioModels database [65] a model describing a set of interactions that, starting from post-synaptic rise in Ca^{2+} concentration, leads to the autophosphorylation (*i.e.*, the activation) of monomeric CaMKII [36]. Particularly, the set of reactions implemented includes:

- Binding reactions between Ca^{2+} ions and CaM and CaM-CaMKII species;
- Dimerization reactions between Ca^{2+}-CaM and monomeric CaMKII;
- Dimerization reactions between two Ca^{2+}-CaM-CaMKII complexes;
- Autophosphorylation reactions of CaMKII monomers inside the 2(Ca^{2+}-CaM-CaMKII) complexes.

4.3.2 Data fitting

4.3.2.1 Concentration-Response curves

We computed the glutamate concentration-response curves for NMDA receptors by stimulating the system with 1 glutamate pulse of 1.5 s and in the absence of Mg^{2+} [45]. We run multiple simulations varying the amplitude of the glutamate pulse, with a concentration range between 0.01 and 1500 μM, and calculating the NMDA receptor-mediated current peaks values. The EC_{50} values were then calculated by fitting the concentration-response data with the following equation:

$$(eq.\ 4.10) \qquad Response\ \% = \frac{100}{\left(1 + \frac{EC_{50}}{[glutamate]}\right)^{n}}$$

where n is the Hill slope.

4.3.2.2 Two-component exponential function fitting

The deactivation time constant for NMDA wild-type receptor and Glu413Gly and Cys461Phe variants were estimated as weighted time constant of the double exponential fit of the NMDA receptor current decay after the exposure of 1 mM glutamate for 1.5 s. The two-component exponential function used for the fitting takes the form:

$$(eq.\ 4.11) \qquad I(t) = I_{fast} * exp\left(\frac{-t}{\tau_{slow}}\right) + I_{slow} * exp\left(\frac{-t}{\tau_{slow}}\right)$$

where I is the current, I_{fast} and I_{slow} are the amplitudes of the fast and slow components, respectively, and τ_{fast} and τ_{slow} are the respective decay time constants. The weighted time constant of decay (τ_w) was calculated using the following equation:

$$(eq.\ 4.12) \qquad \tau_w = \frac{I_{fast}}{I_{fast} + I_{slow}} * \tau_{fast} + \frac{I_{slow}}{I_{slow} + I_{fast}} * \tau_{slow}$$

4.3.2.3 Four-parameter logistic function and bending points

The data generated by the simulation of the relationship between different glutamate-NMDA K_d values and the concentration peaks of activated CaMKII enzyme (see *results* section *4.2.4*) were fitted with the four-parameter logistic function:

$$(eq.\ 4.13) \qquad Y = \frac{a - d}{1 + \left(\frac{X}{c}\right)^b} + d$$

where Y represents the activated CaMKII response, X represents the affinity value K_d (expressed in μM), a is the lower asymptote, d is the upper asymptote, c represents the K_d that generates a mid-way response between the estimated

a and d, and b is a slope factor. The bending point of the curve was then computed as follow:

$$(eq.\ 4.14) \qquad X_{bend} = \frac{a-d}{1+k} + d$$

$$(eq.\ 4.15) \qquad Y_{bend} = c * \left(\frac{a - Y_{bend}}{Y_{bend} - d}\right)^{\frac{1}{b}}$$

where k is a constant value, set to 4.6805 [66].

4.4 Conclusions

We proposed a compartmental model for the hippocampal synapse CA3-CA1. Our goal was to provide a simple and portable[*], *python*-based, program to run kinetics simulations of the synaptic transmission, which embodied both pre and post-synaptic activity. The rationale that drove us through the implementation, as well as the application, of this model was to focus on the integration between system biology and structural biology viewpoints. Exploiting this hybrid multiscale approach, we analyzed the impact of single disease associated variants of NMDA receptors, related to neurological disorders and cognitive impairments, may have on the whole synaptic transmission process. We were able to consistently reproduce experimental data and to quantitatively infer molecular-level causality of a variant-related functional impairment. Therefore, these results show the predictive power of such multiscale approach, aimed to observe behavioral shifts of a complex system that emerge from amplification of small, quantifiable, molecular-level alterations.

---

[*] Our model can be applied to any glutamatergic system. It can also be integrated with other models of the downstream signaling pathways.

4.5 Appendix

Tab. 4.A1 Comparison between peak open probability and deactivation time constants values obtained from our implementation and the ones reported by the original models. Values were obtained by simulating the respective models with 1 glutamate pulse of 1 mM amplitude and 1 ms of glutamate width.

	Peak open probability		**Deactivation time constant (ms)**	
	PySB model	**Original model**	**PySB model**	**Original model**
AMPA	0.32	0.32 [34]	0.54	0.52 [34]
NMDA	0.27	0.27 [35]	162	173 [35]

Tab. 4.A2 List of the parameters used in the equations of the CPC module.

Parameter	**Value**	**Parameter**	**Value**
V_{max}	+67 (mV)	V_{AMPA}	0 (mV)
I_{fast}	0.75	V_{NMDA}	0 (mV)
I_{slow}	0.25	K_M	0.093 (mV^{-1})
τ_{fast}	3 (ms)	R_S	500 (MΩ)
τ_{slow}	25 (ms)	G_{Ca2+}	0.002 ($\mu M \cdot ms^{-1} \cdot mV^{-1}$)
G_{AMPA}	15 (pS)	V_{Ca2+}	130 (mV)
G_{NMDA}	40 (pS)	τ_{Ca2+}	20 (ms)

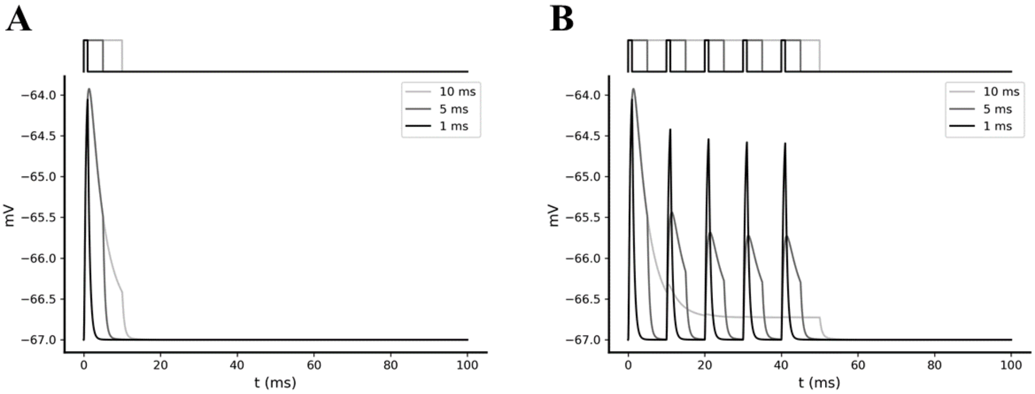

Fig. 4.A1 AMPA-mediated EPSPs generated by pre-synaptic stimulations composed of (A) a single glutamate pulse or (B) a burst of 5 glutamate pulses delivered at 100 Hz. For each stimulation pattern glutamate pulses of 1 mM amplitude were simulated with different widths of 1 ms (black traces), 5 ms (dark gray traces) and 10 ms (light gray traces). We can observe that a small temporal summation only occurs with a pulse duration of 10 ms, reflecting the fast deactivation and desensitization kinetics predicted by the model. Simulations were performed in the presence of 20 AMPA, 15 NMDA and 1 mM Mg^{2+}.

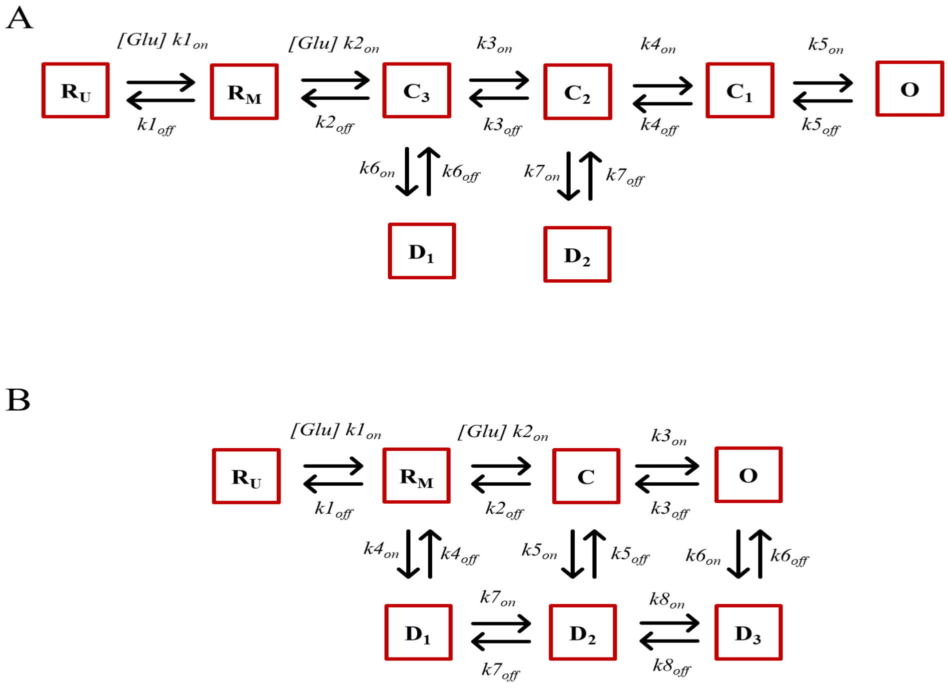

Fig. 4.A2 Kinetic schemes used for simulating the gating mechanisms of **(A)** NMDA and **(B)** AMPA receptors. R_U represent unbound states, R_M represent mono-liganded states (bound to one glutamate), C_n represent closed, fully bound states (bound to two glutamate), D_n represent desensitized states and O represent open states. All the reaction rate constants can be found in the respective articles [34,35].

References

1. Mattson, M.P. Pathways Towards and Away from Alzheimer's Disease. *Nature* **2004**, *430*, 631–639, doi:10.1038/nature02621.

2. Grosjean, B.; Tsai, G.E. NMDA Neurotransmission as a Critical Mediator of Borderline Personality Disorder. *J Psychiatry Neurosci* **2007**, *32*, 103–115.

3. Hsieh, H.; Boehm, J.; Sato, C.; Iwatsubo, T.; Tomita, T.; Sisodia, S.; Malinow, R. AMPA-R Removal Underlies Aβ-Induced Synaptic Depression and Dendritic Spine Loss. *Neuron* **2006**, *52*, 831–843, doi:10.1016/j.neuron.2006.10.035.

4. Snyder, E.M.; Nong, Y.; Almeida, C.G.; Paul, S.; Moran, T.; Choi, E.Y.; Nairn, A.C.; Salter, M.W.; Lombroso, P.J.; Gouras, G.K.; et al. Regulation of NMDA Receptor Trafficking by Amyloid-Beta. *Nat Neurosci* **2005**, *8*, 1051–1058, doi:10.1038/nn1503.

5. Lerma, J.; Marques, J.M. Kainate Receptors in Health and Disease. *Neuron* **2013**, *80*, 292–311, doi:10.1016/j.neuron.2013.09.045.

6. Martin, S.J.; Grimwood, P.D.; Morris, R.G. Synaptic Plasticity and Memory: An Evaluation of the Hypothesis. *Annu Rev Neurosci* **2000**, *23*, 649–711, doi:10.1146/annurev.neuro.23.1.649.

7. Mansvelder, H.D.; Verhoog, M.B.; Goriounova, N.A. Synaptic Plasticity in Human Cortical Circuits: Cellular Mechanisms of Learning and Memory in the Human Brain? *Current Opinion in Neurobiology* **2019**, *54*, 186–193, doi:10.1016/j.conb.2018.06.013.

8. Baez, M.V.; Cercato, M.C.; Jerusalinsky, D.A. NMDA Receptor Subunits Change after Synaptic Plasticity Induction and Learning and Memory Acquisition. *Neural Plast* **2018**, *2018*, doi:10.1155/2018/5093048.

9. Kandel, E.R.; Dudai, Y.; Mayford, M.R. The Molecular and Systems Biology of Memory. *Cell* **2014**, *157*, 163–186, doi:10.1016/j.cell.2014.03.001.

10. Voss, J.L.; Bridge, D.J.; Cohen, N.J.; Walker, J.A. A Closer Look at the Hippocampus and Memory. *Trends Cogn Sci* **2017**, *21*, 577–588, doi:10.1016/j.tics.2017.05.008.

11. Lisman, J.; Buzsáki, G.; Eichenbaum, H.; Nadel, L.; Ranganath, C.; Redish, A.D. Viewpoints: How the Hippocampus Contributes to Memory, Navigation and Cognition. *Nat Neurosci* **2017**, *20*, 1434–1447, doi:10.1038/nn.4661.

12. Kumar, A. Long-Term Potentiation at CA3–CA1 Hippocampal Synapses with Special Emphasis on Aging, Disease, and Stress. *Front Aging Neurosci* **2011**, *3*, doi:10.3389/fnagi.2011.00007.

13. Tsien, J.Z.; Huerta, P.T.; Tonegawa, S. The Essential Role of Hippocampal CA1 NMDA Receptor–Dependent Synaptic Plasticity in Spatial Memory. *Cell* **1996**, *87*, 1327–1338, doi:10.1016/S0092-8674(00)81827-9.

14. Henley, J.M.; Wilkinson, K.A. Synaptic AMPA Receptor Composition in Development, Plasticity and Disease. *Nature Reviews Neuroscience* **2016**, *17*, 337–350, doi:10.1038/nrn.2016.37.

15. Chater, T.E.; Goda, Y. The Role of AMPA Receptors in Postsynaptic Mechanisms of Synaptic Plasticity. *Front. Cell. Neurosci.* **2014**, *8*, doi:10.3389/fncel.2014.00401.

16. Blanke, M.L.; VanDongen, A.M.J. Activation Mechanisms of the NMDA Receptor. In *Biology of the NMDA Receptor*; Van Dongen, A.M., Ed.; Frontiers in Neuroscience; CRC Press/Taylor & Francis: Boca Raton (FL), 2009 ISBN 978-1-4200-4414-0.

17. Vyklicky, V.; Korinek, M.; Smejkalova, T.; Balik, A.; Krausova, B.; Kaniakova, M.; Lichnerova, K.; Cerny, J.; Krusek, J.; Dittert, I.; et al. Structure, Function, and Pharmacology of NMDA Receptor Channels. *Physiol Res* **2014**, *63*, S191-203, doi:10.33549/physiolres.932678.

18. Mayer, M.L.; Westbrook, G.L.; Guthrie, P.B. Voltage-Dependent Block by Mg2+ of NMDA Responses in Spinal Cord Neurones. *Nature* **1984**, *309*, 261–263, doi:10.1038/309261a0.

19. Jahr, C.E.; Stevens, C.F. A Quantitative Description of NMDA Receptor-Channel Kinetic Behavior. *J. Neurosci.* **1990**, *10*, 1830–1837, doi:10.1523/JNEUROSCI.10-06-01830.1990.

20. Feldman, D.E. The Spike Timing Dependence of Plasticity. *Neuron* **2012**, *75*, 556–571, doi:10.1016/j.neuron.2012.08.001.

21. Markram, H.; Gerstner, W.; Sjöström, P.J. A History of Spike-Timing-Dependent Plasticity. *Front. Synaptic Neurosci.* **2011**, *3*, doi:10.3389/fnsyn.2011.00004.

22. Lee, S.-J.R.; Escobedo-Lozoya, Y.; Szatmari, E.M.; Yasuda, R. Activation of CaMKII in Single Dendritic Spines during Long-Term Potentiation. *Nature* **2009**, *458*, 299–304, doi:10.1038/nature07842.

23. Lisman, J.; Yasuda, R.; Raghavachari, S. Mechanisms of CaMKII Action in Long-Term Potentiation. *Nat Rev Neurosci* **2012**, *13*, 169–182, doi:10.1038/nrn3192.

24. Barria, A.; Muller, D.; Derkach, V.; Griffith, L.C.; Soderling, T.R. Regulatory Phosphorylation of AMPA-Type Glutamate Receptors by CaM-KII During Long-Term Potentiation. *Science* **1997**, *276*, 2042–2045, doi:10.1126/science.276.5321.2042.

25. Sibarov, D.A.; Bruneau, N.; Antonov, S.M.; Szepetowski, P.; Burnashev, N.; Giniatullin, R. Functional Properties of Human NMDA Receptors Associated with Epilepsy-Related Mutations of GluN2A Subunit. *Front Cell Neurosci* **2017**, *11*, doi:10.3389/fncel.2017.00155.

26. Shankar, G.M.; Li, S.; Mehta, T.H.; Garcia-Munoz, A.; Shepardson, N.E.; Smith, I.; Brett, F.M.; Farrell, M.A.; Rowan, M.J.; Lemere, C.A.; et al. Amyloid-β Protein Dimers Isolated Directly from Alzheimer's Brains Impair Synaptic Plasticity and Memory. *Nature Medicine* **2008**, *14*, 837–842, doi:10.1038/nm1782.

27. Shipton, O.A.; Leitz, J.R.; Dworzak, J.; Acton, C.E.J.; Tunbridge, E.M.; Denk, F.; Dawson, H.N.; Vitek, M.P.; Wade-Martins, R.; Paulsen, O.; et al. Tau Protein Is Required for Amyloid β-Induced Impairment of Hippocampal Long-Term Potentiation. *J. Neurosci.* **2011**, *31*, 1688–1692, doi:10.1523/JNEUROSCI.2610-10.2011.

28. Bagetta, V.; Ghiglieri, V.; Sgobio, C.; Calabresi, P.; Picconi, B. Synaptic Dysfunction in Parkinson's Disease. *Biochem Soc Trans* **2010**, *38*, 493–497, doi:10.1042/BST0380493.

29. Usdin, M.T.; Shelbourne, P.F.; Myers, R.M.; Madison, D.V. Impaired Synaptic Plasticity in Mice Carrying the Huntington's Disease Mutation. *Hum Mol Genet* **1999**, *8*, 839–846, doi:10.1093/hmg/8.5.839.

30. Murphy, K.P.S.J.; Carter, R.J.; Lione, L.A.; Mangiarini, L.; Mahal, A.; Bates, G.P.; Dunnett, S.B.; Morton, A.J. Abnormal Synaptic Plasticity and Impaired Spatial Cognition in Mice Transgenic for Exon 1 of the Human Huntington's Disease Mutation. *J Neurosci* **2000**, *20*, 5115–5123, doi:10.1523/JNEUROSCI.20-13-05115.2000.

31. Bartol, T.M.; Keller, D.X.; Kinney, J.P.; Bajaj, C.L.; Harris, K.M.; Sejnowski, T.J.; Kennedy, M.B. Computational Reconstitution of Spine Calcium Transients from Individual Proteins. *Front. Synaptic Neurosci.* **2015**, *7*, doi:10.3389/fnsyn.2015.00017.

32. Hu, E.; Mergenthal, A.; Bingham, C.S.; Song, D.; Bouteiller, J.-M.; Berger, T.W. A Glutamatergic Spine Model to Enable Multi-Scale Modeling of Nonlinear Calcium Dynamics. *Front. Comput. Neurosci.* **2018**, *12*, doi:10.3389/fncom.2018.00058.

33. Shouval, H.Z.; Bear, M.F.; Cooper, L.N. A Unified Model of NMDA Receptor-Dependent Bidirectional Synaptic Plasticity. *PNAS* **2002**, *99*, 10831–10836, doi:10.1073/pnas.152343099.

34. Koike, M.; Tsukada, S.; Tsuzuki, K.; Kijima, H.; Ozawa, S. Regulation of Kinetic Properties of GluR2 AMPA Receptor Channels by Alternative Splicing. *J. Neurosci.* **2000**, *20*, 2166–2174, doi:10.1523/JNEUROSCI.20-06-02166.2000.

35. Amico-Ruvio, S.A.; Popescu, G.K. Stationary Gating of GluN1/GluN2B Receptors in Intact Membrane Patches. *Biophys J* **2010**, *98*, 1160–1169, doi:10.1016/j.bpj.2009.12.4276.

36. Pepke, S.; Kinzer-Ursem, T.; Mihalas, S.; Kennedy, M.B. A Dynamic Model of Interactions of Ca2+, Calmodulin, and Catalytic Subunits of Ca2+/Calmodulin-Dependent Protein Kinase II. *PLoS Comput Biol* **2010**, *6*, doi:10.1371/journal.pcbi.1000675.

37. Dzubay, J.A.; Jahr, C.E. The Concentration of Synaptically Released Glutamate Outside of the Climbing Fiber–Purkinje Cell Synaptic Cleft. *J Neurosci* **1999**, *19*, 5265–5274, doi:10.1523/JNEUROSCI.19-13-05265.1999.

38. Moussawi, K.; Riegel, A.; Nair, S.; Kalivas, P.W. Extracellular Glutamate: Functional Compartments Operate in Different Concentration Ranges. *Front Syst Neurosci* **2011**, *5*, doi:10.3389/fnsys.2011.00094.

39. Robert, A.; Howe, J.R. How AMPA Receptor Desensitization Depends on Receptor Occupancy. *J. Neurosci.* **2003**, *23*, 847–858, doi:10.1523/JNEUROSCI.23-03-00847.2003.

40. Nusser, Z.; Lujan, R.; Laube, G.; Roberts, J.D.B.; Molnar, E.; Somogyi, P. Cell Type and Pathway Dependence of Synaptic AMPA Receptor Number and Variability in the Hippocampus. *Neuron* **1998**, *21*, 545–559, doi:10.1016/S0896-6273(00)80565-6.

41. Markram, H.; Lübke, J.; Frotscher, M.; Sakmann, B. Regulation of Synaptic Efficacy by Coincidence of Postsynaptic APs and EPSPs. *Science* **1997**, *275*, 213–215, doi:10.1126/science.275.5297.213.

42. Albensi, B.C.; Oliver, D.R.; Toupin, J.; Odero, G. Electrical Stimulation Protocols for Hippocampal Synaptic Plasticity and Neuronal Hyper-Excitability: Are They Effective or Relevant? *Experimental Neurology* **2007**, *204*, 1–13, doi:10.1016/j.expneurol.2006.12.009.

43. Racca, C.; Stephenson, F.A.; Streit, P.; Roberts, J.D.B.; Somogyi, P. NMDA Receptor Content of Synapses in Stratum Radiatum of the Hippocampal CA1 Area. *J Neurosci* **2000**, *20*, 2512–2522, doi:10.1523/JNEUROSCI.20-07-02512.2000.

44. Lester, R.A.J.; Clements, J.D.; Westbrook, G.L.; Jahr, C.E. Channel Kinetics Determine the Time Course of NMDA Receptor-Mediated Synaptic Currents. *Nature* **1990**, *346*, 565–567, doi:10.1038/346565a0.

45. Swanger, S.A.; Chen, W.; Wells, G.; Burger, P.B.; Tankovic, A.; Bhattacharya, S.; Strong, K.L.; Hu, C.; Kusumoto, H.; Zhang, J.; et al. Mechanistic Insight into NMDA Receptor Dysregulation by Rare Variants in the GluN2A and GluN2B Agonist Binding Domains. *Am J Hum Genet* **2016**, *99*, 1261–1280, doi:10.1016/j.ajhg.2016.10.002.

46. Wells, G.; Yuan, H.; McDaniel, M.J.; Kusumoto, H.; Snyder, J.P.; Liotta, D.C.; Traynelis, S.F. The GluN2B-Glu413Gly NMDA Receptor Variant Arising from a de Novo GRIN2B Mutation Promotes Ligand-Unbinding and Domain Opening. *Proteins* **2018**, *86*, 1265–1276, doi:10.1002/prot.25595.

47. Yuan, H.; Hansen, K.B.; Vance, K.M.; Ogden, K.K.; Traynelis, S.F. Control of NMDA Receptor Function by the NR2 Subunit Amino-Terminal Domain. *J Neurosci* **2009**, *29*, 12045–12058, doi:10.1523/JNEUROSCI.1365-09.2009.

48. Hu, C.; Chen, W.; Myers, S.J.; Yuan, H.; Traynelis, S.F. Human GRIN2B Variants in Neurodevelopmental Disorders. *J Pharmacol Sci* **2016**, *132*, 115–121, doi:10.1016/j.jphs.2016.10.002.

49. Adams, D.R.; Yuan, H.; Holyoak, T.; Arajs, K.H.; Hakimi, P.; Markello, T.C.; Wolfe, L.A.; Vilboux, T.; Burton, B.K.; Fajardo, K.F.; et al. Three Rare Diseases in One Sib Pair: RAI1, PCK1, GRIN2B Mutations Associated with Smith–Magenis Syndrome, Cytosolic PEPCK Deficiency and NMDA Receptor Glutamate Insensitivity. *Molecular Genetics and Metabolism* **2014**, *113*, 161–170, doi:10.1016/j.ymgme.2014.04.001.

50. Hansen, K.B.; Ogden, K.K.; Yuan, H.; Traynelis, S.F. Distinct Functional and Pharmacological Properties of Triheteromeric GluN1/GluN2A/GluN2B NMDA Receptors. *Neuron* **2014**, *81*, 1084–1096, doi:10.1016/j.neuron.2014.01.035.

51. Lopez, C.F.; Muhlich, J.L.; Bachman, J.A.; Sorger, P.K. Programming Biological Models in Python Using PySB. *Mol Syst Biol* **2013**, *9*, 646, doi:10.1038/msb.2013.1.

52. Virtanen, P.; Gommers, R.; Oliphant, T.E.; Haberland, M.; Reddy, T.; Cournapeau, D.; Burovski, E.; Peterson, P.; Weckesser, W.; Bright, J.; et al. SciPy 1.0: Fundamental Algorithms for Scientific Computing in Python. *Nat Methods* **2020**, *17*, 261–272, doi:10.1038/s41592-019-0686-2.

53. Harris, C.R.; Millman, K.J.; van der Walt, S.J.; Gommers, R.; Virtanen, P.; Cournapeau, D.; Wieser, E.; Taylor, J.; Berg, S.; Smith, N.J.; et al. Array Programming with NumPy. *Nature* **2020**, *585*, 357–362, doi:10.1038/s41586-020-2649-2.

54. Hunter, J.D. Matplotlib: A 2D Graphics Environment. *Computing in Science Engineering* **2007**, *9*, 90–95, doi:10.1109/MCSE.2007.55.

55. Stone, D.B.; Tesche, C.D. Topological Dynamics in Spike-Timing Dependent Plastic Model Neural Networks. *Front Neural Circuits* **2013**, *7*, doi:10.3389/fncir.2013.00070.

56. Rackham, O.J.L.; Tsaneva-Atanasova, K.; Ganesh, A.; Mellor, J.R. A Ca2+-Based Computational Model for NMDA Receptor-Dependent Synaptic Plasticity at Individual Post-Synaptic Spines in the Hippocampus. *Front Synaptic Neurosci* **2010**, *2*, doi:10.3389/fnsyn.2010.00031.

57. Lajeunesse, F.; Kröger, H.; Timofeev, I. Regulation of AMPA and NMDA Receptor-Mediated EPSPs in Dendritic Trees of Thalamocortical Cells. *J Neurophysiol* **2013**, *109*, 13–30, doi:10.1152/jn.01090.2011.

58. Pongrácz, F.; Poolos, N.P.; Kocsis, J.D.; Shepherd, G.M. A Model of NMDA Receptor-Mediated Activity in Dendrites of Hippocampal CA1 Pyramidal Neurons. *J Neurophysiol* **1992**, *68*, 2248–2259.

59. Traynelis, S.F.; Wollmuth, L.P.; McBain, C.J.; Menniti, F.S.; Vance, K.M.; Ogden, K.K.; Hansen, K.B.; Yuan, H.; Myers, S.J.; Dingledine, R. Glutamate Receptor Ion Channels: Structure, Regulation, and Function. *Pharmacol Rev* **2010**, *62*, 405–496, doi:10.1124/pr.109.002451.

60. Momiyama, A.; Feldmeyer, D.; Cull-Candy, S.G. Identification of a Native Low-Conductance NMDA Channel with Reduced Sensitivity to Mg2+ in Rat Central Neurones. *J Physiol* **1996**, *494*, 479–492.

61. Benke, T.; Traynelis, S.F. AMPA-Type Glutamate Receptor Conductance Changes and Plasticity: Still a Lot of Noise. *Neurochem Res* **2019**, *44*, 539–548, doi:10.1007/s11064-018-2491-1.

62. Higley, M.J.; Sabatini, B.L. Calcium Signaling in Dendritic Spines. *Cold Spring Harb Perspect Biol* **2012**, *4*, doi:10.1101/cshperspect.a005686.

63. Di Maio, V.; Ventriglia, F.; Santillo, S. A Model of Cooperative Effect of AMPA and NMDA Receptors in Glutamatergic Synapses. *Cogn Neurodyn* **2016**, *10*, 315–325, doi:10.1007/s11571-016-9383-3.

64. Bloodgood, B.L.; Sabatini, B.L. Nonlinear Regulation of Unitary Synaptic Signals by CaV2.3 Voltage-Sensitive Calcium Channels Located in Dendritic Spines. *Neuron* **2007**, *53*, 249–260, doi:10.1016/j.neuron.2006.12.017.

65. Malik-Sheriff, R.S.; Glont, M.; Nguyen, T.V.N.; Tiwari, K.; Roberts, M.G.; Xavier, A.; Vu, M.T.; Men, J.; Maire, M.; Kananathan, S.; et al. BioModels—15 Years of Sharing Computational Models in Life Science. *Nucleic Acids Research* **2020**, *48*, D407–D415, doi:10.1093/nar/gkz1055.

66. Sebaugh, J.L. Guidelines for Accurate EC50/IC50 Estimation. *Pharm Stat* **2011**, *10*, 128–134, doi:10.1002/pst.426.

Part II

Pharmacology modeling and simulation workflows: integrating tools to create and investigate pharmacological models

CHAPTER 5

Development of a structure-quantitative systems pharmacology computational framework

5.1 Introduction

GPCRs are the most common family of human receptors comprising more than 1% of the coding human genome. As they are expressed within every organ system they regulate, consequently, virtually every aspect of physiology. Many statistical studies claim that GPCRs as the largest group of drug targets making up on average ca. 33% for commercial available small-molecule drugs [1–4].

Although many big companies lost their interest and expertise in GPCR targets, the truth is that around 20% of FDA approved drugs each year target these receptors and a new opening up in GPCR-based drug discovery have been stated [5]. In fact, GPCRs are still offering emerging therapeutic opportunities: peptide therapeutics and modification of natural ligands [2,4,6], GPCRs-target antibody therapeutics [7], allosteric sites [8], orphan human GPCRs [9,10], oligomerization [11,12], and biased [1] and bivalent [13] ligands for GPCRs.

Given the importance of the assessment of pharmacodynamic models during the process of drug discovery and the rise of systems pharmacology as a new interdisciplinary field (see *General Introduction* for more details), it appeared reasonable to attempt to develop a computational framework that brings together structural biology information to the systems biology simulations in order to predict the effect of drug-receptor interactions on the receptors' signaling response. In this sense, we are presenting here, a programmable pipeline able to predict dose-response curves from docking structures of agonist/antagonists-receptor interactions.

5.2 The framework pipeline

We develop a fully computational framework to easily predict classical pharmacodynamic models of drug-GPCR (class A) interactions given just as input structural information of the receptor and the ligand. Our framework doesn't use any novel or untested methods. Instead, it brings together free and/or open source bioinformatic tools into a user-friendly pipeline to be used by experts and non-experts. The pipeline was built, as a first instance, in a *jupyter* notebook – an interactive computational environment for replication and exploration of scientific code and analysis. Nowadays, *jupyter* notebooks are being extensively used by the computational biology community, making them the preferred choice to share and rerun computational protocols [14].

All the code under the framework was developed as a *python* module - a *python* file containing *python* classes, functions and statements. This helped us to modularize our code granting its readability, reusability, and deployment. Although the code will not be detailed in this thesis, many libraries were used for its development, such as *SciPy* [15], *Numpy* [16], *Matplotlib* [17], *Pandas* [18], *scikit-learn* [19], *PySB* [20] and *Biopython* [21].

The pipeline we propose (graphically resumed in *Fig. 5.1*), is not static. That is, the users can interact with it at different stages by giving their own data as inputs. We call these stages as input-points, rendering our framework highly dynamic and modular. As a matter of fact, we propose, here, two different ways of using this conceptual framework. Firstly, we propose a *stimulation protocol* to predict the dose-response curves of agonists in order to compare their potencies against a receptor. Secondly, we propose a *competitive inhibition protocol* to predict the inhibition curves of antagonists in the presence of a saturation of agonist.

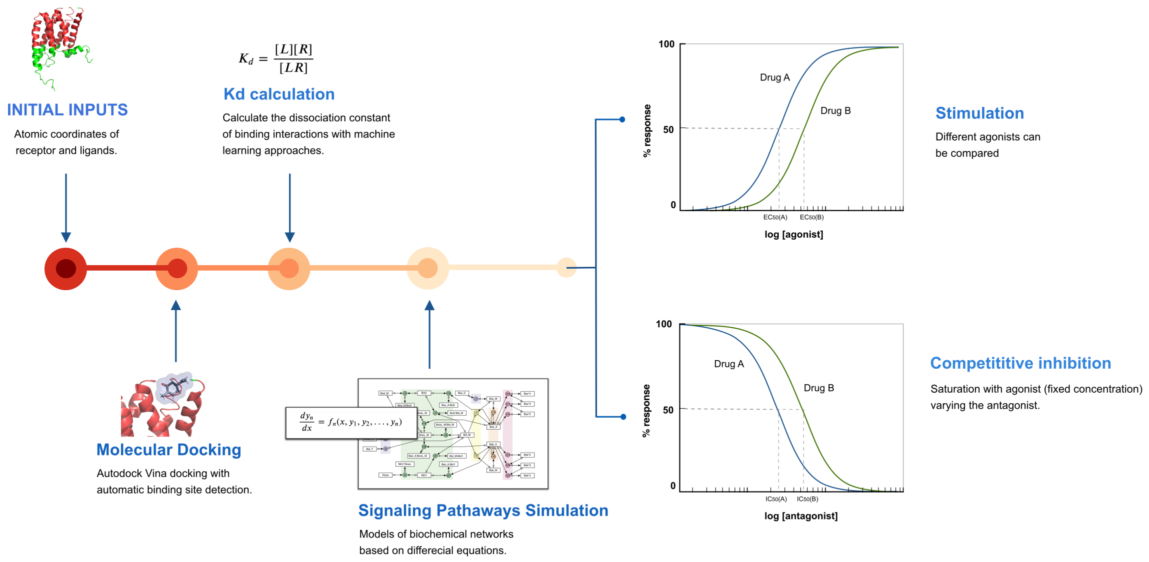

Fig. 5.1 Structure-quantitative systems pharmacology framework's pipeline.

5.2.1 Initial Inputs

Since with this framework we propose a link between biological structure information and quantitative systems pharmacology, the atomic coordinates of the GPCR and ligands constitute the first input-point of the pipeline. Depending on the protocol to be run, the action of the ligand, *i.e.*, agonist or antagonist, must be specified. This is the case for running the competitive inhibition protocol, where the user must classify manually which ligands are agonists and antagonists.

Once the atomic coordinates file of the receptor is obtained, the framework can automatically query an internal *in-house* built database to retrieve relevant information about the protein (see *chapter 6 section 6.2* for more details), like the associated G protein and the gene. The former is important to automatically select, later, which signaling network to simulate (*see section 5.2.4*).

5.2.2 Molecular docking

In the second step of the pipeline, molecular docking calculations are performed. Our *python* framework has implemented a function that performs AutoDock VINA calculations [22] for each ligand to each receptor. This function accepts as inputs some parameters that allow the controlling of the VINA algorithm, like the dimensions of the grid, exhaustiveness, and number of modes [22]. In addition, since the transmembrane binding pocket of GPCRs for small ligands is well conserved, by default, the framework already includes an algorithm that sets automatically the center of the docking grid. Since the results of Vina come out as sorted clusters of binding poses, the cluster with the best Vina score is selected, by default, as the binding pose used to predict the ligand dissociation constant.

5.2.3 Drug-receptor binding and K_d calculation

The concept of drug-receptor binding constitutes the baseline of pharmacodynamics' studies. When a drug or an endogenous ligand such as a neurotransmitter or a hormone binds though complementary to protein conformations, a cellular effect may result from that binding interaction (such as biochemical metabolic effects of second messengers or modulation of basal activity), which is typically described in quantitative terms. This complementary binding depends mainly on the *affinity* and *efficacy* of the ligand – parameters unique to its chemical structure [23]. While the affinity of a ligand can be defined as a measure of how strong the ligand binds to the receptor, the efficacy is the measure of the maximum biological effect that results from the binding.

The affinity of a ligand to a receptor can be calculated according to the law of mass action, from which the equilibrium constant for bound versus unbound ligand is defined as the dissociation constant (K_d), as follows:

$$(eq.\ 5.1) \qquad L + R \rightleftharpoons LR \qquad\qquad (eq.\ 5.2) \qquad K_d = \frac{[L][R]}{[LR]}$$

being [L], [R] and [LR] the ligand, receptor and the ligand-receptor complex's concentration, respectively, and K_d the equilibrium dissociation constant.

If one assumes that the concentration of the receptor is constant: $[LR]+[R]=[R_{total}]$; it comes that:

$$(eq.\ 5.3) \qquad \frac{[LR]}{[R_{total}]} = \frac{[L]}{[L] + K_d}$$

being $[LR]/[R_{total}]$ the fraction of all available receptors that are bound to the ligand at equilibrium. That is to say that if the ligand acts as an agonist, according to the occupancy theory, this fraction represents the concentration of

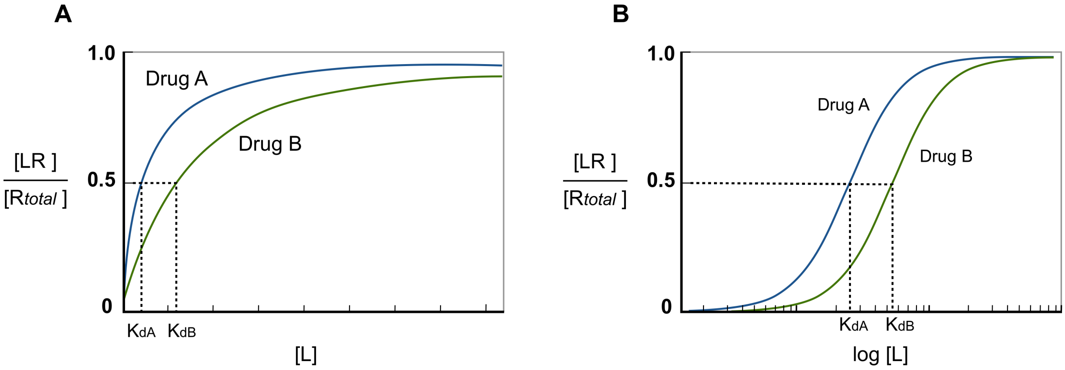

Fig. 5.2 Drug-binding curve. Since ligands can occur in a wide range of concentration values, if the ligand's concentration is plotted semi-logarithmically, the hyperbolic shape of the curve becomes sigmoid. When the curve is presented in this way, a straight line can be obtained between 20% and 80% of the curve, being easy to calculate the concentration of ligand needed to activate specific a fraction of receptors. Moreover, it also makes easier to compare affinities between ligands.

active receptors at equilibrium [23]. From this equation, is possible then, to plot the fraction of bound receptors in the equilibrium over a range of ligand's concentration, rendering the so-called drug-receptor binding curve (*Fig. 5.2*).

Taking into account the importance of *affinity* as a structural binding parameter of ligands and since that our framework intends to link structural biology information with systems biology, the next step in our pipeline is the calculation of K_d from docked structures.

In recent years, with the "*hype*" on machine-learning and artificial intelligence, the cheminformatics' community have been putting a lot of effort on the development of deep learning algorithms tailored for drug-target binding affinity predictions (*Tab. 5.A*). However, most of these machine-learning scoring functions were not already peer-reviewed neither they were trained to estimate drug-target affinities from three-dimensional structural data. On that account, we chose to implement in our framework the DLSCORE deep learning scoring function [24]. Even if it wasn't already peer-reviewed, it was developed and trained on three-dimensional structural data extracted from the refined PDBBind v.2016 [25] and described by BINding ANAlyser (BINANA) descriptors [26]. Moreover, DLSCORE proved to outperform other scoring function regarding consistency and variability, getting the closest values to the experimental data in terms of ΔG values [24]. In addition, it is the only trained neuro-network with such properties that is open source hitherto.

Nevertheless, this stage of the pipeline constitutes another input-point in our framework: one can use the docking structures resolved from the previous steps or give as input one's docking structures obtained with other popular software, for instance GOLD [27], SurFlex [28], or Glide [29], or even give as input its own experimental or computational K_d values.

After obtaining a list of K_d estimated values for each ligand, with our framework it is then possible to obtain a drug-receptor binding curve for each ligand by calculating *eq. 5.3* in function of a range of ligand concentrations. In our framework, by default, the range of ligand concentration is defined as a geometric progression of 20 concentration values between a minimum value (close to zero) and a maximum value defined by the user (normally, 3 orders of magnitude higher). In the end, a binding curve for each ligand is obtained by fitting a logistic regression to the discrete data:

$$(eq.\ 5.4) \qquad Y = \frac{a-d}{1+\left(\frac{X}{c}\right)^{b}} + d$$

where Y is the response[§]; X, is the arithmetic ligand concentration; a, the response when $X = 0$; d, the response when X is equal to the maximum ligand's concentration; c[**]; is the concentration value corresponding to the halfway between a and d; and b is the "slope" value that describes the steepness of the curve [30].

The reason why a geometric progression is used to obtain the range of ligand concentrations, is due to the impact of the dilution factor on the accuracy of K_d and EC_{50}/IC_{50} values experimentally estimated. This factor, that defines the spacing between the adjacent concentration values, has an impact on the concentration values that are on the linear portion of the curve. Using a geometric progression we can mimic the experimental conditions where each concentration equals the power of 2 of the previous lowest concentration [31].

Obtaining then the drug-receptor binding curve for each ligand, allows us to compare the potencies between them. Considering the assumption that K_d can be defined as the concentration of ligand at which 50% of the available receptors are occupied, the more the K_d shifts to right in the plot, the more ligand concentration is needed to achieve the 50% of available occupied receptors (see *Fig. 5.2*). In other words, the more the K_d goes to right in the plot the less potent the drug is.

However, this analysis is just valid if we are dealing with agonists. If antagonists come into play the scenario is different. By definition, an antagonist is a drug that inhibits the action of an agonist, having no effect in the absence of

---

[§] The response of a drug-binding curve is the fraction of receptors occupied in the equilibrium.

[**] For a drug-response curve, the c value corresponds to the K_d value.

the agonist [32]. Therefore, to incorporate the effect of a competitive antagonist, a modified version of *eq. 5.3* must be applied:

$$(eq.\ 5.5) \qquad \frac{[L_1R]}{[R_{total}]} = \frac{[L_1]}{[L_1] + K_{d_{L1}}\left(1 + \frac{[L_2]}{K_{d_{L2}}}\right)}$$

The only difference is the increase in the K_d of the effective ligand by a factor of: $1+[L_2]/K_{d\,L2}$ [23].

In order to apply *eq. 5.5* to obtain drug-receptor binding curve of an antagonist in the presence of an agonist we mimic computationally a binding assay experiment. In a radioligand binding assay, a known ligand for the target receptor is labelled with radioactivity and added to the system (cell or tissue). After reaching the equilibrium the radioligands are “washed out” and the effective ligand (radioactively unlabeled) is added to the system. The latter called “displacer”, will compete with the radioligand for the binding site in the receptor, and the stronger its affinity, the more effectively will bind and displace the radioligand. Such affinity can be inferred by the amount of radioactivity observed in the system [33].

In the same vein, in our framework, we obtain the drug-receptor binding curve of antagonist in the presence of an agonist applying then, the *eq. 5.5* over a range of antagonist concentration values with a fixed concentration value for the agonist. However, to find the agonist concentration value that saturates the receptor, we have to calculate first its submaximal concentration, *i.e.*, the concentration of agonist for which the fraction of occupied receptor reaches the maximum plateau on the agonist-receptor binding curve (*Fig. 5.2*). This plateau can be defined as the upper bend point of the linear portion of the sigmoid curve [34]. Mathematically, this bend point can be obtained by calculating the maximum value of the derivative function of the logistic function (*eq. 5.4*) with respect to *b* (*Fig. 5.3*) [34].

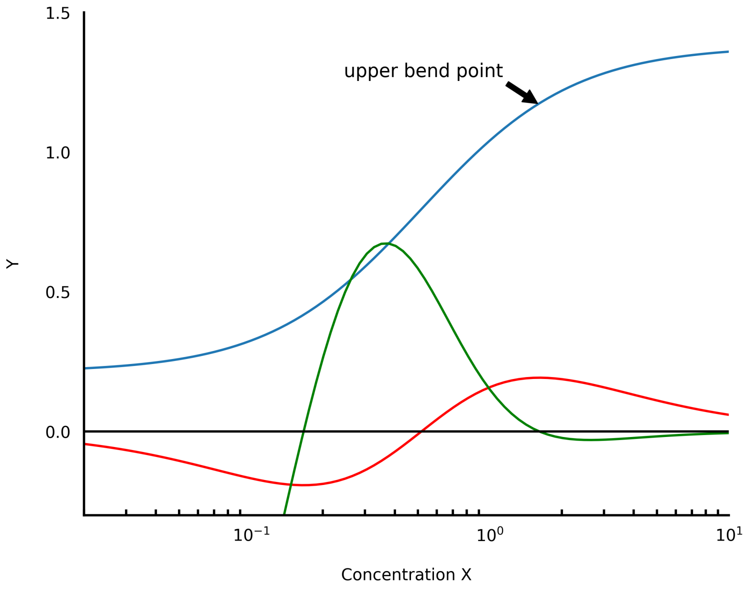

Fig. 5.3 Bending point – The red curve is the first derivative with respect to b. The minimum and maximum values of this curve give us the bending points. The green curve is the first derivative with respect to b and x. The bending points can be obtained resolving numerically this function in order a zero. Figure adapted from *Sebaugh and McCray,2003* [34].

As a matter of fact, in functional studies, the IC_{50} values of antagonists are useful if the concentration of the agonist is submaximal, because higher concentration of agonist increases the IC_{50} of antagonist well above its K_d [32].

5.2.4 Network response

Up to this point, with our framework we are able to predict from a structure of a ligand docked to a receptor its affinity constant and, consequently, obtain a drug-receptor binding curve. However, the pharmacodynamics of a drug is characterized by the relationship between the dose – *i.e.*, the drug's concentration – and the response to that drug.

Since drug targets are coupled to the cell through a myriad of biochemical reactions, the response of a drug is characterized by signaling effects of second

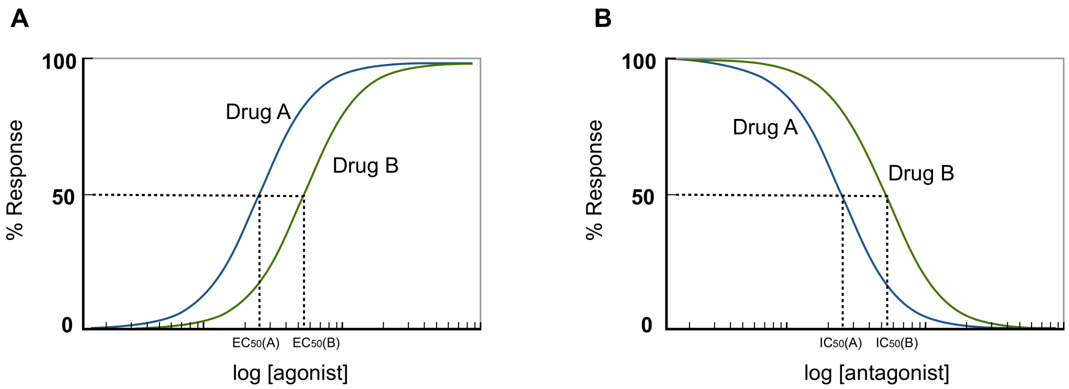

Fig. 5.4 Dose-response curve demonstrating the effect of a drug as a function of its concentration.

messengers or the modulation of basal activity of the cell. In functional studies, this response is normally represented by a dose-response curve (*Fig. 5.4*) from which the *potency* parameters can be deduced. The *potency* parameter expresses the activity of a drug in terms of concentration of ligand needed to produce a defined effect, which is normally defined by the EC_{50} and IC_{50} values for agonist and antagonist, respectively. While EC_{50} represents "*the molar concentration of an antagonist that produces 50% of the maximal possible effect of that agonist*" [32], the IC_{50} represents "*the molar concentration of an antagonist that reduces the response to an agonist by 50% or the concentration of agonist should be given*" [32].

Typically, it is assumed that the response of a drug is proportional to the fraction of activated receptors, however, this assumption is not valid for the so-called "*spare receptors*" like GPCRs. That is to say that the maximum response of a GPCR can be achieved with less than 100% of occupancy [23]. As this implies, we can't estimate the EC_{50}/IC_{50} of ligands of GPCRs without including the signaling pathway associated with these receptors.

Under the umbrella of systems biology, descriptive models of signaling pathways can be used to predict cellular responses. This is possible due to the fact that signaling pathways are an intricate series of molecular events, commonly protein phosphorylation catalyzed by kinases, that can be described by mathematical equations. So, by simulating a mathematical model of a signal-transduction pathway it is possible to predict how the concentration of species (metabolites and proteins) change over time depending on certain initial conditions [35]. Therefore, mathematical models of the GPCR signaling pathways make part of the core of our framework.

Since G-protein subfamilies are classified by their α subunits, this classification has been served to define either the receptor and the effector coupling, and also the signaling pathway [36]. Hence, GPCR pathways have been divided into four families: G_s, $G_{i/o}$, $G_{q/11}$, and $G_{12/13}$ (*Fig. 5.5*).

To implement the GPCR signaling pathways in our framework we developed them based on pre-existing models. The G_s and $G_{i/o}$ pathways were implemented based on the model proposed by *Nair et al.* [38], whereas the $G_{q/11}$ pathway were based on the model proposed by *Chang et al.* [39]. Although we didn't find, in the literature, a suitable descriptive model for the $G_{12/13}$ signaling pathway, this pathway shares the same receptors as the $G_{q/11}$ pathway. Moreover, from all known human GPCRs, just 1% of them are known to couple the $G_{12/13}$ signaling pathway (*Fig. 5.6*).

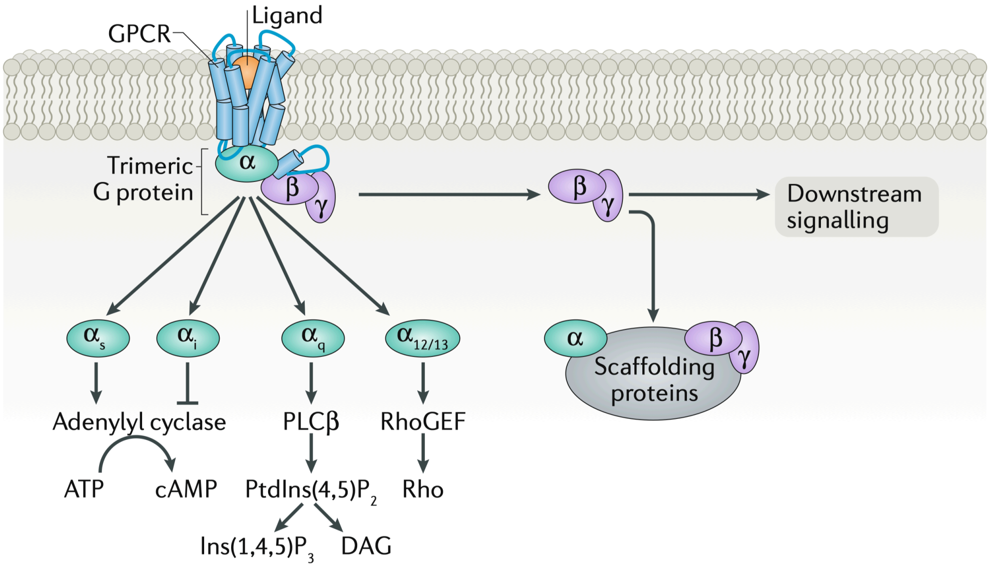

Fig. 5.5 GPCRs' signaling pathways. Figure taken from *Pfleger et al.* 2019 [37].

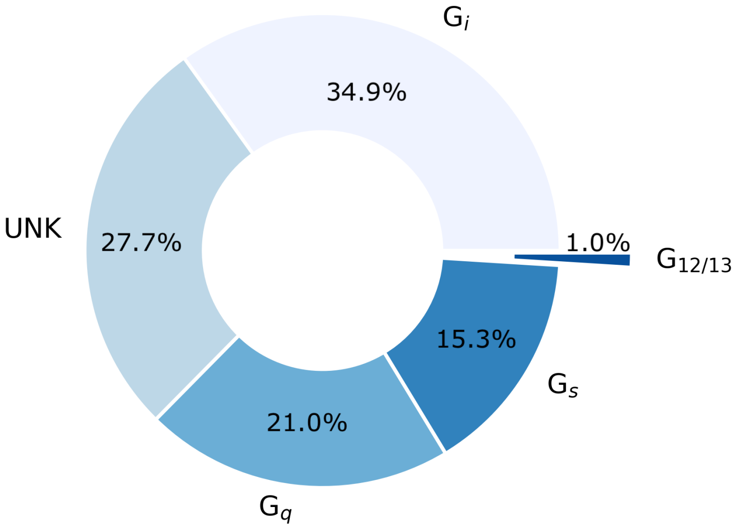

Fig. 5.6 Percentage of human GPCRs in function of their G protein. Data based on GPCRdb and REACTOME database (last access on December 2020) [40,41] (UNK = unknown).

All the three signaling pathways were developed using the PySB [20] framework, designed specifically for systems biology. Essentially, with PySB [20] we start by defining all the species, initial concentrations, reactions and reactions constants. Then, all the differential equations are integrated over an *array* of time, and finally, the variation of the concentration of specific metabolites over time are obtained.

To predict a dose-response curve from the simulation of signaling pathways, individual simulations of the pathway according to an array of ligand concentrations must be performed first. The dose-response curve is, then, obtained by fitting a logistic regression (*eq. 5.4*[††]) to the maximum response values from each individual simulation. In the end, a curve of the response in function of the ligand concentration is obtained (*Fig. 5.7*). The response of a

---

[††] For a drug-response curve, the *c* value of the logistic function corresponds to the EC_{50}/IC_{50} value.

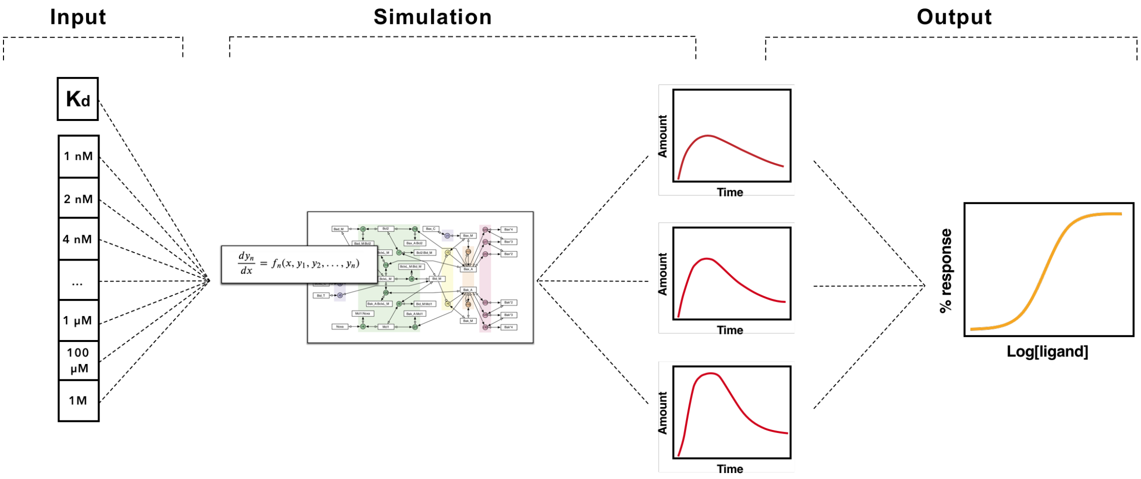

Fig. 5.7 Conceptual scheme for predicting dose-response through signaling pathways' simulation. For each concentration value the signaling model is simulated obtaining in the end several curve of the concentration of a specific species of the pathway as function of time. After, the maximum value of each curve is selected and plotted, resulting, in the end, in the dose-response curve.

signaling pathway is, naturally, represented by the increase or decrease of one of the species described by the model. Therefore, for each signaling pathway we defined, by default, a reference species. While cAMP was chosen as reference species for the G_s and $G_{i/o}$ pathway, for the $G_{q/11}$ pathway we chose IP_3, *Fig. 5.5*.

Having this in mind, with our framework it is then possible to obtain curves for the response of agonists (*stimulation protocol*) and antagonists (*competitive inhibition protocol*).

Since the comparison between drugs' potencies should only be made under specific experimental conditions [32], our framework might become a computational approach to systematically assess pharmacodynamic parameters during virtual screening campaigns against GRCRs.

5.3 Application cases: Adenosine 2A receptor

The physiological role of adenosine on virtually every tissue and organ has long been reported. Adenosine is a physiological nucleoside which activates G protein-coupled receptors referred to as A_1, A_{2A}, A_{2B} and A_3. Due to their broad distribution across the human body, they are related to a multitude of pathologies, such as cardiovascular, renal, pulmonary, neurodegenerative and autoimmune diseases, ischemia, diabetes, and even cancer. Their role is so important that during the last four decades, numerous agonists have been developed, all of them structurally based on adenosine. In fact, adenosine itself is being used as a vasodilatory agent either during cardiac surgeries either to treat tachycardia and arrhythmias [42,43].

In particular, from all adenosine receptors, the A_{2A} receptor is the best studied and characterized by a structural point of view [46]. Therefore, due to the vast quantity of structural data, I will, hereby, apply the two proposed framework protocols to obtain classical pharmacodynamics' models of agonists and antagonists for A_{2A} receptors.

5.3.1 Stimulation protocol

The proposed stimulation protocol was performed using adenosine - the endogenous ligand - and the two more common agonists for A_{2A} receptors used in functional studies: NECA and NGI (*Fig. 5.8 A*). The three-dimensional structure of each ligand was obtained from *PubChem* [44], and three-dimensional structure of the receptor was obtained from the *Protein Data Bank* [45]. We chose the PDB ID: *2DYV*, an X-ray solved structure complexed with the agonist NECA with a resolution of 2.60 Å [46]. Because this structure contains a thermostabilized mutation on the binding pocket, this residue was re-mutated, *in silico*, to obtain the original amino acid sequence using the MODELLER program [47].

Once receptor and ligand structures were obtained, we follow the protocol as described in sections *5.2.3* and 5.2.4. For simulation of the network model, we used a receptor concentration of 2 μM, a range of ligand concentration

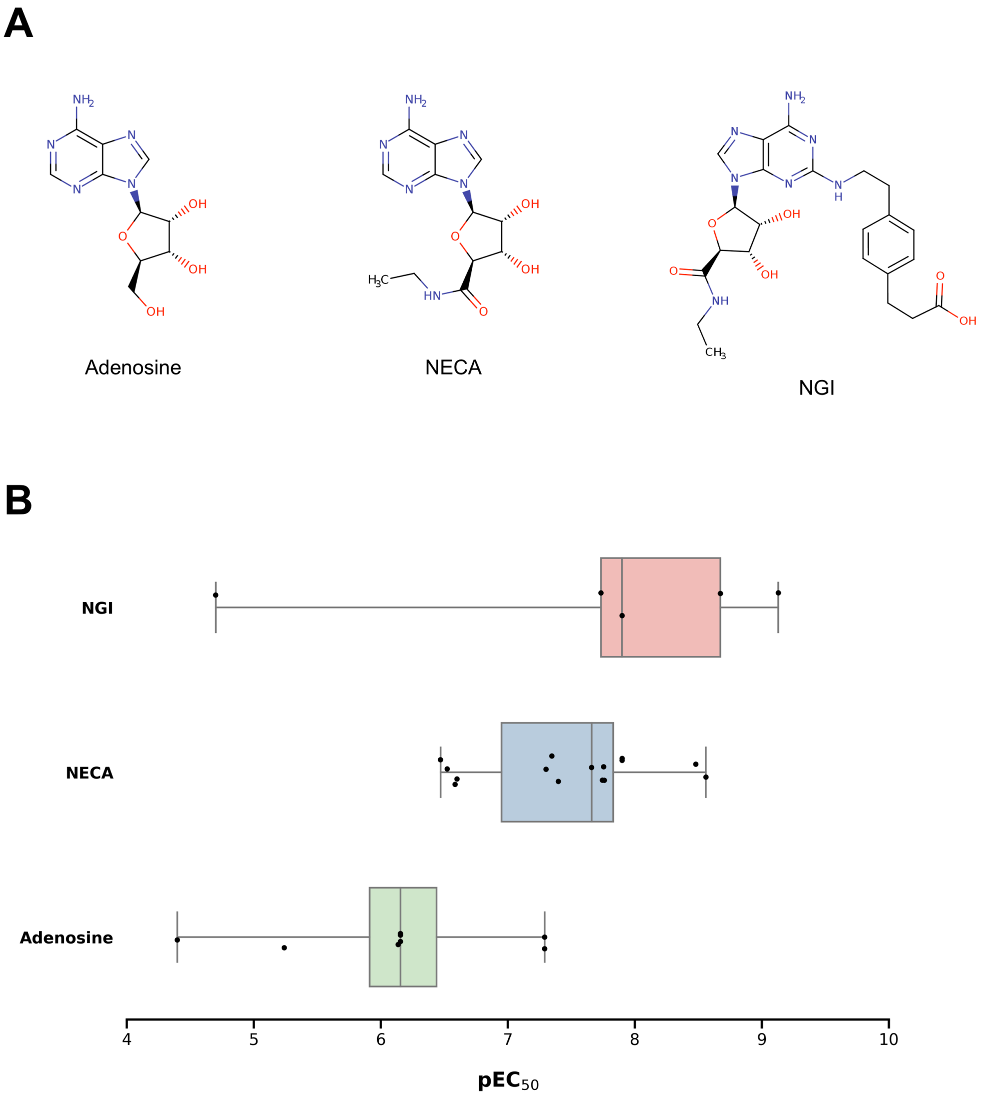

Fig. 5.8 A) chemical representation of the A2A receptor agonists adenosine, NECA and NGI. **B)** Statistical distribution of the experimental values of EC50 relative to the interaction between the adenosine, NECA and NGI with the A2A receptor, respectively. Data taken from *PubChem* [44] (last access on December 2020).

between 10^{-3} μM and 10^{3} μM, and an integral time step of 1000. The results obtained from our protocol (*Fig. 5.9 and Tab. 5.1*) predicted that from the list of ligands tested, the NGI is the most potent agonist, followed by the NECA, being the Adenosine the less potent ligand. Compared with experimental data, *Fig. 5.8B*, one can observe that even if our framework is not able to reproduce the experimental EC_{50} absolute values, it is able to reproduce the potency pattern: NGI > NECA > Adenosine.

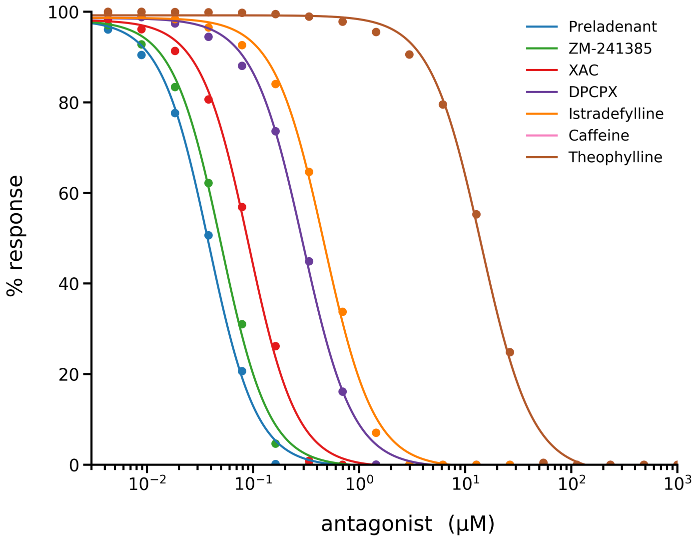

Fig. 5.9 Dose-response curves of agonists (Adenosine, NECA and NGI) of A_{2A} receptor obtained through our framework.

Tab. 5.1 Results obtained from our framework applied to agonists towards the A_{2A} receptor.

Ligand	Vina score (kcal·mol^{-1})	DLSCORE (pK_d)	Predicted EC_{50} (μM)	Predicted pEC_{50}	Experimental* pEC_{50}
Adenosine	-7.1	4.45	1.62	5.79	6.15
NECA	-8.01	4.73	0.9	6.04	7.66
NGI	-9.96	6.04	0.13	6.90	7.90

*Median values calculated from the experimental values of EC50 relative to the interaction between the agonists with the A_{2A} receptor, respectively. Data taken from *PubChem* [48] (last access on December 2020).

5.3.2 Competitive inhibition protocol

Although many adenosine A_2 selective agonists have been used therapeutically, due to the pathophysiological role of A_{2A} receptors on Alzheimer and Parkinson's disease, de development of antagonists for A_{2A} receptors have been highly attractive [48].

Therefore, we applied the proposed competitive inhibition protocol to compare different antagonists for A_{2A} receptors (*Fig. 5.10 A)*. Such antagonists were selected because not only are some of the most used commercial drugs (*theophylline*, *caffeine*, *istradefylline* and *preladenant*) or used in functional studies (*ZM-241385*, *XAC* and *DPCPX*), but also because there are extensive experimental pharmacodynamic data on them. The three-dimensional structure of all ligands were obtained, once again, from *PubChem* [44], and the three-dimensional structure of the receptor was obtained from the *Protein Data Bank* [45]. In this study, we chose the PDB ID: *5IU4*, an X-ray solved structure complexed with the agonist ZM-241385 with a resolution of 1.70 Å [49]. Because this structure contains thermostabilized mutations on the binding pocket, such residues were re-mutated*, in silico*, to obtain the original amino acid sequence using the MODELLER program [47].

The protocol was performed as described in sections *5.2.3* and 5.2.4. For simulation of the network model, we used a receptor concentration of 2 μM, a range of ligand concentration between 10^{-3} μM and 10^{3} μM, and an integral time step of 1000. The results obtained from our protocol (*Fig. 5.11 and Tab. 5.2*), predicted that from the list of antagonists tested, the *preladenant* is the most potent antagonist, followed sequentially by *ZM-241385*, *XAC*, *DPCPX*, *istradefylline,* and *caffeine,* being the *theophylline* the less potent predicted ligand. Since experimental values for IC_{50} of these antagonists are scarce, and due to the fact that IC_{50} is an ambiguous term, being sometimes used as a measure regarding the reduction of a response to an antagonist or regarding the inhibition of binding of radioligand [32], we compared the predicted potency's values with the affinity constants. Even if such constants represent different biochemical properties, one should expect that they are proportionately related. Thus, comparing with experimental affinity data (K_i[‡‡]) (*Fig. 5.10 B*), we can observe that the predicted inhibition pattern follows the experimental affinity pattern: *preladenant* > *ZM-241385* > *XAC* > *DPCPX* > *istradefylline* > *caffeine and theophylline*.

5.4 Discussion

Hereby, we developed a computational framework able to qualitatively predict the dose-response curves from docking structures of agonist/antagonists-receptor interactions. However, there are many challenges to overcome in order to implement such a framework in drug discovery high-throughput virtual screening campaigns.

The first pitfall arises from the docking technique. Although it has been the best option to predict favorable binding conformations of ligands, many of them fail in *in vivo* experiments despite their high docking scores [50]. As well as other techniques, what is suitable for certain systems may not work for others. Indeed, the accuracy of docking algorithms vary depending on the target being tested and the kind of molecules being docked. For instance, if the screening library is beyond the chemical space for which the algorithms were trained and developed, they will not provide the same results with the same reliability [50]. In addition, in our framework we implement a *rigid docking* approach. In this kind of docking, the bond angles and lengths of protein and ligand are fixed. The search algorithm will then dock randomly the ligand, rotating and translating it after. Finally, the fact that the target protein, normally obtained from the PDB database, has already a specific conformation, because proteins are commonly co-crystalized with ligands, can affect the docking results [50].

Although a *flexible docking* type could be an alternative to the rigid docking in order to enhance the results, molecular dynamics may be the best option to

---

[‡‡] The lower case subscript of the binding constant describes the pharmacological experiment: direct binding for K_d and inhibition for K_i [32].

predict binding poses. The drawback, here, is the time and computational cost that molecular dynamics simulations require. However, the Hybrid MM/CG (molecular mechanics/coarse-grained) technique proposed by *Schneider et al.* promises to predict with high quality the ligand binding poses, even with low resolution protein models, keeping the computational cost low [51].

Another pitfall in our framework is the use of the affinity constants, K_d, as the exclusive parameter for calculate the concentration of activated receptors. The reality is that not only docking scores and experimental binding affinities are still poorly correlated, but also new activation models of receptors are taking into account three distinct parameters: *i)* the dissociation constant (K_d) that characterizes the equilibrium binding affinity; *ii)* the efficacy parameter that describes the receptor activation; *iii)* and the amplification parameter that represents the post-activation signal transduction [52]. Furthermore, some studies have recently demonstrated that the residence time (k_{off}^{-1}) of the ligand inside the binding pocket plays a more important role in regulating cellular responses than its affinity and potency [53–55]. As this implies, recently many computational approaches, applying statistical machine learning or molecular dynamics simulations combined with enhanced sampling techniques, have been developed to derive drug binding kinetics [55–58]. Since our mathematical models of signaling pathways are based on binding kinetic equations, we intend, in the near future, to implement the prediction of the drug-receptor binding k_{off} parameter in order to enhance our receptor activation model.

Finally, the accuracy of the kinetic parameters constitutes the last limitation of our framework. Although many of them are derived experimentally, they are dependent on the experimental conditions. Also, despite the next generation of binding kinetics predictors, we have yet to understand if such parameters are transferable, so they can be used in molecular systems other than those for which they were predicted and how they can be optimized.

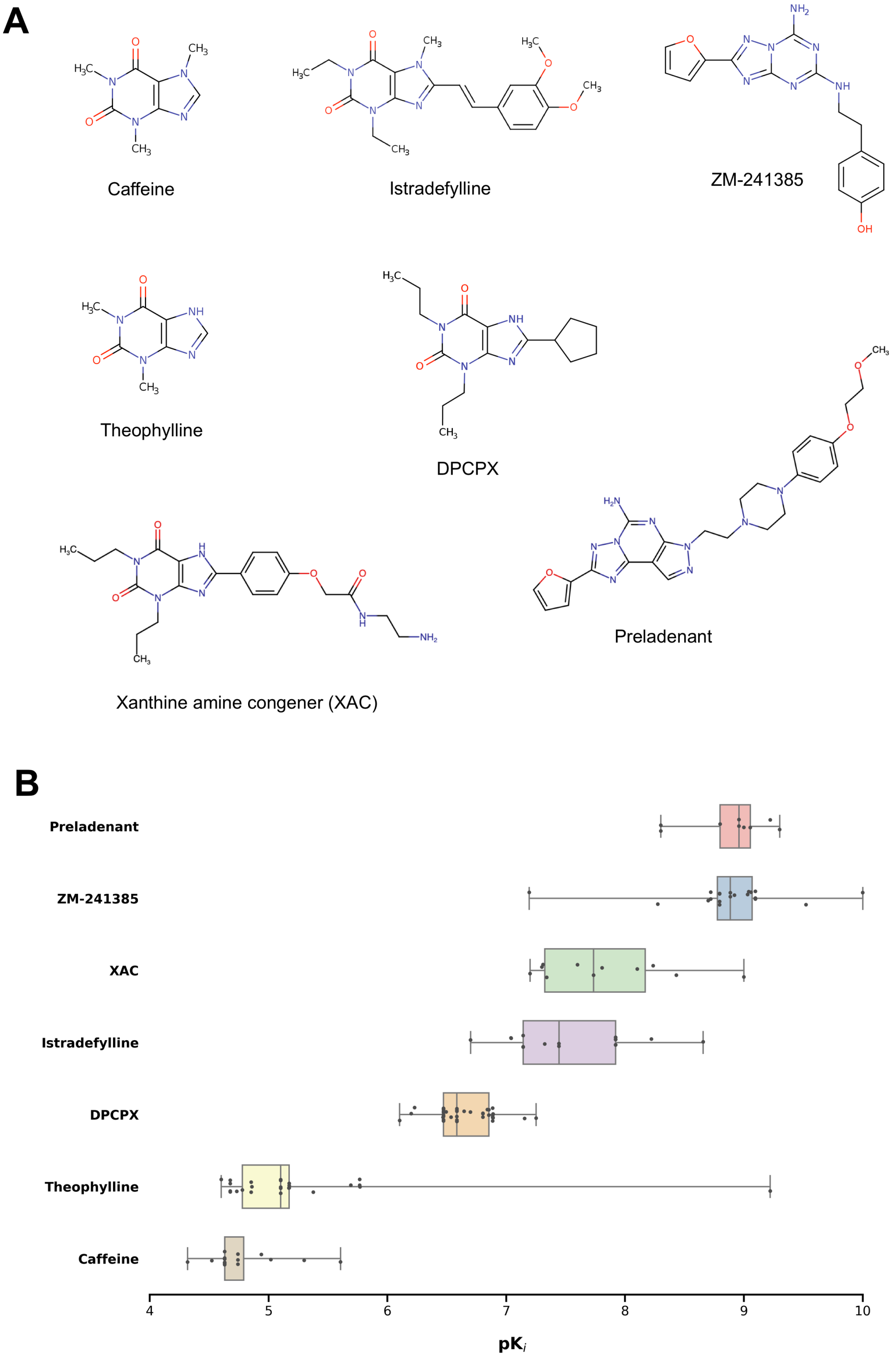

Fig. 5.10 **A)** chemical representation of the A$_{2A}$ receptor antagonists: caffeine, DPCPX, Istradefylline, preladenant, theophylline, xanthine amine congener (XAC) and ZM-21385. **B)** Statistical distribution of the experimental values of Ki relative to the binding interaction between the antagonists with the A$_{2A}$ receptor. Data taken from PubChem [44] (last access on December 2020).

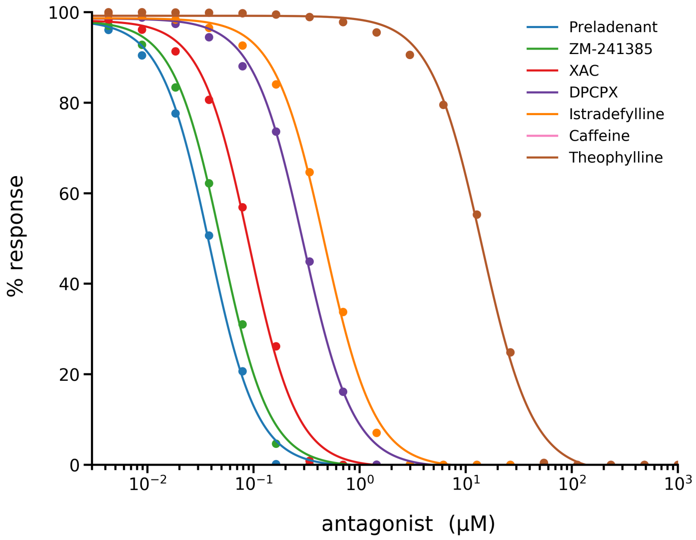

Fig. 5.11 Inhibition curves of antagonists (caffeine, DPCPX, Istradefylline, preladenant, theophylline, xanthine amine congener (XAC) and ZM-21385) of A_{2A} receptor obtained through our framework. The curves of caffeine and theophylline are superimposed.

Tab. 5.2 Results obtained from our framework applied to agonists towards the A_{2A} receptor.

Ligand	Vina score (kcal·mol^{-1})	DLSCORE (*pK$_d$*)	Predicted IC$_{50}$ (μM)	Predicted pIC$_{50}$	Experimental* *pKi*
Theophylline	-5.94	3.70	14.1	4.85	5.10
Caffeine	-6.33	3.91	8.76	5.06	4.63
Istradefylline	-8.32	5.18	0.47	6.33	7.44
DPCPX	-7.74	5.38	0.29	6.53	6.58
XAC	-8.72	5.90	0.09	7.04	7.74
ZM-241385	-9.12	6.17	0.05	7.30	8.89
Preladenant	-7.9	6.28	0.04	7.42	8.96

*Median values calculated from the experimental values of pK_i relative to the interaction between the antagonists for the A_{2A} receptor, respectively. Data taken from *PubChem* [44] (last access on December 2020)).

5.5 Appendix

Tab. 5.A Comparison of the computational estimation tools for drug-target binding affinities.

	Type	Docking Structure-based	Open source	Published	Reference	Date
DeepAffinity	Unified RNN-CNN	No	Yes	Yes	https://doi.org/10.1093/bioinformatics/btz111	2018
DeepDTA	CNN	No	Yes	Yes	https://doi.org/10.1093/bioinformatics/bty593	2018
DLSCORE	Fully connected CNN	Yes	Yes	No	https://doi.org/10.26434/chemrxiv.6159143.v1	2018
KDeep	3D-CNN	Yes	No	Yes	https://doi.org/10.1021/acs.jcim.7b00650	2018
PADME	Graph CNN	No	No	No	https://arxiv.org/abs/1807.09741v1	2018
DeepAtom	3D-CNN	Yes	No	No	http://arxiv.org/abs/1912.00318	2019
DeepConv-DTI	CNN	No	Yes	Yes	https://doi.org/10.1371/journal.pcbi.1007129	2019
WideDTA	CNN	No	No	No	https://arxiv.org/abs/1902.04166	2019
DeepAction	CNN	No	No	Yes	https://doi.org/10.1016/j.ab.2020.113978	2020
GANsDTA	GANs	No	No	Yes	https://doi.org/10.3389/fgene.2019.01243	2020
GEFA	Graph-in-Graph NN	No	yes	No	https://arxiv.org/abs/2009.12146	2020
FAST	3D-CNN+GNN	Yes	Yes	Yes	https://doi.org/10.1021/acs.jcim.0c01306	2021

RNN – Recurrent neural network
CNN – Convolutional neural network
GAN – Graph neural network
GAN – Generative adversarial network
GNN – Generative neural network

References

1. Oprea, T.I.; Bologa, C.G.; Brunak, S.; Campbell, A.; Gan, G.N.; Gaulton, A.; Gomez, S.M.; Guha, R.; Hersey, A.; Holmes, J.; et al. Unexplored Therapeutic Opportunities in the Human Genome. *Nature Reviews Drug Discovery* **2018**, *17*, 317–332, doi:10.1038/nrd.2018.14.

2. Rask-Andersen, M.; Almén, M.S.; Schiöth, H.B. Trends in the Exploitation of Novel Drug Targets. *Nature Reviews Drug Discovery* **2011**, *10*, 579–590, doi:10.1038/nrd3478.

3. Santos, R.; Ursu, O.; Gaulton, A.; Bento, A.P.; Donadi, R.S.; Bologa, C.G.; Karlsson, A.; Al-Lazikani, B.; Hersey, A.; Oprea, T.I.; et al. A Comprehensive Map of Molecular Drug Targets. *Nature Reviews Drug Discovery* **2017**, *16*, 19–34, doi:10.1038/nrd.2016.230.

4. Hauser, A.S.; Attwood, M.M.; Rask-Andersen, M.; Schiöth, H.B.; Gloriam, D.E. Trends in GPCR Drug Discovery: New Agents, Targets and Indications. *Nature Reviews Drug Discovery* **2017**, *16*, 829–842, doi:10.1038/nrd.2017.178.

5. Mullard, A. Fiona Marshall. *Nature Reviews Drug Discovery* **2018**, *17*, 158–159, doi:10.1038/nrd.2018.25.

6. Demartis, A.; Lahm, A.; Tomei, L.; Beghetto, E.; Di Biasio, V.; Orvieto, F.; Frattolillo, F.; Carrington, P.E.; Mumick, S.; Hawes, B.; et al. Polypharmacy through Phage Display: Selection of Glucagon and GLP-1 Receptor Co-Agonists from a Phage-Displayed Peptide Library. *Scientific Reports* **2018**, *8*, 585, doi:10.1038/s41598-017-18494-5.

7. Hutchings, C.J.; Koglin, M.; Olson, W.C.; Marshall, F.H. Opportunities for Therapeutic Antibodies Directed at G-Protein-Coupled Receptors. *Nature Reviews Drug Discovery* **2017**, *16*, 787–810, doi:10.1038/nrd.2017.91.

8. Thal, D.M.; Glukhova, A.; Sexton, P.M.; Christopoulos, A. Structural Insights into G-Protein-Coupled Receptor Allostery. *Nature* **2018**, *559*, 45–53, doi:10.1038/s41586-018-0259-z.

9. Cohen, L.J.; Esterhazy, D.; Kim, S.-H.; Lemetre, C.; Aguilar, R.R.; Gordon, E.A.; Pickard, A.J.; Cross, J.R.; Emiliano, A.B.; Han, S.M.; et al. Commensal Bacteria Make GPCR Ligands That Mimic Human Signalling Molecules. *Nature* **2017**, *549*, 48–53, doi:10.1038/nature23874.

10. Kim, K.-S.; Seeley, R.J.; Sandoval, D.A. Signalling from the Periphery to the Brain That Regulates Energy Homeostasis. *Nature Reviews Neuroscience* **2018**, *19*, 185–196, doi:10.1038/nrn.2018.8.

11. George, S.R.; O'Dowd, B.F.; Lee, S.P. G-Protein-Coupled Receptor Oligomerization and Its Potential for Drug Discovery. *Nature Reviews Drug Discovery* **2002**, *1*, 808–820, doi:10.1038/nrd913.

12. Ferré, S. The GPCR Heterotetramer: Challenging Classical Pharmacology. *Trends in Pharmacological Sciences* **2015**, *36*, 145–152, doi:10.1016/j.tips.2015.01.002.

13. Pérez-Benito, L.; Henry, A.; Matsoukas, M.-T.; Lopez, L.; Pulido, D.; Royo, M.; Cordomí, A.; Tresadern, G.; Pardo, L. The Size Matters? A Computational Tool to Design Bivalent Ligands. *Bioinformatics* **2018**, *34*, 3857–3863, doi:10.1093/bioinformatics/bty422.

14. Rule, A.; Birmingham, A.; Zuniga, C.; Altintas, I.; Huang, S.-C.; Knight, R.; Moshiri, N.; Nguyen, M.H.; Rosenthal, S.B.; Pérez, F.; et al. Ten Simple Rules for Writing and Sharing Computational Analyses in Jupyter Notebooks. *PLoS Comput Biol* **2019**, *15*, e1007007, doi:10.1371/journal.pcbi.1007007.

15. Virtanen, P.; Gommers, R.; Oliphant, T.E.; Haberland, M.; Reddy, T.; Cournapeau, D.; Burovski, E.; Peterson, P.; Weckesser, W.; Bright, J.; et al. SciPy 1.0: Fundamental Algorithms for Scientific Computing in Python. *Nat Methods* **2020**, *17*, 261–272, doi:10.1038/s41592-019-0686-2.

16. Harris, C.R.; Millman, K.J.; van der Walt, S.J.; Gommers, R.; Virtanen, P.; Cournapeau, D.; Wieser, E.; Taylor, J.; Berg, S.; Smith, N.J.; et al. Array Programming with NumPy. *Nature* **2020**, *585*, 357–362, doi:10.1038/s41586-020-2649-2.

17. Hunter, J.D. Matplotlib: A 2D Graphics Environment. *Computing in Science Engineering* **2007**, *9*, 90–95, doi:10.1109/MCSE.2007.55.

18. Mckinney, W. Data Structures for Statistical Computing in Python. *Proceedings of the 9th Python in Science Conference* **2010**, *445*, 51–56.

19. Pedregosa, F.; Varoquaux, G.; Gramfort, A.; Michel, V.; Thirion, B.; Grisel, O.; Blondel, M.; Prettenhofer, P.; Weiss, R.; Dubourg, V.; et al. Scikit-Learn: Machine Learning in Python. *J. Mach. Learn. Res.* **2011**, *12*, 2825–2830.

20. Lopez, C.F.; Muhlich, J.L.; Bachman, J.A.; Sorger, P.K. Programming Biological Models in Python Using PySB. *Mol Syst Biol* **2013**, *9*, 646, doi:10.1038/msb.2013.1.

21. Cock, P.J.A.; Antao, T.; Chang, J.T.; Chapman, B.A.; Cox, C.J.; Dalke, A.; Friedberg, I.; Hamelryck, T.; Kauff, F.; Wilczynski, B.; et al. Biopython: Freely Available Python Tools for Computational Molecular Biology and Bioinformatics. *Bioinformatics* **2009**, *25*, 1422–1423, doi:10.1093/bioinformatics/btp163.

22. Trott, O.; Olson, A.J. AutoDock Vina: Improving the Speed and Accuracy of Docking with a New Scoring Function, Efficient Optimization, and Multithreading. *Journal of Computational Chemistry* **2010**, *31*, 455–461, doi:https://doi.org/10.1002/jcc.21334.

23. *Principles of Pharmacology: The Pathophysiologic Basis of Drug Therapy*; Golan, D.E., Tashjian, A.H., Eds.; 3rd ed.; Wolters Kluwer Health/Lippincott Williams & Wilkins: Philadelphia, 2012; ISBN 978-1-60831-270-2.

24. Hassan, M.; Mogollón, D.C.; Fuentes, O.; Sirimulla, S. DLSCORE: A Deep Learning Model for Predicting Protein-Ligand Binding Affinities. **2018**, 16.

25. Liu, Z.; Su, M.; Han, L.; Liu, J.; Yang, Q.; Li, Y.; Wang, R. Forging the Basis for Developing Protein–Ligand Interaction Scoring Functions. *Acc. Chem. Res.* **2017**, *50*, 302–309, doi:10.1021/acs.accounts.6b00491.

26. Durrant, J.D.; McCammon, J.A. BINANA: A Novel Algorithm for Ligand-Binding Characterization. *J Mol Graph Model* **2011**, *29*, 888–893, doi:10.1016/j.jmgm.2011.01.004.

27. Jones, G.; Willett, P.; Glen, R.C.; Leach, A.R.; Taylor, R. Development and Validation of a Genetic Algorithm for Flexible Docking11Edited by F. E. Cohen. *Journal of Molecular Biology* **1997**, *267*, 727–748, doi:10.1006/jmbi.1996.0897.

28. Jain, A.N. Surflex: Fully Automatic Flexible Molecular Docking Using a Molecular Similarity-Based Search Engine. *J. Med. Chem.* **2003**, *46*, 499–511, doi:10.1021/jm020406h.

29. Friesner, R.A.; Banks, J.L.; Murphy, R.B.; Halgren, T.A.; Klicic, J.J.; Mainz, D.T.; Repasky, M.P.; Knoll, E.H.; Shelley, M.; Perry, J.K.; et al. Glide: A New Approach for Rapid, Accurate Docking and Scoring. 1. Method and Assessment of Docking Accuracy. *J. Med. Chem.* **2004**, *47*, 1739–1749, doi:10.1021/jm0306430.

30. DeLean, A.; Munson, P.J.; Rodbard, D. Simultaneous Analysis of Families of Sigmoidal Curves: Application to Bioassay, Radioligand Assay, and Physiological Dose-Response Curves. *Am J Physiol* **1978**, *235*, E97-102, doi:10.1152/ajpendo.1978.235.2.E97.

31. Sebaugh, J.L. Guidelines for Accurate EC50/IC50 Estimation. *Pharm Stat* **2011**, *10*, 128–134, doi:10.1002/pst.426.

32. Neubig, R.R.; Spedding, M.; Kenakin, T.; Christopoulos, A. International Union of Pharmacology Committee on Receptor Nomenclature and Drug Classification. XXXVIII. Update on Terms and Symbols in Quantitative Pharmacology. *Pharmacol Rev* **2003**, *55*, 597–606, doi:10.1124/pr.55.4.4.

33. Patrick, G.L. *An Introduction to Medicinal Chemistry*; Fifth edition.; Oxford University Press: Oxford, 2013; ISBN 978-0-19-969739-7.

34. Sebaugh, J.L.; McCray, P.D. Defining the Linear Portion of a Sigmoid-Shaped Curve: Bend Points. *Pharmaceutical Statistics* **2003**, *2*, 167–174, doi:10.1002/pst.62.

35. Stein, M.; Gabdoulline, R.R.; Wade, R.C. Bridging from Molecular Simulation to Biochemical Networks. *Current Opinion in Structural Biology* **2007**, *17*, 166–172, doi:10.1016/j.sbi.2007.03.014.

36. Neves, S.R. G Protein Pathways. *Science* **2002**, *296*, 1636–1639, doi:10.1126/science.1071550.

37. Pfleger, J.; Gresham, K.; Koch, W.J. G Protein-Coupled Receptor Kinases as Therapeutic Targets in the Heart. *Nature Reviews Cardiology* **2019**, *16*, 612–622, doi:10.1038/s41569-019-0220-3.

38. Nair, A.G.; Gutierrez-Arenas, O.; Eriksson, O.; Vincent, P.; Hellgren Kotaleski, J. Sensing Positive versus Negative Reward Signals through Adenylyl Cyclase-Coupled GPCRs in Direct and Indirect Pathway Striatal Medium Spiny Neurons. *J Neurosci* **2015**, *35*, 14017–14030, doi:10.1523/JNEUROSCI.0730-15.2015.

39. Chang, C.; Poteet, E.; Schetz, J.A.; Gümüş, Z.H.; Weinstein, H. Towards a Quantitative Representation of the Cell Signaling Mechanisms of Hallucinogens: Measurement and Mathematical Modeling of 5-HT1A and 5-HT2A Receptor-Mediated ERK1/2 Activation. *Neuropharmacology* **2009**, *56*, 213–225, doi:10.1016/j.neuropharm.2008.07.049.

40. Kooistra, A.J.; Mordalski, S.; Pándy-Szekeres, G.; Esguerra, M.; Mamyrbekov, A.; Munk, C.; Keserű, G.M.; Gloriam, D.E. GPCRdb in 2021: Integrating GPCR Sequence, Structure and Function. *Nucleic Acids Research* **2021**, *49*, D335–D343, doi:10.1093/nar/gkaa1080.

41. Jassal, B.; Matthews, L.; Viteri, G.; Gong, C.; Lorente, P.; Fabregat, A.; Sidiropoulos, K.; Cook, J.; Gillespie, M.; Haw, R.; et al. The Reactome Pathway Knowledgebase. *Nucleic Acids Res* **2020**, *48*, D498–D503, doi:10.1093/nar/gkz1031.

42. Gessi, S.; Merighi, S.; Varani, K. Adenosine Receptors: The Status of the Art. In *The Adenosine Receptors*; Borea, P.A., Varani, K., Gessi, S., Merighi, S., Vincenzi, F., Eds.; Springer International Publishing: Cham, 2018; pp. 1–11 ISBN 978-3-319-90807-6.

43. Yan, L.; Burbiel, J.C.; Maaß, A.; Müller, C.E. Adenosine Receptor Agonists: From Basic Medicinal Chemistry to Clinical Development. *Expert Opinion on Emerging Drugs* **2003**, *8*, 537–576, doi:10.1517/14728214.8.2.537.

44. Kim, S.; Chen, J.; Cheng, T.; Gindulyte, A.; He, J.; He, S.; Li, Q.; Shoemaker, B.A.; Thiessen, P.A.; Yu, B.; et al. PubChem in 2021: New Data Content and Improved Web Interfaces. *Nucleic Acids Research* **2021**, *49*, D1388–D1395, doi:10.1093/nar/gkaa971.

45. Berman, H.M.; Westbrook, J.; Feng, Z.; Gilliland, G.; Bhat, T.N.; Weissig, H.; Shindyalov, I.N.; Bourne, P.E. The Protein Data Bank. *Nucleic Acids Research* **2000**, *28*, 235–242, doi:10.1093/nar/28.1.235.

46. Lebon, G.; Warne, T.; Edwards, P.C.; Bennett, K.; Langmead, C.J.; Leslie, A.G.W.; Tate, C.G. Agonist-Bound Adenosine A2A Receptor Structures Reveal Common Features of GPCR Activation. *Nature* **2011**, *474*, 521–525, doi:10.1038/nature10136.

47. Eswar, N.; Webb, B.; Marti-Renom, M.A.; Madhusudhan, M.S.; Eramian, D.; Shen, M.-Y.; Pieper, U.; Sali, A. Comparative Protein Structure Modeling Using Modeller. *Curr Protoc Bioinformatics* **2006**, *Chapter 5*, Unit-5.6, doi:10.1002/0471250953.bi0506s15.

48. de Lera Ruiz, M.; Lim, Y.-H.; Zheng, J. Adenosine A2A Receptor as a Drug Discovery Target. *J Med Chem* **2014**, *57*, 3623–3650, doi:10.1021/jm4011669.

49. Segala, E.; Guo, D.; Cheng, R.K.Y.; Bortolato, A.; Deflorian, F.; Doré, A.S.; Errey, J.C.; Heitman, L.H.; IJzerman, A.P.; Marshall, F.H.; et al. Controlling the Dissociation of Ligands from the Adenosine A2A Receptor through Modulation of Salt Bridge Strength. *J Med Chem* **2016**, *59*, 6470–6479, doi:10.1021/acs.jmedchem.6b00653.

50. Gupta, M.; Sharma, R.; Kumar, A. Docking Techniques in Pharmacology: How Much Promising? *Computational Biology and Chemistry* **2018**, *76*, 210–217, doi:10.1016/j.compbiolchem.2018.06.005.

51. Schneider, J.; Korshunova, K.; Musiani, F.; Alfonso-Prieto, M.; Giorgetti, A.; Carloni, P. Predicting Ligand Binding Poses for Low-Resolution Membrane Protein Models: Perspectives from Multiscale Simulations. *Biochemical and Biophysical Research Communications* **2018**, *498*, 366–374, doi:10.1016/j.bbrc.2018.01.160.

52. Buchwald, P. A Receptor Model With Binding Affinity, Activation Efficacy, and Signal Amplification Parameters for Complex Fractional Response Versus Occupancy Data. *Front. Pharmacol.* **2019**, *10*, 605, doi:10.3389/fphar.2019.00605.

53. Yun, Y.; Chen, J.; Liu, R.; Chen, W.; Liu, C.; Wang, R.; Hou, Z.; Yu, Z.; Sun, Y.; IJzerman, A.P.; et al. Long Residence Time Adenosine A1 Receptor Agonists Produce Sustained Wash-Resistant Antilipolytic Effect in Rat Adipocytes. *Biochemical Pharmacology* **2019**, *164*, 45–52, doi:10.1016/j.bcp.2019.03.032.

54. Guo, D.; Mulder-Krieger, T.; IJzerman, A.P.; Heitman, L.H. Functional Efficacy of Adenosine A_2A Receptor Agonists Is Positively Correlated to Their Receptor Residence Time. *Br J Pharmacol* **2012**, *166*, 1846–1859, doi:10.1111/j.1476-5381.2012.01897.x.

55. Schuetz, D.A.; de Witte, W.E.A.; Wong, Y.C.; Knasmueller, B.; Richter, L.; Kokh, D.B.; Sadiq, S.K.; Bosma, R.; Nederpelt, I.; Heitman, L.H.; et al. Kinetics for Drug Discovery: An Industry-Driven Effort to Target Drug Residence Time. *Drug Discovery Today* **2017**, *22*, 896–911, doi:10.1016/j.drudis.2017.02.002.

56. Bruce, N.J.; Ganotra, G.K.; Richter, S.; Wade, R.C. KBbox: A Toolbox of Computational Methods for Studying the Kinetics of Molecular Binding. *J. Chem. Inf. Model.* **2019**, *59*, 3630–3634, doi:10.1021/acs.jcim.9b00485.

57. Nunes-Alves, A.; Kokh, D.B.; Wade, R.C. Recent Progress in Molecular Simulation Methods for Drug Binding Kinetics. *Current Opinion in Structural Biology* **2020**, *64*, 126–133, doi:10.1016/j.sbi.2020.06.022.

58. Capelli, R.; Lyu, W.; Bolnykh, V.; Meloni, S.; Olsen, J.M.H.; Rothlisberger, U.; Parrinello, M.; Carloni, P. On the Accuracy of Molecular Simulation-Based Predictions of Koff Values: A Metadynamics Study. *bioRxiv* **2020**, 2020.03.30.015396, doi:10.1101/2020.03.30.015396.

CHAPTER 6

Building the structure-quantitative systems pharmacology biocomputing web-platform

6.1 Introduction

Due to the sheer amount of biological data and bioinformatics tools that have become available in the last decades, mainly thanks to the advent of the internet and the constant increase in computational power, the need for a systematic and standardized approach to use these tools and data has become fundamental [1,2]. For this reason, the use of web-services in life sciences have changed our approach in conducting biological research [3].

Web-services are, essentially, a platform to provide a standard way of publishing applications and data sources over the internet. But they are not limited to access biological information. Actually, one of the most prominent benefits of web-services is the accessible standardized environments, where non-IT experts, effectively, can carry out transparent, reproducible and reusable computational analysis and tasks from genome analysis to protein structure prediction [1–3].

Giving the importance of web-services in life sciences and the importance of bringing together the structure systems biology to the quantitative systems pharmacology (see *General Introduction*), the development of a web-service for structural quantitative pharmacology studies, became paramount. Therefore, we present in this chapter the conceptual design of a biocomputing platform tailored for in-depth studies of G-protein coupled receptors in order to improve current empirically driven drug discovery approaches in a more precise drug design towards these receptors. The central ideal of this platform is to easily predict classical pharmacodynamics' models of drug-target interactions given just as input basic structural information of the receptor and the drug. To accomplish this, we intend to combine individual services in a single common workflow, allowing them to communicate with each other by sharing data at execution time (*Fig. 6.1*). For this purpose we intend to combine *i)* the GOMoDo web-service [4], specific designed for homology modelling of human GPCRs; *ii)* the Hybrid MM/CG web-service [5] for predict binding poses in human GPCRs; *iii)* the structure-quantitative systems pharmacology framework, described in *Chapter 5*; and *iv)* a database for human GPCRs structures specific for structural systems biology.

The development of this integrative platform is still an ongoing process. The heterogenicity of the different tools makes their cross-communication arduous to implement. The platform has also been object of an intensive systematic validation before it is ready to be publicly released.

6.2 GPCR database for Structure Systems Biology

Obtaining atomic coordinates is crucial for any structural biology study. Thanks to the constant improvement in techniques for structure determination like high-throughput X-ray crystallography, multidimensional NMR spectroscopy, Cryo-Electron microscopy (cryo-EM), or small angle X-ray scattering (SAXS), the number of three-dimensional structures of proteins have been rapidly increasing (*Fig. 6.2*) [6].

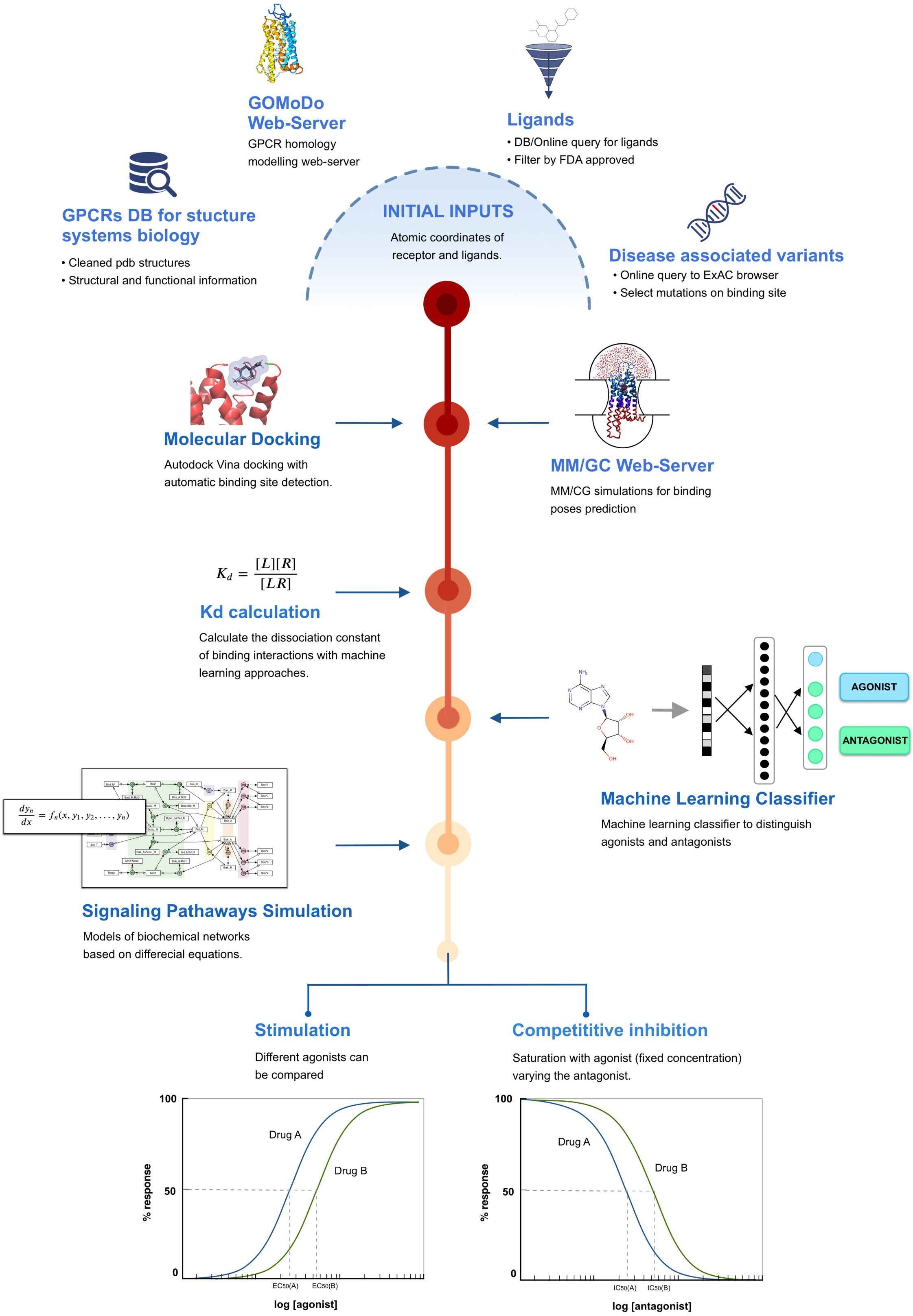

GOMoDo Web-Server
GPCR homology modelling web-server

Ligands
- DB/Online query for ligands
- Filter by FDA approved

GPCRs DB for stucture systems biology
- Cleaned pdb structures
- Structural and functional information

INITIAL INPUTS
Atomic coordinates of receptor and ligands.

Disease associated variants
- Online query to ExAC browser
- Select mutations on binding site

Molecular Docking
Autodock Vina docking with automatic binding site detection.

MM/GC Web-Server
MM/CG simulations for binding poses prediction

$$K_d = \frac{[L][R]}{[LR]}$$

Kd calculation
Calculate the dissociation constant of binding interactions with machine learning approaches.

Machine Learning Classifier
Machine learning classifier to distinguish agonists and antagonists

$$\frac{dy_n}{dx} = f_n(x, y_1, y_2, \ldots, y_n)$$

Signaling Pathways Simulation
Models of biochemical networks based on differecial equations.

Stimulation
Different agonists can be compared

Competititive inhibition
Saturation with agonist (fixed concentration) varying the antagonist.

Fig. 6.1 Conceptual pipeline of the structure-quantitative systems pharmacology biocomputing platform.

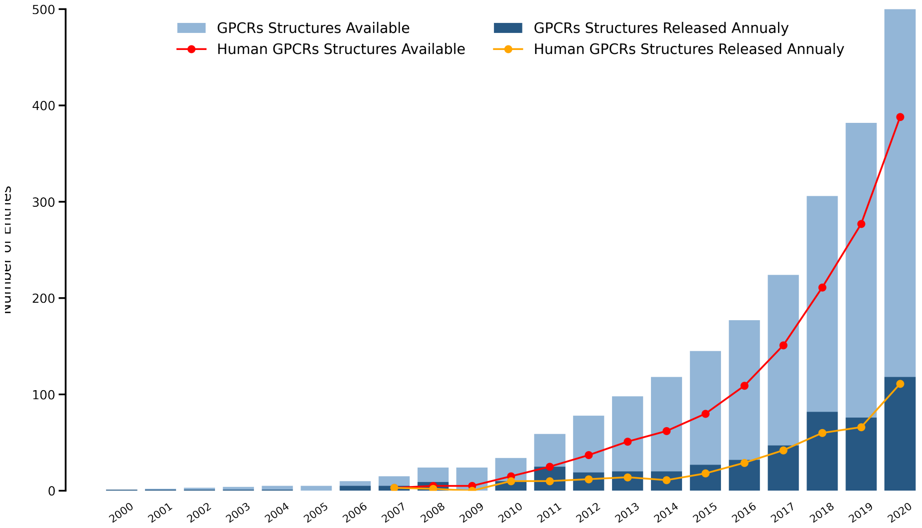

Fig. 6.2 Total number of GPCR structures deposited on the *Protein Data Bank* and the number of GPCR structures released per year. Data taken from the *GPCRdb [7]* (last access on December 2020).

However, even if such structures are deposited in free-accessible databases, like *The Protein Databank* [8], under a standardized format, once a protein is selected it can't be used directly. For instance, when a protein is being prepared for X-ray crystallography, it commonly undergoes a series of physio-biochemical processes, such as, the introduction of point mutations for thermostabilization improvement [9], co-expression with proteins from different species for better expression and solubility, or even the addition to the C-terminal of the protein a polyhistidine-tag for better protein purification [10]. Worse still, most of the time, the description of these changes in the original protein is hidden deeply into the metadata of the coordinate files, being often missed even by experienced researchers.

Taking all this into account, we came up with the idea of creating a database for human GPCR structures specific for structural systems biology. The main ideal is then, aggregate in one single database clean and ready-to-go human GPCR structures for modeling, docking, and molecular dynamics simulations.

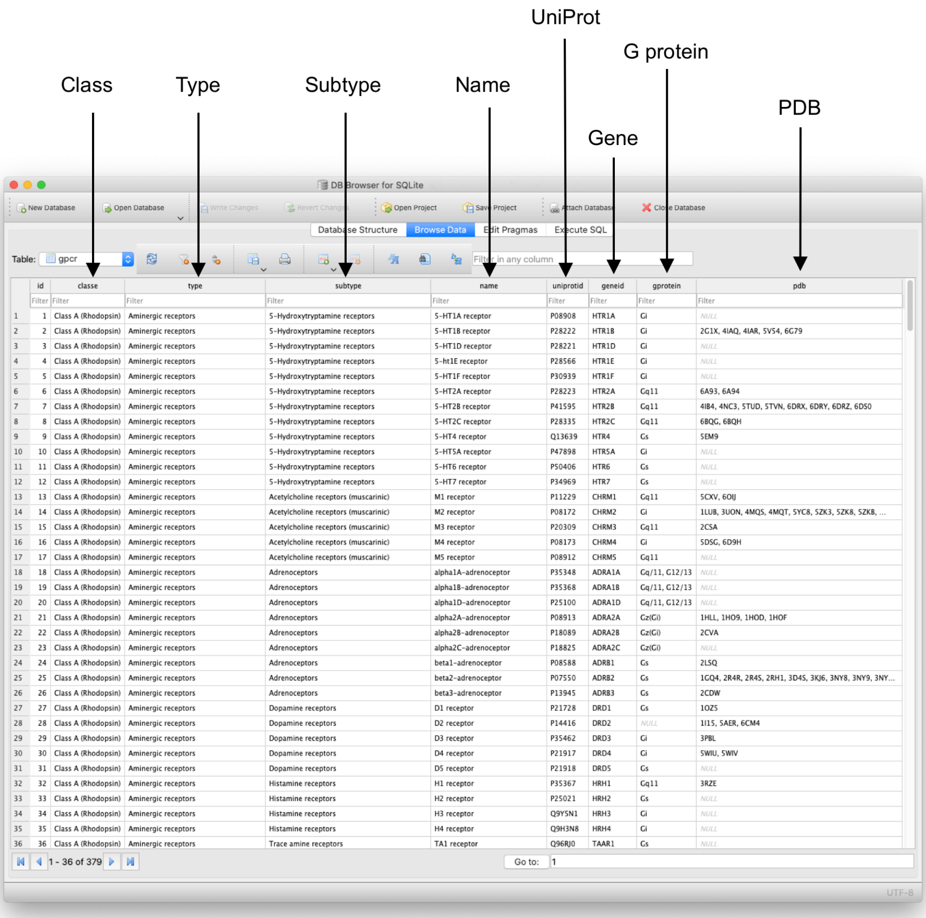

	id	classe	type	subtype	name	uniprotid	geneid	gprotein	pdb
	Filter	Filter	Filter	Filter	Filter	Filter	Filter	Filter	Filter
1	1	Class A (Rhodopsin)	Aminergic receptors	5-Hydroxytryptamine receptors	5-HT1A receptor	P08908	HTR1A	Gi	NULL
2	2	Class A (Rhodopsin)	Aminergic receptors	5-Hydroxytryptamine receptors	5-HT1B receptor	P28222	HTR1B	Gi	2G1X, 4IAQ, 4IAR, 5V54, 6G79
3	3	Class A (Rhodopsin)	Aminergic receptors	5-Hydroxytryptamine receptors	5-HT1D receptor	P28221	HTR1D	Gi	NULL
4	4	Class A (Rhodopsin)	Aminergic receptors	5-Hydroxytryptamine receptors	5-ht1E receptor	P28566	HTR1E	Gi	NULL
5	5	Class A (Rhodopsin)	Aminergic receptors	5-Hydroxytryptamine receptors	5-HT1F receptor	P30939	HTR1F	Gi	NULL
6	6	Class A (Rhodopsin)	Aminergic receptors	5-Hydroxytryptamine receptors	5-HT2A receptor	P28223	HTR2A	Gq11	6A93, 6A94
7	7	Class A (Rhodopsin)	Aminergic receptors	5-Hydroxytryptamine receptors	5-HT2B receptor	P41595	HTR2B	Gq11	4IB4, 4NC3, 5TUD, 5TVN, 6DRX, 6DRY, 6DRZ, 6DS0
8	8	Class A (Rhodopsin)	Aminergic receptors	5-Hydroxytryptamine receptors	5-HT2C receptor	P28335	HTR2C	Gq11	6BQG, 6BQH
9	9	Class A (Rhodopsin)	Aminergic receptors	5-Hydroxytryptamine receptors	5-HT4 receptor	Q13639	HTR4	Gs	5EM9
10	10	Class A (Rhodopsin)	Aminergic receptors	5-Hydroxytryptamine receptors	5-HT5A receptor	P47898	HTR5A	Gi	NULL
11	11	Class A (Rhodopsin)	Aminergic receptors	5-Hydroxytryptamine receptors	5-HT6 receptor	P50406	HTR6	Gs	NULL
12	12	Class A (Rhodopsin)	Aminergic receptors	5-Hydroxytryptamine receptors	5-HT7 receptor	P34969	HTR7	Gs	NULL
13	13	Class A (Rhodopsin)	Aminergic receptors	Acetylcholine receptors (muscarinic)	M1 receptor	P11229	CHRM1	Gq11	5CXV, 6OIJ
14	14	Class A (Rhodopsin)	Aminergic receptors	Acetylcholine receptors (muscarinic)	M2 receptor	P08172	CHRM2	Gi	1LUB, 3UON, 4MQS, 4MQT, 5YC8, 5ZK3, 5ZK8, 5ZKB, ...
15	15	Class A (Rhodopsin)	Aminergic receptors	Acetylcholine receptors (muscarinic)	M3 receptor	P20309	CHRM3	Gq11	2CSA
16	16	Class A (Rhodopsin)	Aminergic receptors	Acetylcholine receptors (muscarinic)	M4 receptor	P08173	CHRM4	Gi	5DSG, 6D9H
17	17	Class A (Rhodopsin)	Aminergic receptors	Acetylcholine receptors (muscarinic)	M5 receptor	P08912	CHRM5	Gq11	NULL
18	18	Class A (Rhodopsin)	Aminergic receptors	Adrenoceptors	alpha1A-adrenoceptor	P35348	ADRA1A	Gq/11, G12/13	NULL
19	19	Class A (Rhodopsin)	Aminergic receptors	Adrenoceptors	alpha1B-adrenoceptor	P35368	ADRA1B	Gq/11, G12/13	NULL
20	20	Class A (Rhodopsin)	Aminergic receptors	Adrenoceptors	alpha1D-adrenoceptor	P25100	ADRA1D	Gq/11, G12/13	NULL
21	21	Class A (Rhodopsin)	Aminergic receptors	Adrenoceptors	alpha2A-adrenoceptor	P08913	ADRA2A	Gz(Gi)	1HLL, 1HO9, 1HOD, 1HOF
22	22	Class A (Rhodopsin)	Aminergic receptors	Adrenoceptors	alpha2B-adrenoceptor	P18089	ADRA2B	Gz(Gi)	2CVA
23	23	Class A (Rhodopsin)	Aminergic receptors	Adrenoceptors	alpha2C-adrenoceptor	P18825	ADRA2C	Gz(Gi)	NULL
24	24	Class A (Rhodopsin)	Aminergic receptors	Adrenoceptors	beta1-adrenoceptor	P08588	ADRB1	Gs	2LSQ
25	25	Class A (Rhodopsin)	Aminergic receptors	Adrenoceptors	beta2-adrenoceptor	P07550	ADRB2	Gs	1GQ4, 2R4R, 2R4S, 2RH1, 3D4S, 3KJ6, 3NY8, 3NY9, 3NY...
26	26	Class A (Rhodopsin)	Aminergic receptors	Adrenoceptors	beta3-adrenoceptor	P13945	ADRB3	Gs	2CDW
27	27	Class A (Rhodopsin)	Aminergic receptors	Dopamine receptors	D1 receptor	P21728	DRD1	Gs	1OZ5
28	28	Class A (Rhodopsin)	Aminergic receptors	Dopamine receptors	D2 receptor	P14416	DRD2	NULL	1I15, 5AER, 6CM4
29	29	Class A (Rhodopsin)	Aminergic receptors	Dopamine receptors	D3 receptor	P35462	DRD3	Gi	3PBL
30	30	Class A (Rhodopsin)	Aminergic receptors	Dopamine receptors	D4 receptor	P21917	DRD4	Gi	5WIU, 5WIV
31	31	Class A (Rhodopsin)	Aminergic receptors	Dopamine receptors	D5 receptor	P21918	DRD5	Gs	NULL
32	32	Class A (Rhodopsin)	Aminergic receptors	Histamine receptors	H1 receptor	P35367	HRH1	Gq11	3RZE
33	33	Class A (Rhodopsin)	Aminergic receptors	Histamine receptors	H2 receptor	P25021	HRH2	Gs	NULL
34	34	Class A (Rhodopsin)	Aminergic receptors	Histamine receptors	H3 receptor	Q9Y5N1	HRH3	Gi	NULL
35	35	Class A (Rhodopsin)	Aminergic receptors	Histamine receptors	H4 receptor	Q9H3N8	HRH4	Gi	NULL
36	36	Class A (Rhodopsin)	Aminergic receptors	Trace amine receptors	TA1 receptor	Q96RJ0	TAAR1	Gs	NULL

Fig. 6.3 Screenshot of the SQL database of human GPCRs for structure systems biology.

To build this database, we start by getting from the GPCRdb [7] all the already identified human GPCRs, extracting, then, for each one, its *class*, *type*, *subtype*, *name*, *gene* and *UniProtKB* [11] *identifiers*. After, through the *UniProtKB identifier* we have queried the *REACTOME* database [12] to get the G protein to which the receptor is coupled with, and the *UniProtKB* database [11] itself to obtain all the PDB identifiers from the *Protein Data Bank* [8] belonging to the receptor of interest. Once all the PDB files of human GPCRs have been identified and downloaded, each one underwent a series of steps to become ready for structure biology studies. In a first step, the exogenous residues, those that don't belong to the GPCR of interest, as well as the expressions tags, like the polyhistidine-tags, were removed. Then, the thermostabilizing mutations were identified and re-mutated to the original residue using the MODELLER program [13]. Lastly, the amino acid sequence of each chain was compared with the related sequence from *UniProtKB* [11] in order to obtain a percentual value of the coverage.

Finally, all the information obtained was compiled into a SQL database (*Fig. 6.3*), so that it can be better integrated with APIs (application programing interfaces). Lastly, considering the constant increase in the number of solved protein's structures, the database was built into a framework that keeps the database automatically updated.

6.3 GOMoDo v2.0

The GOMoDo web-service is a GPCRs online modeling and docking web-service, developed in the Applied Bioinformatics Laboratory of the University of Verona, and publicly available since 2013. With a very easy user interface, this biocomputing platform allows users to effortlessly model GPCR structures and dock ligands to the model, obtaining biologically and pharmacologically relevant data, in a consistent pipeline: protein sequence alignment, homology modeling and model quality assessment, and docking [4].

One of the novelties that GOMoDo brought to the bioinformatic community was the use of local GPCR sequences and pre-generated alignments databases. However, at the time of its development and deployment, only less than 3% of the human GPCR structures were available, and those databases have never been updated since then. In addition, the code behind the back- and front-end of the web-service not only is difficult to maintain, but also no longer satisfies the necessary requisites for the utmost web performance and security, and also the interconnection with other web-services. These reasons prompted us to create the version 2.0 of GOMoDo, with a simplified back-end workflow, updated internal databases, and a refreshed graphical interface. To accomplish that, we start by re-coding all GOMoDo's workflow in the *python* programming language, which will facilitate the integration with other web-services developed under the same programming language. All the bioinformatic tools inside the server were also updated to their latest version, like HH-suite3 [14], for the multiple sequence alignment, and MODELLER [13] for homology modeling. In the same way, the databases used by these tolls, such as UNIREF30 and PDB70 databases [15] were also updated.

Finally, the next stage, which was not yet accomplished, is the development of the new graphical interface for the renewed GOMoDO's workflow. To ensure an effective interconnection with the other services that will make part of the main biocomputing platform, this task must, ideally, be undertaken concomitantly with the development of the other parts of the platform.

6.4 The Hybrid MM/CG Webserver

The work described in this section is taken from: Schneider, J.; ***Ribeiro, R.;*** *Alfonso-Prieto, M.; Carloni, P.; Giorgetti, A. Hybrid MM/CG Webserver: Automatic Set up of Molecular Mechanics/Coarse-Grained Simulations for Human G Protein-Coupled Receptor/Ligand Complexes. Front. Mol. Biosci. 2020, 7, doi:10.3389/fmolb.2020.576689.*

The MM/GC Webserver is an online server that automatizes and speeds up the MM/CG simulation set up of huma GPCR/ligands complexes. Hybrid Molecular Mechanics/Coarse-Grained (MM/CG) simulations help to predict ligand poses in human GPCRs, even if the receptor's structure is a lower resolution model [16,17].

In MM/CG simulations the receptor/ligand interactions are described in atomistic detail, including explicit water molecules in the binding site (MM region), while the rest of the receptor is coarse-grained (CG region) [16]. The all-atom force fields used [17] for the MM part of the protein and water are the Amber14SB [18] and TIP3P [19], respectively, whereas the ligand can be described using either GAFF or GAFF2 [20,21]. The CG region is described by a Gō-like [22] potential. A region at the interface between the MM and CG parts couples the two levels of resolution. The membrane is described implicitly by introducing five potential walls [16,23]. Two planar walls coincide with the height of the head groups of the membrane lipids, two hemispheric walls cap the extracellular and intracellular ends of the protein and prevent water evaporation, and the last wall follows the initial shape of the interface between protein and membrane, mimicking the effect of the lipid acyl tails (*for more details please see the original article*).

This approach turned out to be able to reproduce the ligand poses for four different human GPCRs [17]. These include the adenosine 2A receptor in complex with caffeine, the human bitter receptor 16 in complex with phenyl-β-D-glucopyranoside, the β2-adrenergic receptor with adrenaline, and the dopamine D3 receptor with eticlopride [17]. Retrospective validation against available X-ray structures and mutagenesis data confirmed that the MM/CG approach can predict correct ligand poses and identify experimentally determined binding residues [17], regardless of the model resolution. In addition, the MM/CG simulations can provide insights into the flexibility of receptor–ligand interactions and hydration of the binding cavity, at a lower computational cost than all-atom molecular dynamics simulations.

6.5 Future perspectives

With the conceptual design we are presenting here, we intend to build a computing platform designed for in-depth studies of post-synaptic receptors, in particular human GPCRs, in order to improve the current empirically driven drug discovery pipeline.

One of the advantages of building a biocomputing platform where many individual web-services can communicate with each other, is the possibility, at any time, to expand, improve and reintegrate the platform. We aim in the near future, integrate other services, for example, a web-service for kinetic constants prediction not only from drug-receptor binding, but also from binding and catalysis of the species downstream the signaling pathways.

References

1. Romano, P.; Marra, D.; Milanesi, L. Web Services and Workflow Management for Biological Resources. *BMC Bioinformatics* **2005**, *6*, S24, doi:10.1186/1471-2105-6-S4-S24.

2. Curcin, V.; Ghanem, M.; Guo, Y. Web Services in the Life Sciences. *Drug Discovery Today* **2005**, *10*, 865–871, doi:10.1016/S1359-6446(05)03481-1.

3. Raghava, G.P.S. PDWSB: Public Domain Web Servers in Biology. *Biotech Software & Internet Report* **2001**, *2*, 152–153, doi:10.1089/152791601753204304.

4. Sandal, M.; Duy, T.P.; Cona, M.; Zung, H.; Carloni, P.; Musiani, F.; Giorgetti, A. GOMoDo: A GPCRs Online Modeling and Docking Webserver. *PLoS One* **2013**, *8*, doi:10.1371/journal.pone.0074092.

5. Schneider, J.; Ribeiro, R.; Alfonso-Prieto, M.; Carloni, P.; Giorgetti, A. Hybrid MM/CG Webserver: Automatic Set up of Molecular Mechanics/Coarse-Grained Simulations for Human G Protein-Coupled Receptor/Ligand Complexes. *Front. Mol. Biosci.* **2020**, *7*, doi:10.3389/fmolb.2020.576689.

6. Pandey, A.; Shin, K.; Patterson, R.E.; Liu, X.-Q.; Rainey, J.K. Current Strategies for Protein Production and Purification Enabling Membrane Protein Structural Biology. *Biochem Cell Biol* **2016**, *94*, 507–527, doi:10.1139/bcb-2015-0143.

7. Kooistra, A.J.; Mordalski, S.; Pándy-Szekeres, G.; Esguerra, M.; Mamyrbekov, A.; Munk, C.; Keserű, G.M.; Gloriam, D.E. GPCRdb in 2021: Integrating GPCR Sequence, Structure and Function. *Nucleic Acids Research* **2021**, *49*, D335–D343, doi:10.1093/nar/gkaa1080.

8. Berman, H.M.; Westbrook, J.; Feng, Z.; Gilliland, G.; Bhat, T.N.; Weissig, H.; Shindyalov, I.N.; Bourne, P.E. The Protein Data Bank. *Nucleic Acids Research* **2000**, *28*, 235–242, doi:10.1093/nar/28.1.235.

9. Tate, C.G. A Crystal Clear Solution for Determining G-Protein-Coupled Receptor Structures. *Trends Biochem Sci* **2012**, *37*, 343–352, doi:10.1016/j.tibs.2012.06.003.

10. Hengen, P.N. Purification of His-Tag Fusion Proteins from Escherichia Coli. *Trends in Biochemical Sciences* **1995**, *20*, 285–286, doi:10.1016/S0968-0004(00)89045-3.

11. The UniProt Consortium UniProt: A Worldwide Hub of Protein Knowledge. *Nucleic Acids Research* **2019**, *47*, D506–D515, doi:10.1093/nar/gky1049.

12. Jassal, B.; Matthews, L.; Viteri, G.; Gong, C.; Lorente, P.; Fabregat, A.; Sidiropoulos, K.; Cook, J.; Gillespie, M.; Haw, R.; et al. The Reactome Pathway Knowledgebase. *Nucleic Acids Res* **2020**, *48*, D498–D503, doi:10.1093/nar/gkz1031.

13. Webb, B.; Sali, A. Comparative Protein Structure Modeling Using MODELLER. *Current Protocols in Bioinformatics* **2016**, *54*, 5.6.1-5.6.37, doi:10.1002/cpbi.3.

14. Steinegger, M.; Meier, M.; Mirdita, M.; Vöhringer, H.; Haunsberger, S.J.; Söding, J. HH-Suite3 for Fast Remote Homology Detection and Deep Protein Annotation. *BMC Bioinformatics* **2019**, *20*, 473, doi:10.1186/s12859-019-3019-7.

15. Mirdita, M.; von den Driesch, L.; Galiez, C.; Martin, M.J.; Söding, J.; Steinegger, M. Uniclust Databases of Clustered and Deeply Annotated Protein Sequences and Alignments. *Nucleic Acids Research* **2017**, *45*, D170–D176, doi:10.1093/nar/gkw1081.

16. Schneider, J.; Korshunova, K.; Musiani, F.; Alfonso-Prieto, M.; Giorgetti, A.; Carloni, P. Predicting Ligand Binding Poses for Low-Resolution Membrane Protein Models: Perspectives from Multiscale Simulations. *Biochemical and Biophysical Research Communications* **2018**, *498*, 366–374, doi:10.1016/j.bbrc.2018.01.160.

17. Schneider, J.; Korshunova, K.; Si Chaib, Z.; Giorgetti, A.; Alfonso-Prieto, M.; Carloni, P. Ligand Pose Predictions for Human G Protein-Coupled Receptors: Insights from the Amber-Based Hybrid Molecular Mechanics/Coarse-Grained Approach. *J. Chem. Inf. Model.* **2020**, *60*, 5103–5116, doi:10.1021/acs.jcim.0c00661.

18. Maier, J.A.; Martinez, C.; Kasavajhala, K.; Wickstrom, L.; Hauser, K.E.; Simmerling, C. Ff14SB: Improving the Accuracy of Protein Side Chain and Backbone Parameters from Ff99SB. *J. Chem. Theory Comput.* **2015**, *11*, 3696–3713, doi:10.1021/acs.jctc.5b00255.

19. Jorgensen, W.L.; Chandrasekhar, J.; Madura, J.D.; Impey, R.W.; Klein, M.L. Comparison of Simple Potential Functions for Simulating Liquid Water. *J. Chem. Phys.* **1983**, *79*, 926–935, doi:10.1063/1.445869.

20. Wang, J.; Wolf, R.M.; Caldwell, J.W.; Kollman, P.A.; Case, D.A. Development and Testing of a General Amber Force Field. *J. Comput. Chem.* **2004**, *25*, 1157–1174, doi:10.1002/jcc.20035.

21. Case, D.A.; Belfon, K.; Ben-Shalom, I.; Brozell, S.R.; Cerutti, D.; Cheatham, T.; Cruzeiro, V.W.D.; Darden, T.; Duke, R.E.; Giambasu, G.; et al. Amber 2020. **2020**.

22. Gō N.; Abe, H. Noninteracting Local-Structure Model of Folding and Unfolding Transition in Globular Proteins. I. Formulation. *Biopolymers* **1981**, *20*, 991–1011, doi:10.1002/bip.1981.360200511.

23. Leguèbe, M.; Nguyen, C.; Capece, L.; Hoang, Z.; Giorgetti, A.; Carloni, P. Hybrid Molecular Mechanics/Coarse-Grained Simulations for Structural Prediction of G-Protein Coupled Receptor/Ligand Complexes. *PLoS ONE* **2012**, *7*, e47332, doi:10.1371/journal.pone.0047332.

CHAPTER 7

Conclusions

In this thesis we attempted to, applying a structure-quantitative systems pharmacology approach, correlate the intracellular effects of the activation of neurosignaling cascades on ligand binding to neuroreceptors, and build a computational platform that integrates such approaches.

Firstly, we began by bridging structural macromolecular data with network biology to provide a rationale on the structure-function relationships of a disease variant of the oxytocin receptor and the NMDA receptor. With regard to the former study, we implemented a systems biology model of the signaling pathway of the oxytocin receptor in order to give a better understand behind the difference on dynamics of the intracellular Ca^{2+} between the OTXR-WT and OXTR-A218T that had been observed experimentally. Here, we have shown that the change in receptor activation caused by the mutation might be the key factor for the observed changes in intracellular Ca^{2+} concentrations, which may be implied in the maintaining downstream signal specificity. Similarly, we also implemented a systems biology model of the NMDA and AMPA mediated synapse CA1-CA3 transmission, which allow us to analyze the impact of single disease associated variants of NMDA receptors, related to neurological disorders and cognitive impairments. In this study, we were able to consistently reproduce experimental data and to quantitatively infer molecular-level causality of a variant-related functional impairment. All in all, with these studies we showed that the predictive power of such multiscale approaches can help us to understand complex biological and pathophysiological phenomena.

In second place, we developed a structural-quantitative systems pharmacology framework for the prediction of classical pharmacodynamic models towards G-protein coupled receptors. Here, we demonstrated that even with some limitations, the framework is able to predict efficacy and potency parameters of drugs comparable qualitatively to experimental values.

At last, we proposed the conceptual structure-quantitative systems pharmacology web-interface biocomputing platform. With this platform we want to make it possible to access the drug-receptor binding effects at different levels: from the molecular level to the entire network of interactions through a systems biology approach. Specifically, we are creating a platform where one can easily predict classical pharmacodynamics models of drug-target interactions given just as input basic structural information of the receptor and the drug. Consequently, the platform will return ligand receptor binding and dose-response curves allowing the comparison between the effects of different drugs upon receptor binding or between a ligand and receptors with associated disease variances.

Addendum

The work presented in this thesis doesn't cover all the research activities that I endeavor during my Ph.D. Program in Biotechnology.

In fact, during the three years of my doctoral studies I participated in several other projects in collaboration with different research groups. In particular, I would like to highlight the project entitled "Understanding the molecular properties responsible for the pharmacology of Cys-loop receptors" that I undertook for three months in the "Institut de Biologie Physico-Chimique", which belongs to the "Centre National de la Recherche Scientifique" (CNRS) based in Paris, France, under the supervision of Prof. Dr. Marc Baaden. I am deeply grateful to Prof. Baaden for hosting me and for his insightful comments and suggestions.

From these collaborations some articles were published:

- Amundarain, M.J.; **Ribeiro, R.P.**; Costabel, M.D.; Giorgetti, A. GABAA Receptor Family: Overview on Structural Characterization. Future Medicinal Chemistry **2019**, 11, 229–245, doi:10.4155/fmc-2018-0336.

- De Rosa, C.; Melchior, A.; Sanadar, M.; Tolazzi, M.; Giorgetti, A.; **Ribeiro, R.P.**; Nardon, C.; Piccinelli, F. Effect of the Heteroaromatic Antenna on the Binding of Chiral Eu(III) Complexes to Bovine Serum Albumin. *Inorg. Chem.* **2020**, *59*, 12564–12577, doi:10.1021/acs.inorgchem.0c01663.

- Marchetto, A.; Si Chaib, Z.; Rossi, C.A.; **Ribeiro, R.**; Pantano, S.; Rossetti, G.; Giorgetti, A. CGMD Platform: Integrated Web Servers for the Preparation, Running, and Analysis of Coarse-Grained Molecular Dynamics Simulations. *Molecules* **2020**, *25*, 5934, doi:10.3390/molecules25245934.

Lastly, apart from all research activities and collaborations I was also involved in tutoring and teaching activities, which, in my judgment, were extremely valuable for my career as a researcher.

Abbreviations

A

ASD	Autism spectrum disorder
AMPA	α-amino-3-hydroxy-5-methyl-4-isoxazolepropionic acid

B

bAP	back-propagating action potential

C

CaM	Calmodulin
CaMK	Ca2+/CAM-dependent Kinase
CaMKII	Ca2+/CAM-dependent Kinase
cAMP	Cyclic adenosine monophosphate
CAS	CaMKII Activation Simulation
CPC	Current/Potential Calculation

D

DAG	Diacylglycerol

E

ER	Endoplasmic Reticulum

F

FDA	Food and Drug Administration

G

GPCR	G protein coupled receptor

H

HIT	small molecule that binds to the target and is able to modify its function

I

IP_3	Inositol-1,4,5-trisphosphate
IP_3R	Inositol-1,4,5-trisphosphate receptor

L

Lead	A chemical compound that has pharmacological or biological activity with a possible therapeutic use.
LTD	Long Term Depression
LTP	Long Term Potentiation

M

MAPK	Mitogen-activated protein kinase
mCaMKII	Individual subunits of Calmodulin Kinase II
MD	Molecular Dynamics
MM/CG	Molecular mechanics/Coarse-grained

N

NMDA	N-Methyl-D-aspartic acid
NMR	Nuclear magnetic resonance
nsSNP	Non-synonymous single nucleotide polymorphisms

O

ODE	Ordinary differential equations
OXT	Oxytocin
OXTR	Oxytocin receptor

P

PDE	Partial differential equations
PIP$_2$	Phosphatidylinositol 4,5-bisphosphate
PKA	Phosphokinase A
PKC	Phosphokinase C
PLC	Phospholipase C

R

RGS	Receptors Gating Simulation

S

SQL	Structured Query Language

W

WT	Wild type

 # Quem vier atrás, feche a porta!

(Portuguese saying)